Development of Novel Optical Design and Signal Processing Approaches in Optical Coherence Imaging

by

Ruobing Qian

Department of Biomedical Engineering
Duke University

Date:_____

Approved:

_____
Joseph A. Izatt, Advisor

_____
Joel A. Greenberg

_____
Roarke W. Horstmeyer

_____
Anthony N. Kuo

_____
Adam P. Wax

Dissertation submitted in partial fulfillment of
the requirements for the degree of Doctor
of Philosophy in the Department of
Biomedical Engineering in the Graduate School
of Duke University

2020

ABSTRACT

Development of Novel Optical Design and Signal Processing Approaches in Optical Coherence Imaging

by

Ruobing Qian

Department of Biomedical Engineering
Duke University

Date:_____

Approved:

_____
Joseph A. Izatt, Advisor

_____
Joel A. Greenberg

_____
Roarke W. Horstmeyer

_____
Anthony N. Kuo

_____
Adam P. Wax

An abstract of a dissertation submitted in partial fulfillment of the requirements for the degree of Doctor of Philosophy in the Department of Biomedical Engineering in the Graduate School of Duke University

2020

Abstract

Optical coherence tomography (OCT) is a non-invasive optical imaging modality which can provide high-resolution, cross-sectional images of retina and cornea. It has become a standard of care in ophthalmology for the diagnosis and monitoring of ocular diseases. However, current OCT systems face several major challenges, among which include: (1) difficult alignment and fixation in pediatric retinal imaging (2) limited cellular-level contrast for ophthalmic disease diagnosis and (3) expensive hardware and intensive computation requirements for real-time high-speed 3D imaging.

This dissertation describes the development of several novel optical design and signal processing approaches in OCT and optical coherence imaging technologies to address these limitations. We first describe a long working distance swept-source OCT system to facilitate retinal imaging in young children (chapter 2). The system incorporates two custom lenses and a novel compact 2f retinal scanning configuration to achieve a working distance of 350mm with a 16^{o} OCT field of view. The system achieves high quality retinal imaging of children as young as 21 months old without sedation in the clinic. We then present a spectroscopic OCT technology that utilizes time-frequency analysis to obtain quantitative diagnostic information of cellular responses in the anterior chamber of the eye, which can indicate many ocular diseases such as hyphema and anterior uveitis. We demonstrate that this technology can differentiate and quantify

the composition of anterior chamber blood cells such as red blood cells and subtypes of WBCs, including granulocytes, lymphocytes and monocytes (chapter 3 and 4). Finally, we describe a coherence-based 3D imaging technique that uses a grating for fast beam steering, a swept-source laser with long coherence length, and time-frequency analysis for depth retrieval (chapter 5). We demonstrate that the system can achieve high-speed 3D imaging with sub-millimeter axial resolution and tens of centimeters axial imaging ranging.

Contents

List of Tables

List of Figures

Acknowledgements

First and foremost, I would like to thank my advisor, Dr. Joseph Izatt, for his amazing support, guidance and mentorship. You inspired me to take on challenging engineering problems with hard work, dedication and creativity. Thank you for bringing me into this incredible field of medical optics. I could not have dreamed of a better advisor!

I would also like to thank all the Izatt lab members and alumni for their great support over the past six years. The incredibly collaborative work environment is something I will cherish forever. I would especially like to thank Kevin Zhou. We have worked together on almost all the projects we did in the Izatt lab. I enjoyed all the research discussions with you, and I have learned so much from you in the past years. I also want to thank Oscar Carrasco-Zevallos, who mentored me in the first two years of my Ph.D. The incredible amount of trust that you placed in me when I first started continue to motivate me today. I also would like to thank Francesco LaRocca, Derek Nankivil, Christian Viehland, Ryan McNabb and James Polans who taught me lots of optics knowledge when I started.

I would also like to thank Dr. Roarke Horstmeyer and all the members in his lab. I really enjoyed working with you in the DCS project. Our collaboration led to such wonderful discussions.

Dr. Anthony Kuo and Dr. Cynthia Toth, I feel so lucky to have the opportunity to collaborate with you on several clinical OCT projects. Without you, I won't be able to translate the engineering technologies I developed in the lab into impactful clinical practice. Dr. Joel Greenberg, Dr. Adam Wax and Dr. Sina Farsiu, your guidance and support throughout my years at Duke will never be forgotten.

I would like to thank my loving parents for their unconditional support and love throughout my life. You are the reason that I can freely pursue my dreams in technology. I wouldn't become a person I am today without your nurture and guidance.

Serene Hu, I was so fortunate to meet you at the first day of the graduate school. We have had so many wonderful memories together throughout our graduate studies. Every time I was frustrated with my research, you were always there to support and encourage me. You are the most important part of my life! I look forward to the next stages of our lives together!

Finally, I would like to take this opportunity to thank all the doctors, nurses and healthcare workers (including my mom), who devoted themselves to battling the COVID-19 pandemic. Despite the challenges, I have faith that the national health systems and advancements in COVID-19 R&D will soon pivot us onto a path for recovery.

1. Introduction

1.1 Overview of Research Aims

This dissertation focuses on the development of novel optical design and signal processing approaches in optical coherence imaging. As detailed in the following section, OCT is a non-invasive optical imaging modality which can provide high-resolution, cross-sectional images of retina and cornea. It has become a standard of care for ophthalmic imaging. However, current OCT systems face several challenges or limitations, among which include: (1) difficult alignment and fixation in pediatric retinal imaging (2) poor contrast for blood cell differentiation in the anterior chamber and (3) expensive hardware and intensive computation requirements for real-time high-speed 3D imaging. To address these limitations, this dissertation is divided into the following three research aims:

- Specific Aim 1: a SS-OCT system that incorporates two custom lenses and a novel 2f retinal scanning configuration to achieve a working distance of 350mm. The system can facilitate retinal imaging of young children. This aim is addressed in Chapter 2.
- Specific Aim 2: a spectroscopic OCT method to utilize time-frequency analysis to obtain quantitative diagnostic information of cellular responses in the ocular anterior chamber. The method can be used to differentiate and

quantify the composition of anterior chamber blood cells noninvasively. This aim is addressed in Chapter 3 and 4.

- Specific Aim 3: a high-speed coherence-based 3D imaging technology that uses a grating for fast beam steering and time-frequency analysis for depth retrieval. The system can achieve >video rate(30Hz) 3D imaging with sub-millimeter axial resolution and tens of centimeters axial imaging ranging. This aim is addressed in Chapter 5.

1.2 Optical Coherence Tomography

Optical coherence tomography (OCT) is an optical imaging modality that provides cross-sectional images of biological tissue and transparent objects with micron-scale resolution and millimeter-scale penetration depth [1]. Since its invention in 1991, OCT has become has become a standard of care for ophthalmology imaging [2, 3], and is used to diagnose and monitor a variety of ocular diseases, such as glaucoma and macular degeneration [4-6] . OCT has been widely used in other biomedical applications, such as dentistry [7], dermatology [8], endoscopic imaging of the esophagus [9] and catheter based intravascular imaging [10]. Recently, OCT has also been used in many non-biomedical applications, such as integrated-circuit inspection [11], conservation of artwork [12] and large-scale depth ranging [13].

The principle of OCT is based on the low-coherence interferometry. The first-generation OCT system is time-domain OCT (TD-OCT). In a typical TD-OCT (Fig.1), light from a broadband low-coherence source is split into two channels by a 2*2 fiber-optic coupler. Light exiting the sample arm fiber is incident upon the scanning optics, such as a galvanometer mirror, and an objective lens that focuses the light onto the sample. The backscattered light from the sample is collected by the same fiber and mixed with the reflecting light from the reference arm. The combined light interferes on the surface of a photodetector, and the raw interferometric signal is detected by scanning the reference arm delay. The raw interferometric signal is then processed into an A-scan, which represents the depth-resolved reflectivity profile of the sample at the focal spot of the beam. Scanning the sample arm beam position in one lateral dimension would result in two-dimensional cross-sectional images known as B-scans, and in two lateral dimensions would result in three-dimensional images known as volumes, or volumetric images.

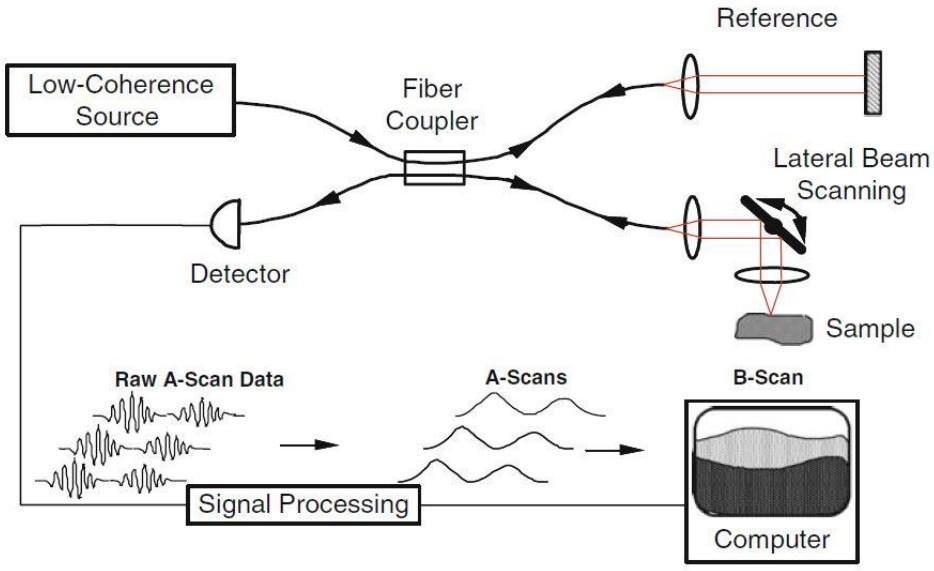

Figure 1: Reproduced from [14]. Schematic of a generic fiber-optic TD-OCT system. Bold lines represent fiber-optic paths, red lines represent free space optical paths, and thin lines represent electronic signal paths.

The lateral resolution of the OCT is similar to scanning confocal microscope, as the single mode fiber is essentially a pinhole aperture for both illumination and collection optics. Therefore, the theoretical lateral resolution of an OCT system can be calculated using the following equation:

$$\delta x = 0.37 \frac{\lambda_0}{NA} \tag{1}$$

where λ_0 is the center wavelength of the light source, and NA is the numerical aperture of the sample arm objective. The axial resolution of the OCT is determined by the wavelength and the bandwidth of the light source,

$$\delta z = \frac{2\ln(2)}{\pi} \frac{{\lambda_0}^2}{\Delta\lambda} \tag{2}$$

where $\Delta\lambda$ is the bandwidth of the source.

TD-OCT relies on translating the reference arm pathlength mechanically to get the depth profile at each lateral position (A-scan). Thus, the A-scan rate of a typical TD-OCT system is less than a few kilohertz, which means at least hundreds of milliseconds are needed to get a cross-sectional image (B-scan) of a sample, which severely limits its *in vivo* applications.

To address this limitation, two Fourier-domain OCT (FD-OCT) technologies, spectral-domain OCT (SD-OCT) and swept-source OCT (SS-OCT), were invented [15-18], and both technologies don't require reference arm translation. In SD-OCT, a broadband light source is still used, and the spectral power density of the spectral interferogram, $I_D(k)$, is recorded by a spectrometer. The sample reflectivity profile or A-scan can then be calculated from the Fourier transform of $I_D(k)$. In SS-OCT, instead of a broadband source, a rapid wavelength-sweeping laser is used. Since the frequency information of the spectral interferogram is separate in time, a high-speed photodetector can be used to resolve the spectral interferogram, and the same Fourier transform calculation can be used to calculate the A-scan. FD-OCT not only significantly improves the imaging speed, but also offers a 20-30 dB sensitivity advantage compared to TD-OCT [19-21].

1.3 OCT Imaging in Pediatric Ophthalmology

An estimated 19 million children worldwide are visually impaired, and 1.4 million are irreversibly blind[22]. To decrease the risk for blindness, it is critical to

diagnose these children early on and treat the evolving disease prior to permanent damage. Optical coherence tomography (OCT) has become a standard clinical diagnostic tool for management of ocular diseases in adults and older children [23, 24]. Clinical tabletop OCT systems have working distances of approximately 25 mm and require a chinrest to immobilize the patient. To acquire high-quality OCT images, these systems necessitate upright and cooperative patients who can fixate for seconds at a time with large instrumentation close to their face. Imaging of young children and toddlers, who are uncooperative and inherently afraid of objects close to their face, with conventional OCT is challenging and thus, diagnostic retinal screening of this population is currently limited.

The most popular approach to facilitate OCT pediatric imaging is handheld OCT. Multiple handheld OCT (HHOCT) probes have been developed and used to image infants and young children in the supine position, either under sedation with general anesthesia [25-29] or without sedation [30-32]. Retinal imaging with HHOCT has significantly contributed to the understanding of the development of infant retina *in vivo* [33-39] and aided in uncovering microanatomic structural retinal changes in infants and children with retinopathy of prematurity [30, 34, 36, 40-45], albinism [29], nystagmus [46, 47] and shaken baby syndrome [26, 48]. Recently, several handheld OCT angiography probes have also been developed to allow non-invasive imaging of retinal microvasculature in infants [49, 50].

1.4 Spectroscopic OCT

Utilizing a broadband source, OCT can retrieve both structural and spectral information of the sample. Spectroscopic OCT, an extension of OCT, uses time-frequency analysis to perform depth-resolved spectroscopy study [51, 52]. Spectroscopic OCT has two contrast contributions: absorption and scattering. For absorption, some strong absorbers in biological samples are blood/hemoglobin and melanin. For scattering, the backscattering spectral information in spectroscopic OCT is sensitive to scatterer structure, such as scatterer size, shape and geometrical distribution. Several studies have shown that using spectroscopic OCT, the size of microspheres can be retrieved with an accuracy better than the OCT resolution [52, 53]. Multiple spectroscopic OCT applications have previously been developed to study the absorption or scattering properties of tissue *ex vivo* or *in vivo*. For example, Robles et al., developed molecular imaging true-color spectroscopic optical coherence tomography to allow depth resolved quantification of hemoglobin oxygenation [54]. Yi et al., demonstrated *in vivo* retinal oximetry using visible-light spectroscopic OCT [55]. Zhao et al., demonstrated spectroscopic OCT can evaluate burn injuries *in vivo* [56].

One of the major limitations of spectroscopic OCT is the inherent tradeoff between spectral and axial (temporal) resolution in the time-frequency analysis, where improvement in one necessitates degradation in the other. A broader bandwidth source can certainly mitigate the effect of this tradeoff. On the other hand, different time-

frequency processing methods have also been developed to address this limitation. For instance, Xu et al., demonstrated that the Wigner–Ville distribution (WVD) can improve the time-bandwidth product of the spectroscopic analysis, compared to the conventional short-time Fourier transform [57]; Robles et al., developed a dual window method that applies two orthogonal Gaussian windows to independently determine the spectral and temporal resolution, such that both high spectral and temporal resolution can be maintained [58]; Most recently, Zhou et al., developed a technique named spectroscopic optical coherence refraction tomography, which uses spectroscopic OCT images from multiple angles to reconstruct a spectroscopic image with isotropic spatial resolution limited by the OCT lateral resolution [59].

1.5 Long-range 3D Imaging using OCT

During the last two decades, OCT speed (A-scan rate) has increased by over three orders of magnitude from TD-OCT to SS-OCT [60]. Recently, new developments in high-speed swept-source lasers and high-end digitizer further improve the OCT A-scan rate to megahertz range [61], allowing live video rate (>30Hz) volumetric OCT imaging of biological tissue [62]. To process and display these huge amounts of data in real-time, GPU or field-programmable gate array (FPGA) accelerated computing are required.

On the other hand, conventional FD-OCT systems usually have an imaging range or coherence length of several millimeters, limited by the number of spectrometer pixels in SD-OCT and instantaneous linewidth of swept-source in SS-OCT. Therefore, OCT applications are typically restricted to millimeter-scale tissue imaging. Recently, there is a growing interest in developing long imaging range OCT system for many high-speed 3D imaging applications, such as LiDAR, virtual reality, machine vision, precision measurement, and nondestructive evaluation of materials. SS-OCT for high-resolution distance measurements over long ranges (>tens of centimeters) is also named optical frequency-modulated continuous-wave (FMCW) reflectometry, which has drawn great interests from LiDAR developers in the industry such as self-driving car. These long-range SS-OCT or FMCW systems typically utilize vertical-cavity surface-emitting lasers (VCSEL) or distributed feedback laser (DFB), which have coherence lengths longer than meters. For example, Wang et al., demonstrated a 100kHz SS-OCT system with an

axial imaging range of >1.5m using a long coherence length, 1310 nm VCSEL [13] ; Song et al., developed a 100kHz SS-OCT system with an imaging range of ~10cm using an akinetic programmable swept laser [63]; DiLazaro et al., developed a FMCW system that has an imaging range of >6m and an axial resolution of 27.1μm using 12 combined distributed feedback laser (DFB) elements [64].

2. Long Working Distance OCT (LWD-OCT) to Facilitate Retinal Imaging in Children

2.1 Abstract

We demonstrate a prototype retinal swept-source OCT system with a long working distance (from the last optical element to the subject's eye) to facilitate pediatric imaging. To reduce the number of optical elements and axial length compared to the traditional 4f telescope, we employ a compact 2f retinal scanning configuration and achieve a working distance of 350 mm with a 16° OCT field of view. We performed imaging of fovea and optic nerve head using the prototype system in participants with and without pathology from three age groups: adults, children 13 to 18 years old and children under 6 years old. Several important imaging parameters such as image quality and alignment time were evaluated. The system successfully imaged 88 of 94 eligible eyes, including 7 of 10 eyes of young children, and 86% OCT images from young children, were graded as high-quality scans. This LWD-OCT system can potentially facilitate OCT imaging in young children.

2.2 Background

An estimated 19 million children worldwide are visually impaired, and 1.4 million are irreversibly blind [22]. To decrease the risk for blindness, it is critical to diagnose these children early on and treat the evolving disease prior to permanent damage. OCT is a diagnostic imaging modality that provides high resolution cross-sectional images of the human retina in vivo [65] and has become a standard clinical

diagnostic tool for management of vitreoretinal diseases in adults and older children [23, 24]. Clinical tabletop OCT systems have working distances of approximately 25 mm and require a chinrest to immobilize the patient. To acquire high-quality OCT images, these systems necessitate upright and cooperative patients who can fixate for seconds at a time with large instrumentation close to their face. Imaging of young children and toddlers, who are uncooperative and inherently afraid of objects close to their face, with conventional OCT is challenging and thus, diagnostic retinal screening of this population is currently limited. The A-line rates of spectral-domain OCT clinical-grade systems are also limited to 20-68 kHz [66] and require several seconds for volumetric acquisition, which may be insufficient to image young children who cannot adequately fixate for seconds at a time.

An alternative approach is to use handheld OCT (HHOCT) probes to image infants and young children in the supine position, either under sedation with general anesthesia[25-29] or without sedation[30-32]. However, similar to clinical OCT scanners, the HHOCT probe must also be placed approximately 25 mm away from the eye to achieve alignment and requires the child to be stable (and usually supine). While experts may be able to image young children and infants sitting on a parent's lap or in the supine position while cradled in the parent's arms [67], imaging of uncooperative young children and infants without sedation is generally difficult with current HHOCT systems.

The goal of this study is to design and demonstrate a prototype retinal swept-source OCT system with a long working distance (from the last optical element to the subject's eye) of at least 350 mm to facilitate pediatric imaging.

2.3 Methods

2.3.1 Lens and System Design

We used a single 2f refractive relay to design a long working distance OCT system with a compact form factor (Fig.2). In this design, a beamshaping lens (L_1) directed converging light through the optical scanners to a focus at a distance f_2 prior to the objective (L_2), resulting in collimated light incident on the cornea. The scanning mirrors were placed conjugate to the subject's pupil at a distance $2f_2$ prior to the objective lens (L_2). To achieve our design goal of 10 μm diffraction-limited lateral resolution at the retinal plane across +/− 8° FOV, L_1 and L_2 are two custom-designed lenses. The detailed lens design of these two lenses is shown in the results section.

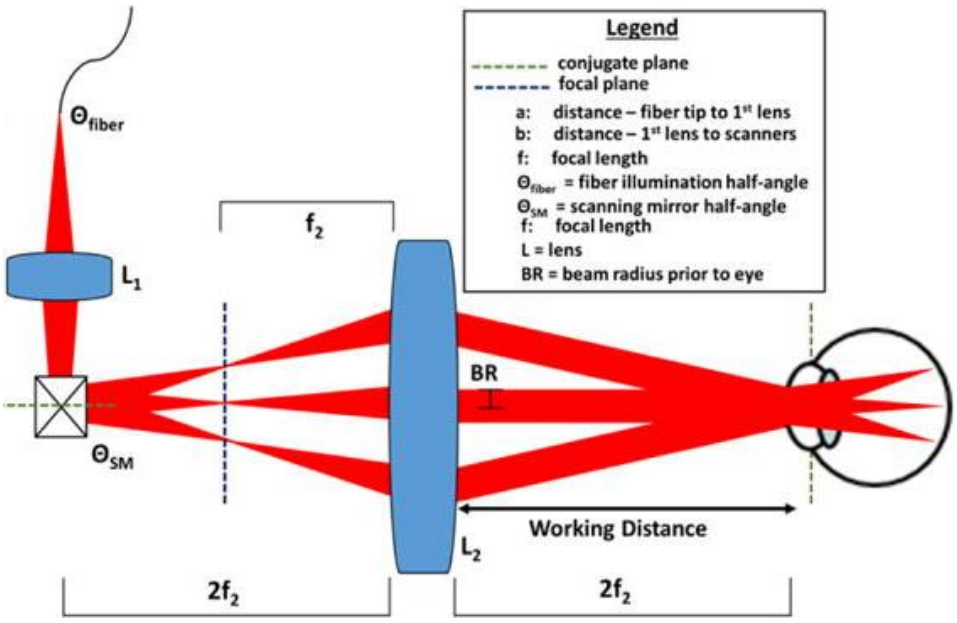

Figure 2: Schematic of a novel 2f retinal OCT scanner design enabled by delivering converging light into a single 2f refractive relay.

2.3.2 Human Imaging

The prospective *in vivo* human study was approved by the Duke University Medical Center Institutional Review Board, and it adhered to the Health Insurance Portability and Accountability Act and all tenets of the Declaration of Helsinki. Healthy volunteers and patients, both adults and children, were enrolled after obtaining written informed consent from either the participant or from the legal guardian of the participant after explanation of the potential risks of the study. Eligible eyes for this pilot study could be healthy or exhibit pathology, and all eligible eyes were required to have media adequate for imaging and reasonable visual function (eyes with dense amblyopia or no light perception (NLP) vision were excluded). The optical power incident on the cornea at 1040 nm was measured at below 1.7 mW before and after all imaging sessions,

which was well under the maximum permissible exposure determined by ANSI safety standards.

Images centered on the fovea and on the optic nerve head were attempted in each eye using the following protocol: B-scans comprised of 800 A-scans/B-scan and volumetric scans comprised of 800 A-scans/B-scan and 96 B-scans/volume. Radial scans with 800 A-scans/B-scan and 24 B-scans were also attempted in the adults and teenagers, but not in the group of young children due to the restricted imaging session time. The B-scan, volume, and radial scan frame rates were 125 Hz, 1.3 Hz, and 5.2Hz, respectively.

The prospective study consisted of four sequential stages. In stage 1, the prototype LWD-OCT system was used to obtain images in 10 adults, with or without retinal pathology, to optimize the system design and imaging protocol. In stage 2, LWD-OCT imaging was obtained in 16 adults (8 with pathology and 8 without pathology). In stage 3, LWD-OCT imaging was obtained in 16 children aged 13-18 (called teenagers for the rest manuscript, 8 with pathology and 8 without pathology). In the last stage, to test the feasibility of imaging in young children without a need for sedation and supine positioning, LWD-OCT imaging was obtained in children under 6 years of age (called young children for the rest chapter). To proceed from one stage to the next, a minimum of 80% of the scans for each scan type had to be graded as "good". The grading protocol is detailed in the Data Analysis section.

Alignment Protocol

Adults in the study (stages 1 & 2) were aligned both laterally and axially using a chinrest mounted on a slit-lamp base. The green dot overlaid on the pupil camera images displayed on a computer monitor denoted the lateral position of OCT beam to facilitate lateral alignment (Figure 3(a)). For initial axial alignment, the participant's head was translated until the pupil was in focus on the displayed pupil camera images. The final alignment was performed based on the real-time OCT images displayed on the custom software.

The final goal of the study was to align and image young children without a chinrest, since children are inherently afraid of objects, including chinrests and slit-lamps, close to their face. In stage 3 of this study, the teenagers were imaged without a chinrest and the participant's head was gently held by the operator to align the system (Figure 3(a)). The OCT system was also placed on a motorized table with an adjustable height to help facilitate vertical alignment. In stage 4 of the study, children aged 4 to 6 years were aligned in a similar method to that used for teenagers. Children under 4 years of aged sat on the parent's lap during alignment (Figure 3(b)). With guidance from the OCT operator, the parent then adjusted the child's body and head position to align the system based on the pupil camera image feedback. The LCD screen displayed

fixation cartoons to attract the child's attention.

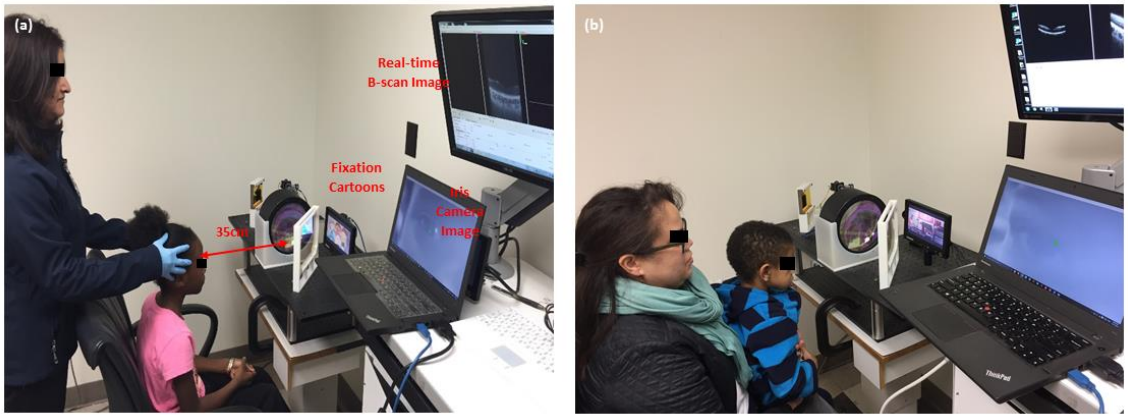

Figure 3: Demonstrations of the typical positioning of older and younger children with the imaging system. (a) A 9-year-old child aligned with the system by the operator. (b) A 2-year-old child seated in the parent's lap and aligned by the parent. (All photographs with parental permission.) The green dot on the pupil camera image indicates the location of the OCT beam.

Survey

A survey study was conducted with the participant after the imaging session. For the young child under 4 years of age, the survey was conducted with the participant's legal guardian. The survey consists of four questions, which are listed below.

1. Was the imaging session too long? (Yes/No for the first ten adult participants, and too long/acceptable/excellent for the rest participants)
2. Was the fixation difficult? (Yes/No for the first ten adult participants, and hard/okay/easy for the rest participants)
3. Was it difficult to hold steady for imaging? (Not included in the survey of first ten adult participants, hard/okay/easy for the rest participants)

4. Was the imaging session uncomfortable? (Yes/No for the first ten adult participants, and uncomfortable/okay/comfortable for the rest participants)

Volume Motion Artifact Correction

Despite improvement in the imaging acquisition speed with swept source OCT system, artifacts due to the participant's motion were still present in the volumetric images and degraded the quality of the acquired volumes. Additionally, motion artifacts were more noticeable when aligning the participant without a chinrest (stages 3&4) compared to when using a chin rest (stages 1&2), which is the convention method of alignment for clinical OCT system. Without a chin rest, axial motion was more noticeable since the child's head was gently stabilized laterally (by the imager or parent) without forehead support. Motion artifacts in acquired volume, were corrected in post-processing using the following correction algorithm specifically written in MATLAB (Mathworks,Natick, MA) for this study:

1. Lateral and axial motion between subsequent B-scans was estimated from the peak of the cross-correlation between them, and all B-scans were registered to the first one used as a key frame.
2. The top of the inner segment/outer segment (IS/OS) junction layer in the central B-scan of fovea in the volumetric image was segmented[68] to obtain an estimate of retinal curvature.

3. To recover the approximate retinal curvature in the slow scan direction, all B-scans were axially shifted to match the estimated retinal curvature in the slow scanning axis.

The motion artifact algorithm is illustrated in Figure 4 with representative volumetric foveal images of a 6-year-old child. All OCT volumes acquired in the study with significant axial motion artifacts were corrected using the algorithm described above. The motion artifacts in the volume of optic nerve head were also corrected in post-processing using the step 1 of the above algorithm.

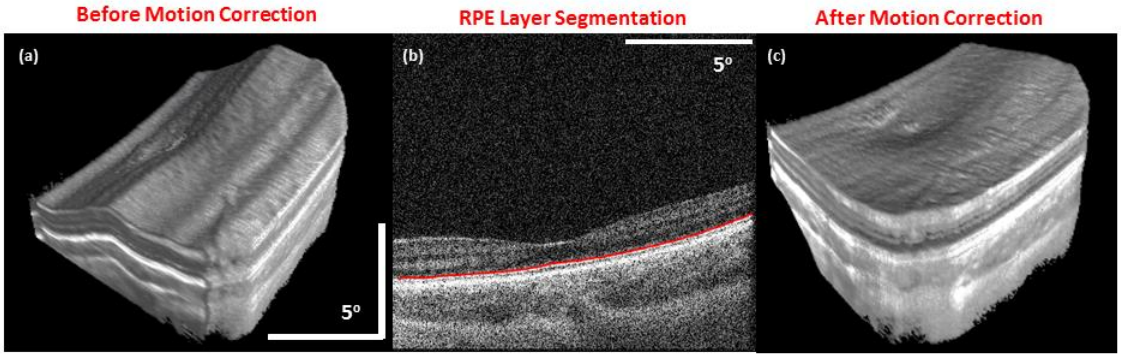

Figure 4: The illustration of the volume motion correction algorithm. (a) Volumetric image centered on the fovea of a 6-year-old child before motion correction. (b) Single B-scan at the center of the fovea with a segmentation line (red) at the top of the IS/OS band. (c) The same volumetric image after motion correction.

Data Analysis

The B-scans and OCT volumes of the first ten adult participants acquired were graded by two independent graders based on four categories: lateral centration and axial centration of fovea or optic nerve head, contrast and resolution. A scoring system was

devised and each category was given a mark: 2 for high quality, 1 for acceptable or 0 for unacceptable scans. Analysis of results showed that there was 100% intergrader agreement on scoring of each type of scans of all ten adult participants, therefore the rest of the images were graded by a single grader (SM) based on this scoring system. The total score was defined as a sum of all categorical marks and the highest attainable score was 8. The scan was deemed high quality if the total score was 7 or 8 and the scan was deemed acceptable if the score was 5 or greater. For the overall quality of the volumetric image, the grade was given for the best single B-scan in the volume. Further, the best foveal scan acquired from each eye was chosen to assess the presence of retinal layers and pathology at the fovea. Similarly, for the optic nerve scans, the overall volume, as well as the ability to capture the entire optic nerve was assessed.

To address a primary outcome of whether successful imaging was possible with this system, we recorded the percentage of eligible eyes that were successfully imaged with LWD-OCT. To address the second primary outcome of whether high-quality images of fovea and optic nerve head could be acquired with LWD-OCT, the average score of each imaged eye was calculated by averaging the scores of three categories of images: B-scans of fovea, volumes of fovea and optic nerve head. The radial scans of fovea were not included in calculating the average scores since they were acquired only in the adults and teenagers. To address a secondary outcome of whether the quality of captured images was comparable across age groups, the Wilcoxon signed-rank test was

used to compare the average grading scores for pairs of age groups (adults vs. teenagers vs. young children) to assess whether image quality of LWD-OCT prototype system is consistent among all the age groups. The null hypothesis was that image quality scores were not significantly different among all age groups, and a P-value lower than 0.05 was deemed statistically significant.

The alignment time was another key parameter used to assess the performance of the prototype system, especially in pediatric imaging. The alignment start time was defined as the time point when the imager first obtained rough alignment of the participant's pupil within the field of view of the pupil camera, and commenced acquisition of B-scan images. The alignment stop time was defined as clear and constant visualization of fovea in the real-time B-scan images.

2.4 Results

2.4.1. Lens and System Design

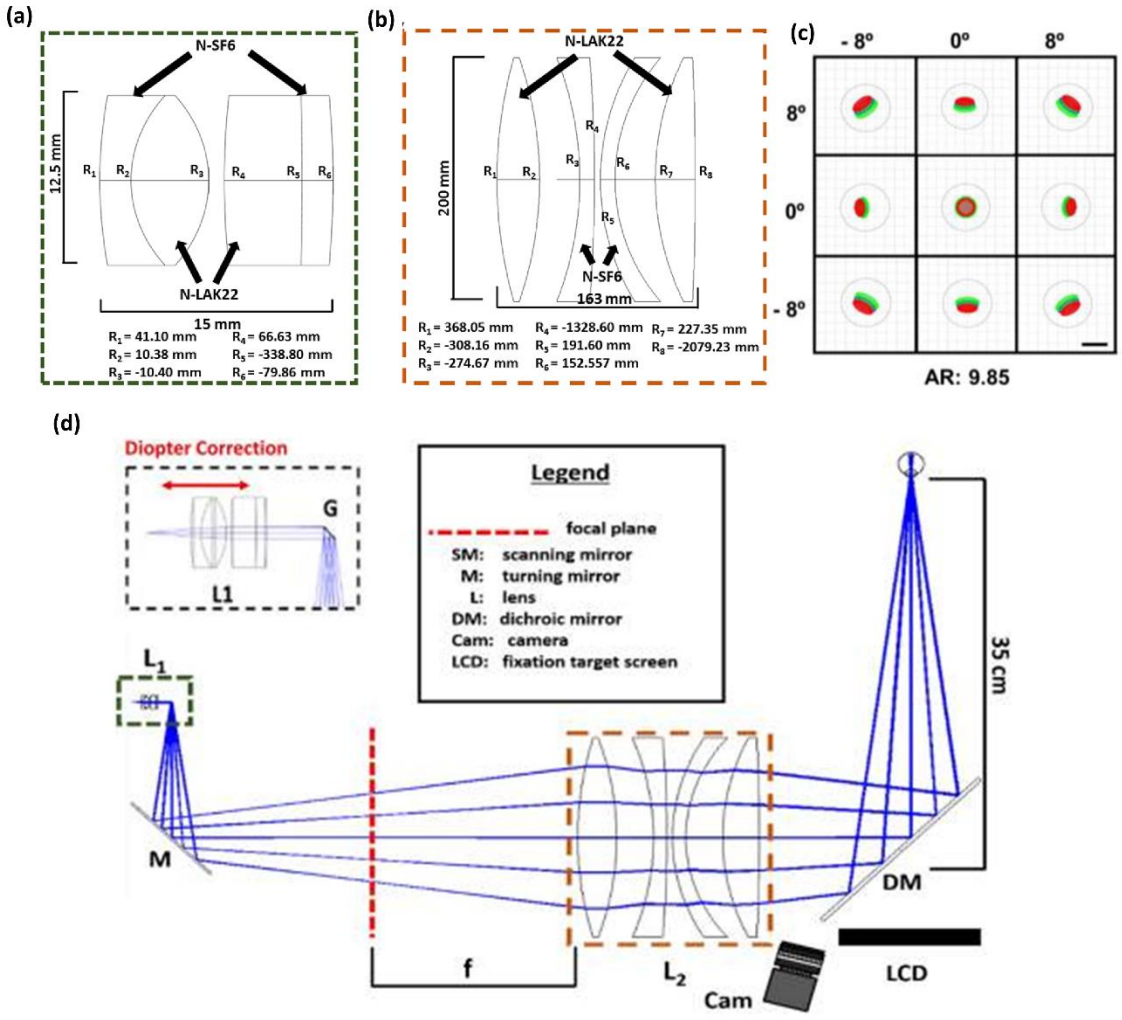

Figure 5 Optical design of the 2*f* sample arm. (a-b) Detailed lens design of L_1 (a) and L_2 (b); (c) spot diagram at the retinal plane of a schematic eye, AR=airy disk; (d) complete optical design with defined parameters and distances.

To optimize lateral resolution at the retinal plane, the 2f design employed two custom-designed lenses (L1 and L2) shown in Fig.5(a-b). The lenses were designed in

ray tracing software (Zemax, LLC; Kirkland, WA), and the diameter, thickness, and surface curvature of each element was optimized to minimize aberrations and achieve our design goal of 10 μm diffraction-limited lateral resolution at the retinal plane across +/− 8° FOV. Achromatic doublets were chosen to minimize the optical power of each individual element and reduce chromatic aberrations. The surface curvatures and thicknesses of each element in L1 were allowed to vary during the design optimization process to achieve diffraction-limited focusing at the intermediate image plane (red line in Fig.3(d) using the RMS spot size as our optimization metric. Similarly, the design of L2 was optimized by allowing the curvatures, thicknesses, and distances between elements to vary to achieve collimated light at the ocular pupil plane using the RMS angular spot radius as the optimization metric. Finally, we employed a schematic eye model [69] at the ocular pupil plane and optimized both L1 and L2 using the same degrees of freedom previously noted to minimize the RMS spot size at the retinal plane. Due to the large size of L2, compensating for refractive error by axially translating the lens was impractical. Instead, the fiber tip was translated axially relative to L1 to vary the beam vergence prior to the cornea to refocus the OCT beam at the retinal plane. The optical design achieved a simulated refractive error correction range of +5 to −8 diopters by translating the fiber tip from – 0.8 mm to 1.1 mm. Overall, the working distance of the system (from the dichroic mirror to the participant's pupil) was 350 mm with a maximum scanning angle of 16°, limited by the diameter of L2, with a lateral resolution

of <10 μm over the entire angular scan range (Fig.5(c)). Prominent aberrations present at the retinal plane of the schematic eye in both designs were transverse chromatic and spherical aberrations.

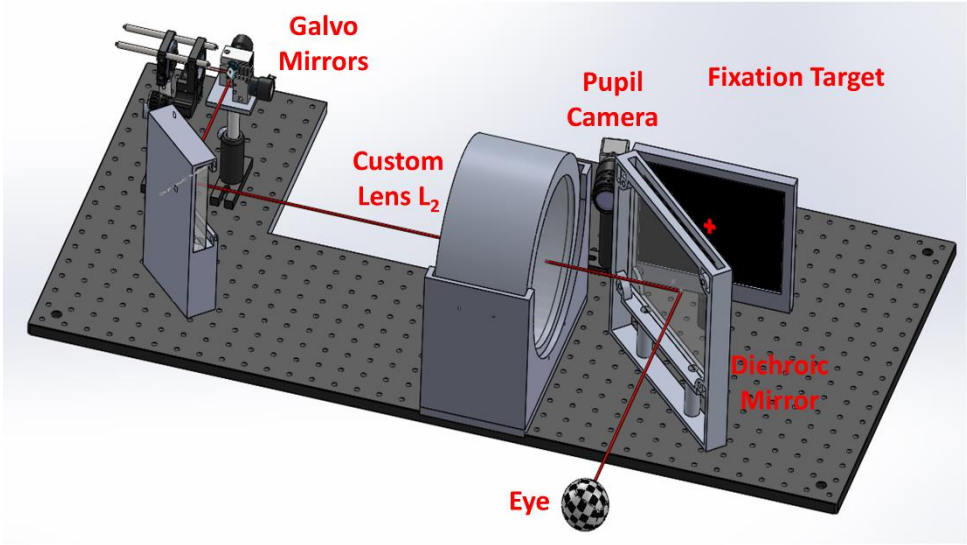

Figure 6: The optomechanical design of the OCT system and the fixation system.

The optomechanical design of the OCT system and the fixation system is shown in Fig.6. A liquid crystal display (LCD) screen (Lilliput Electronics, Inc., City of Industry, CA) was coaligned with the OCT system using a custom dichroic mirror (DM; OPCO Laboratory, Inc., Fitchburg, MA) and displayed a crosshair target to facilitate fixation during imaging of adults and older children. During imaging of young children, the LCD screen displayed animation videos selected before the imaging session by each child based on his or her preference. Additionally, a pupil camera (Point Grey Research, Inc., Richmond, Canada) was used to facilitate initial lateral and axial alignment of the

ocular pupil to the OCT beam. A green marker overlaid on the live pupil camera frames denoted the lateral position of the OCT beam.

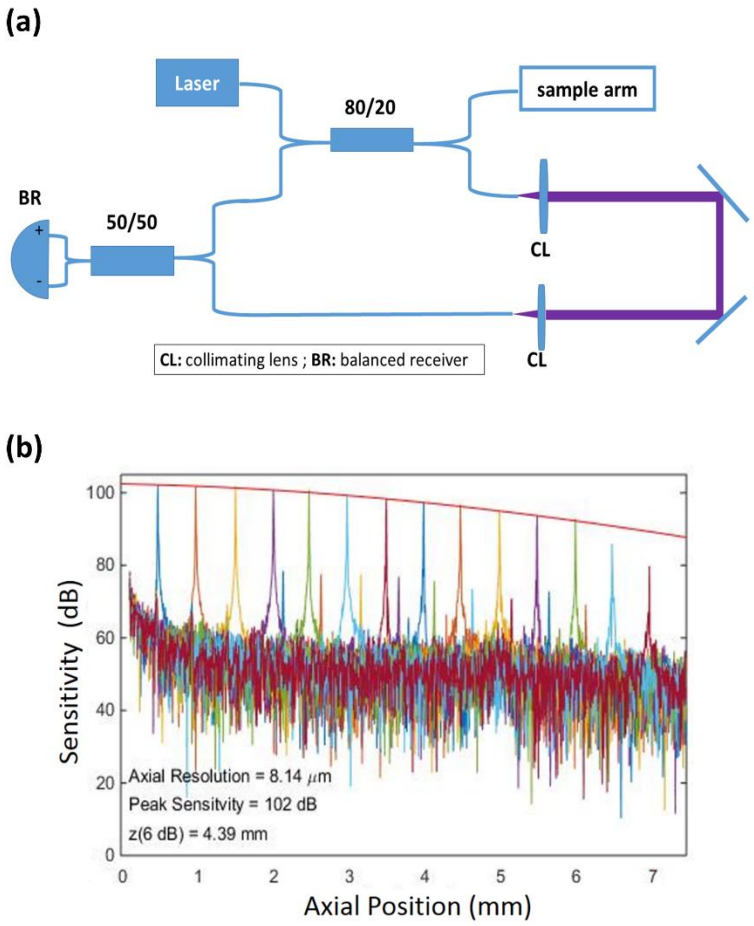

Figure 7: The OCT engine design and performance. (a) SS-OCT system with a transmission reference arm interferometer; (b) Sensitivity fall-off and axial resolution measurements of the system

The swept source OCT engine used a 1040 nm, 100 kHz swept laser source and a transmissive reference arm interferometer (Fig.7(a)). The system achieved an axial resolution of 8.12 μm across the entire depth range of 7.4mm, and a peak sensitivity of

102dB with a 6dB imaging range of 4.39mm (Fig.7(b)). The custom graphic processing unit (GPU) accelerated custom software enabled real-time volumetric imaging at 100k A-scans/second [70].

2.4.2 Human Imaging

We enrolled 26 adults (10 with pathology and 16 without pathology), 16 teenagers (8 with pathology and 8 without pathology) and 7 young children (4 with pathology and 3 without pathology) in this prospective study.

The total number of participants, eyes, and eyes with acquired images of each age group are shown in Table 1. In 4 of the young children (21 months, 2 years, 2 years and 3 years old), one eye of each participant was excluded from the study due to unmeasurable low vision with amblyopia, retinoschisis detachment with scarring, no light perception with massive coloboma, or parents' decisions not to proceed with research imaging.

Of all of the study eligible eyes, 50 of 52 adult eyes (96.2%) and 29 of 30 teenager eyes (96.9%) were successfully imaged. Among the adults, two eyes from one participant were not successfully imaged due to a temporary system malfunction. Among the teenagers, one eye was not successfully imaged due to the participant had very high diopter (+23D) customized contact lens. Among the young children with eligible eyes, 3 eyes from two children (13 months and 2 years old), were not successfully imaged, as

they were uncooperative and unable to maintain fixation. The youngest child that was successfully imaged was 21 months old.

Table 1: Number of enrolled participants, eligible eyes, and eyes that were successfully imaged in the LWD-OCT study.

Age Group (years)	Total number of participants	Total number of eligible eyes	Total number of eyes with acquired images N (%)
Adults	26	52	50 (96.2)
Teenagers (13-18yrs)	16	32	31 (96.9)
Young children (13 mos-6 yrs)	7	10	7 (70)

Young Children Imaging

Representative B-scans and volumes of fovea and optic nerve head of normal participants in the group of children under age of 6 are shown in the Figure 8(a-d). Retinal pathology, such as optic nerve head elevation, OPL disruption, retinoschisis and subretinal fluid were also successfully identified in the pediatric group using the prototype system. Some representative B-scans and volumetric images with pathology are shown in the Figure 8 (e-h).

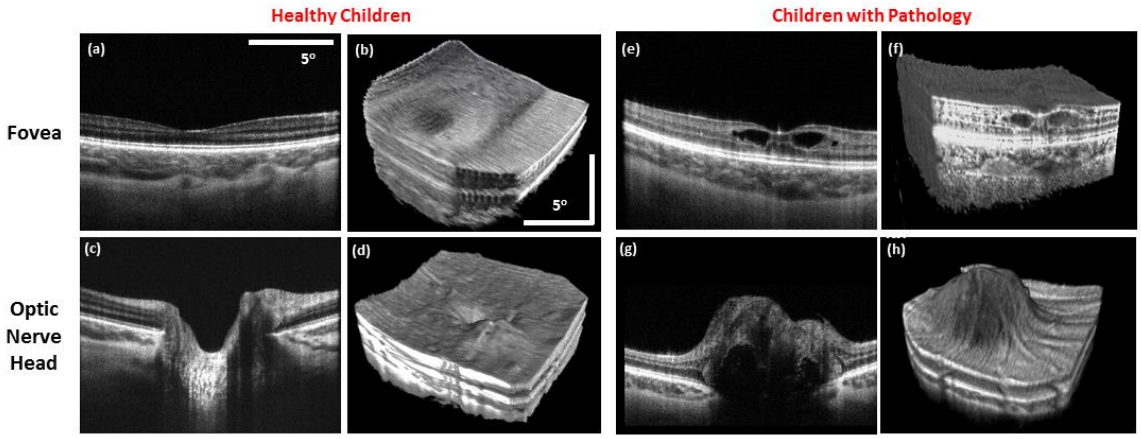

Figure 8: Representative SSOCT images acquired from a teenager and young child with and without pathology are illustrated and obtained with the prototype system. (a) Ten averaged B-scans of a healthy 6-year-old child. (b) Volume of the fovea of a healthy 2-year-old child. (c, d) Ten averaged B-scans and volume of optic nerve of a healthy 6-year-old child. (e, f) Ten averaged B-scans and the cross section of volume of a 5-year-old child with retinoschisis. (g, h) Ten averaged B-scans and volume of a 16-year-old child with optic nerve head elevation. All B-scans and volumetric images here were graded as high-quality scans.

Imaging Grading

Among all the successfully imaging sessions, the overall percentages of images with grading scores higher than or equal to 7 (good scans) of each age group are 82%, 84% and 86%. The average score of the adults group (n=50) is 7.29 ±1.01. The average score of teenagers (n=31) is 7.24±1.39, and the average grade of young children (n=7) is 7.31 ± 1.00, and image quality of different age groups did not have significant differences by two-sided Wilcoxon rank sum test (Figure 9). Note that the two enrolled eye of adults and the three enrolled eyes of young children that were not successfully imaged were excluded from statistical analysis of grading.

Table 2: Results of grading of SSOCT images for each age group in this LWD-OCT study

Age group (number of eyes with scans)	Acceptable scans percentage (% with score ≥ 5)					High quality scans percentage (% with score ≥ 7)				
	Foveal B-scans	Foveal volume	Foveal radial scans	Optic nerve	Overall	Foveal B-scans	Foveal volume	Foveal radial scans	Optic nerve	Overall
Adults (n= 50)	98%	96%	96%	100%	98%	82%	86%	82%	93%	82%
Teenagers (n=31)	100%	97%	100%	93%	97%	90%	80%	85%	87%	84%
Young Children (n=7)	100%	83%	-	100%	100%	86%	83%	-	100%	86%
Total (n=88)	99%	96%	97%	97%	97%	85%	84%	83%	91%	83 %

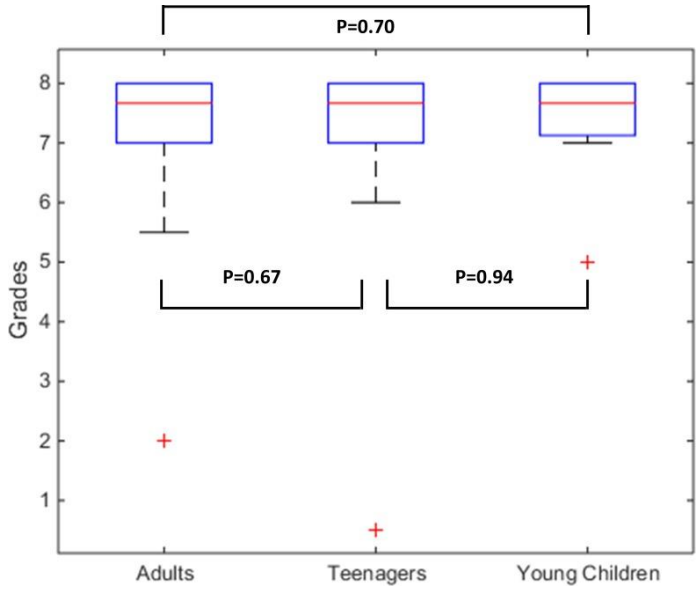

Figure 9: Boxplot of image grading scores of three age groups in the study, and results of the Wilcoxon rank sum test between every pair of two age groups. Outliers are defined as the scores larger than 1.5 times the interquartile range of the box.

System Alignment

An important parameter to evaluate the difficulty of alignment is alignment time (defined in the methods section). The alignment time of 38 eyes of adults, 6 eyes of teenagers and 7 eyes of young children were measured (Figure 10). It should be noticed that the alignment time of first 8 eyes in the study was relatively longer, because the green dot marker in the pupil camera image indicating the OCT beam location was not fully calibrated. Additionally, the examiner was not experienced in operating the system in the initial part of the study. As a result, the alignment time of the first 8 eyes were excluded from the statistical analysis below.

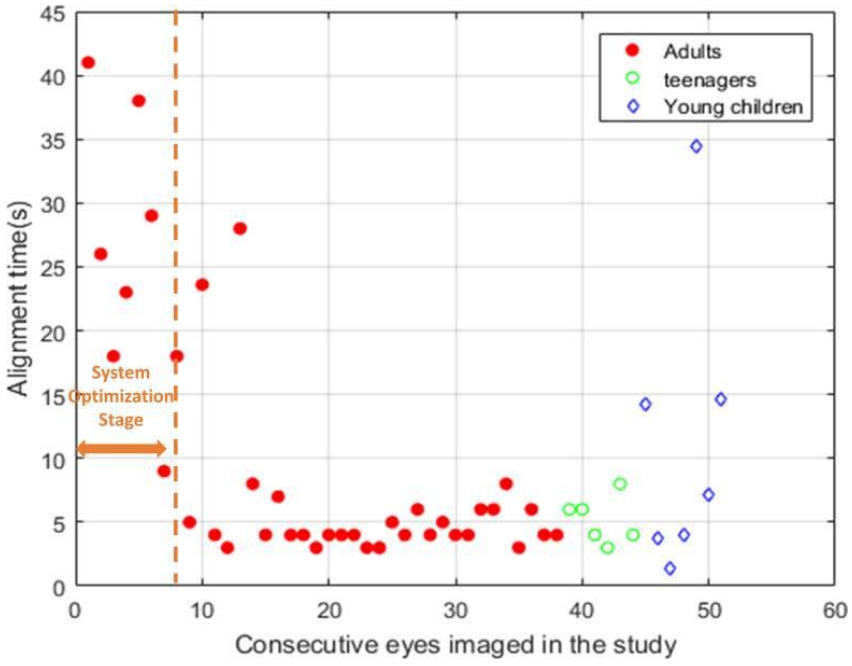

Figure 10: Alignment time of 38 eyes of adults (red dots), six eyes of teenagers (green circles), and seven eyes of young children (blue diamonds).

The average alignment time across all three age groups (n=43) was 6.8 ± 6.7s. The average alignment time of adults (red dots in Figure 9, n=30), teenagers (green circles in Figure 6, n=6) alignment time of young children (blue diamonds in Figure 9, n=7) were 6.0 ± 5.6s, 5.2± 1.8s and 11.4s ± 11.4s. It should be noticed that the average alignment time of young children was calculated based on 7 of 10 eyes that were successfully imaged.

Survey Outcomes

Table 3: The survey results of each age group in this LWD-OCT study

<table>
<tr><th></th><th></th><th>First 10 Adults N (%)</th><th>The rest Adults N (%)</th><th>Teenagers N (%)</th><th>Young Children N (%)</th><th>Total* N (%)</th></tr>
<tr><td rowspan="2">Was imaging session too long?</td><td>Yes</td><td>2(20%)</td><td>1(6%)</td><td>0(0%)</td><td>0(0%)</td><td>3(6%)</td></tr>
<tr><td>Acceptable</td><td rowspan="2">8(80%)</td><td>12(75%)</td><td>13(81%)</td><td>6(86%)</td><td rowspan="2">46(94%)</td></tr>
<tr><td>Excellent</td><td>3(19%)</td><td>3(19%)</td><td>1(14%)</td></tr>
<tr><td rowspan="3">Was the fixation difficult?</td><td>Hard</td><td>0(0%)</td><td>0(0%)</td><td>0(0%)</td><td>2(29%)</td><td>2(4%)</td></tr>
<tr><td>Okay</td><td rowspan="2">10 (100%)</td><td>2(13%)</td><td>5(31%)</td><td>2(29%)</td><td rowspan="2">47(96%)</td></tr>
<tr><td>Easy</td><td>14(87%)</td><td>11(69%)</td><td>3(43%)</td></tr>
<tr><td rowspan="3">Was it difficult to hold steady for imaging?</td><td>Hard</td><td rowspan="3">N/A</td><td>1(6%)</td><td>1(6%)</td><td>2(29%)</td><td>4(10%)</td></tr>
<tr><td>OK</td><td>4(25%)</td><td>6(38%)</td><td>4(57%)</td><td>14(36%)</td></tr>
<tr><td>Easy</td><td>11(69%)</td><td>9(56%)</td><td>1(14%)</td><td>21(54%)</td></tr>
<tr><td>Was the imaging</td><td>Uncomfortable</td><td>2(20%)</td><td>1(6%)</td><td>0(0%)</td><td>0(0%)</td><td>3(6%)</td></tr>
</table>

session comfortable ?	Okay	8(80%)	3(19%)	6(37%)	3(43%)	46(94%)
	Comfortable		12(75%)	10(63%)	4(57%)	

* To combine the survey results of the first ten adult participants with the rest participants in this column, we collapsed acceptable/excellent imaging session time (Question 1), okay and easy fixation (Question 2), and comfortable and okay imaging session (Question 4).

All 49 participants were enrolled in the survey. 46 of 49 (94%) participants in total, including all 7 young children (100%) participants indicated that the imaging time was not too long. All 3 participants who considered the imaging time too long were the participants during in the optimization stage of the study. 47 of 49 (96%) participants in total, including 5 of 7 young children participants (71%) did not feel that fixation was difficult to achieve and maintain. Two young children, whose parents considered the fixation difficult, were the participants in which OCT images were not successfully acquired. 35 of 39 (90%) participants, including 5 of 7 young children, didn't think holding steady during the imaging session was too hard. It should be noted that this question was not included in the survey of first ten adult participants, which lead the total number of participants' feedback of this question to be 39 instead of 49. 15 of all 18 participants (83%) who were imaged as the imager gently held participants' head (Figure 5(a)), considered it easy or okay to hold steady, while the parents of 4 of 5 (80%)

young children participants under 4 years of age who were situated in parents' laps (Figure 5(b)) considered it easy or OK to hold steady. 46 of 49 (94%) participants in total including all 7 young children participants, thought the overall imaging session was OK or comfortable.

2.5 Discussion

In this study, we demonstrated the use of a prototype LWD-OCT system with a working distance of 350 mm to image young children under 6 years of age without sedation and chinrest and with a reasonable alignment time. OCT systems with long working distances have been previously developed for endoscopic imaging probes (up to 80mm)[71] for tissue imaging and microscope integrated OCT systems (up to 175 mm)[72-74] for intraoperative imaging. To our knowledge, this is the longest working distance OCT system that has been reported. The 2f optical relay, which has been previously implemented in scanning laser ophthalmoscopes (SLO)[75, 76] and adaptive optics SLO[77], greatly reduced the footprint and weight of the system. The system also employed a 100KHz swept source, which has a faster A-scan rate than most commercial spectral domain OCT systems, and it allows volumetric imaging of retina in as shorter imaging time with less motion artifacts.

The current study was conducted in three age groups: adults, teenagers and young children. In young children, we were only able to image 7 of 10 eyes with this system. It is important to note that in one of these children aged 21 months old,

however, no clinical OCT imaging was possible due to the participant's inability to fixate in front of the tabletop system, yet we were able to image the macula with the LWD OCT system.

For the eyes in which OCT images were successfully acquired, there was no significant difference in image quality grades between the age groups with 5% significance levels, and the overall percentages of high-quality scans were higher than 80% for each age group. While cooperation was still a challenge in two young children (3 eyes) when using the current tabletop setup, when images could be captured, they were generally very high-quality volume and B-scan images of macula and optic nerve head. The mean alignment time was 11.4s for young children when OCT images were successfully captured, indicating the feasibility of alignment of young children and infants without the use of chinrest and supine position using LWD-OCT.

Handheld OCT probes have shown a great promise in young children and infant bedside imaging. However, handheld OCT imaging of young children and infants without use of sedation and supine position in general is difficult. In contrast, with our LWD-OCT system we have the ability to image young children while they were comfortable and with minimal restraint sitting on their parent's laps and watching cartoons on the LCD screen in front of them. In addition, our LWD-OCT system allowed participants to maintain a comfortable distance from the "intimidating" instrument.

One of the major limitations of our LWD-OCT system is the absence of an automatic tracking and alignment system, and it was the main reason why we didn't successfully image three eyes of young children in the study. The current system alignment relies on the participant's parents or examiners gently holding and adjusting the position of the participants' head as well as the operator adjusting the height of the instrument table based on the feedback from the pupil camera and the real-time OCT images. These requirements to acquire high quality images in children may increase alignment difficulty and introduce more motion artifacts. Future work may include placing the OCT sample arm on a three dimensional motorized translational stage, using additional methods to detect fixation[78], and implementing the pupil tracking technology into the current prototype system[79], so that the system can be aligned with the participant automatically based on the pupil position extracted from the pupil tracking system, and the alignment time could potentially be reduced. An automatic tracking and alignment system can potentially facilitate LWD-OCT imaging of young uncooperative children.

In the study, we also noticed that our current fixation targets and cartoon movies sometimes did not attract the child's attention, especially when imaging children less than 3 years of age. Moreover, the visible prototype optical elements such as the large objective lens distracted the child from the fixation movies. In the future, more age specific fixation targets or cartoon movies will be used[80]. Additionally, all the optical

elements of the system will be housed in an enclosure to ensure the participant not get distracted.

Another limitation is the motion artifacts in volumetric images. The motion artifacts were inevitable as the participants were imaged without a chinrest and positioned further away from the system compared to the conventional tabletop OCT systems. We applied a motion artifact correction algorithm to correct axial and lateral motion along the B-scan direction in the volume as shown above (Figure 6). Although the algorithm partially compensated for participant motion during image acquisition in order to generate high quality image volumes, it made several assumptions (such as that the retinal curvature in fast and slow OCT acquisition directions was the same) that should limit extraction of quantitative morphological data from the acquired image volumes. Additionally, other motion artifacts such as lateral and rotational motion out of the B-scan plane could not be corrected using the current setting, which may affect the visualization of volumes. A more robust method to remove motion artifacts in volumes is to use an orthogonal scan pattern[81, 82], which will be considered in future studies.

Another potential improvement would be to employ an OCT light source with much longer instantaneous coherence length, such as a vertical cavity surface-emitting laser (VCSEL), which has a theoretical imaging range of more than one meter[83], compared to 7.4mm in our current prototype system. In general, the axial alignment of the LWD-OCT system is more difficult than with a conventional tabletop OCT system,

since the participant's eye is much further away from the system and not fixed by the chinrest. A much longer imaging range could potentially help the imager locate the participant's axial position much easily, however such light sources and the related acquisition systems are not yet clinically viable.

In summary, we successfully captured high quality retinal images of adults, teenagers and young children with and without pathology using our prototype LWD-OCT system. Furthermore, we successfully imaged children as young as 21 months old without sedation in clinic. Additional studies such as comparative studies among the LWD, the conventional tabletop and the handheld probe OCT system, are needed to further validate the utility of our prototype.

2.6 Summary

In this work, we demonstrate a prototype retinal swept-source OCT system with a long working distance (from the last optical element to the subject's eye) to facilitate pediatric imaging. To reduce the number of optical elements and axial length compared to the traditional 4f telescope, we employ a compact 2f retinal scanning configuration and achieve a working distance of 350 mm with a 16° OCT field of view. In the following clinical study, the LWD-OCT imaging was successfully performed on 88 of 94 eligible eyes, including seven of 10 eyes of young children. Of the successfully acquired OCT images, 83% of B-scan and volumetric images, including 86% from young children, were graded as high-quality scans. Pathology was observed in high-quality OCT images.

Overall, the prototype LWD-OCT system achieved high quality retinal imaging of young children with and without pathology with reasonable alignment time, and the system can potentially facilitate imaging in children.

3. Anterior Chamber Blood Cell Differentiation Using Spectroscopic OCT

3.1 Abstract

There is potential clinical significance in identifying cellular responses in the anterior chamber (AC) of the eye, which can indicate hyphema (an accumulation of red blood cells [RBCs]) or aberrant intraocular inflammation (an accumulation of white blood cells [WBCs]). In this work, we developed a spectroscopic OCT analysis method to differentiate between populations of RBCs and subtypes of WBCs, including granulocytes, lymphocytes and monocytes, both *in vitro* and in ACs of porcine eyes. We developed an algorithm to track single cells within OCT datasets, and extracted the backscatter reflectance spectrum of each single cell from the detected interferograms using the short-time Fourier transform (STFT). A look-up table of Mie back-scattering spectra was generated and used to correlate the backscatter spectral features of single cells to their characteristic sizes. The extracted size distributions based on the best Mie spectra fit were significantly different between each cell type. We also studied theoretical backscattering models of single RBCs to further validate our experimental results. The described work is a promising step towards clinically differentiating and quantifying AC blood cell types.

3.2 Background

There are many diseases associated with cellular response in the anterior chamber (AC) of the eye, the anatomical space between the cornea and the iris which is occupied by the aqueous humor. For example, hyphema is a collection of red blood cells (RBCs) inside the AC, which can occur after blunt trauma, after intraocular surgery, or spontaneously [84]. On the other hand, anterior uveitis, the most common form of intraocular inflammation, causes an accumulation of white blood cells (WBCs, also called leukocytes) in the ocular anterior chamber. Further, the subtype of WBC response may provide differentiating diagnostic information regarding the type of inflammation and hence the appropriate treatment. For instance, a predominant response of polymorphonuclear WBCs (also called granulocytes), mainly neutrophils, may suggest an endotoxin-induced or HLA-B27-associated acute uveitis [85, 86], while a predominant response of mononuclear WBCs, mainly lymphocytes and monocytes, may suggest sarcoidosis [87], Vogt–Koyanagi–Harada [88] and melanin-protein-induced uveitis [89]. The primary current diagnostic tool to examine the condition of the aqueous humor and evaluate the severity of these diseases is slit-lamp microscopy. Although specialists can recognize the presence or absence of these responses, subjective qualitative assessment of these conditions makes it difficult to judge the longitudinal course of the response. In addition, subtypes of WBCs, such as granulocytes, lymphocytes and monocytes, cannot be differentiated using clinical ophthalmic microscopy. The true composition of cells in

the aqueous humor can be obtained using AC paracentesis and flow cytometry [90]. However, AC paracentesis is an invasive procedure that requires a needle insertion and local anesthesia [91].

Optical coherence tomography (OCT) allows noninvasive, high-resolution cross-sectional imaging of the AC [92]. Several groups have investigated its potential in grading AC inflammation by locating and counting cells within anterior segment OCT (AS-OCT) images [93-97]. However, quantitative analysis of the true composition of cells using OCT remains a challenge. Healthy RBCs have a biconcave shape which is 7.5 to 8.7 μm in diameter and 1.7 to 2.2 μm in thickness [98], while WBCs are more globular with a mean diameter range from 6 to 20 μm [99]. Conventional, clinical AS-OCT systems have an axial resolution of ~5-10 μm in tissue, and a lateral resolution of tens of μms. Therefore, individual cells appear as indistinguishable hyper-reflective spots in conventional AS-OCT images [100]. Rose-Nussbaumer et al. have investigated differentiation of RBCs and subtypes of WBCs using the reflectance intensity in OCT images [100]. Although the average reflectance distribution of each cell type was shown to be different with statistical significance, cell reflectance in OCT images can be easily affected by many factors, such as illumination laser power, optical alignment, and cornea opacities. Ossowski et.al have developed a method to detect and differentiate moving RBCs and WBCs using phase-sensitive OCT in vitro; however, the method relies

on using a custom designed microfluidic device with a highly scattering substrate, and is difficult to implement in vivo [101].

The goal of this work is to develop a spectroscopic OCT analysis method to differentiate between populations of RBCs and subtypes of WBCs, including granulocytes, lymphocytes and monocytes. The proposed work can potentially provide quantitative diagnostic information of cellular responses in the ocular anterior chambers of patients in the clinic and expand the field's pathophysiologic knowledge about diseases such as anterior uveitis.

3.3 Methods

3.3.1 OCT system design

A custom swept-source OCT (SSOCT) system (Fig.1(a)) was built for this study. The system employed a 100-kHz swept-wavelength laser (Axsun Technologies; Billerca, MA), centered at 1052 nm with a sweeping range of 108 nm. The interferometric signal was detected with a dual-balanced receiver (Thorlabs, Inc.; Newton, NJ) with 1GHz electronic bandwidth and digitized at 800 MS/s (AlazarTech Inc.; Pointe-Claire, QC, Canada). The sample arm included a collimator lens, a pair of galvanometer scanning mirrors (Thorlabs, Inc.; Newton, NJ) and a telecentric imaging lens with a working distance of 75 mm (Fig 11(a)). The lateral resolution was measured to be 20 μm. The measured sensitivity and -6 dB fall off of the OCT system was 103 dB and 4.39 mm with 2.2mW illumination power on the sample, respectively (Fig.11(b)). The measured axial

resolution was constant over an imaging range of 5.5 mm with a mean full width at half maximum of ~8.8 μm (in air) (Fig.1(b)). The maximum imaging range of the system was 7.4mm. Custom GPU-based software enabled real-time acquisition, processing, and rendering of volumetric data at a 100-kHz A-line rate.

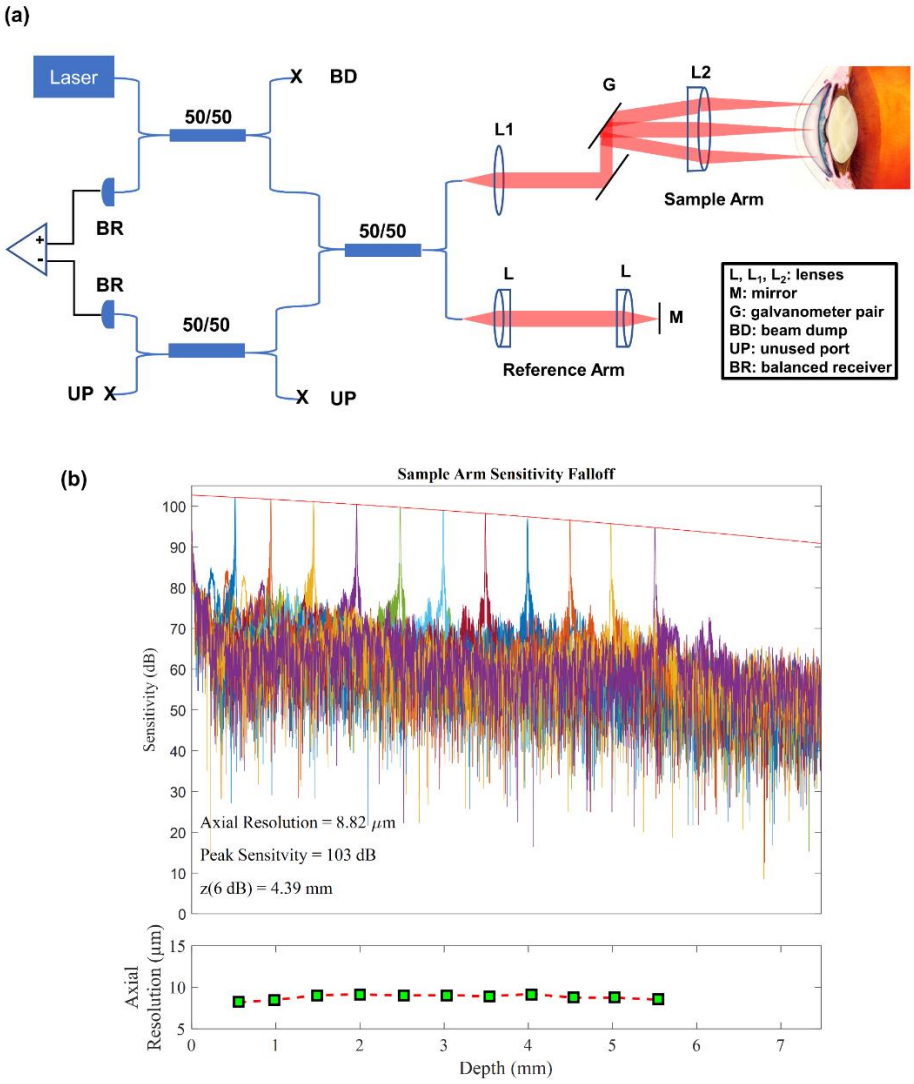

Figure 11: The custom OCT system design and performance evaluation.(a) Schematic diagram of the custom swept-source OCT system, and (b) fall off sensitivity performance and axial resolution of the system across an imaging range of

5.5mm. L, L_1, L_2: lenses, G: galvanometer scanner, M: mirror, BD: beam dump, UP: unused port, BR: balanced receiver

3.3.2 Phantom and Cell Preparation

***Ex vivo* Phantom Preparation**

To first demonstrate the feasibility of using spectroscopic OCT to distinguish cellular scale objects in the AC, approximately 0.1 mL 10 μm polystyrene microspheres with a particle density of 1.05 g/cm^3 (Thermo Scientific; Waltham, MA) were suspended in 5mL water and injected into the ACs of freshly enucleated porcine eyes (N=2).

***In vitro* Cell Preparation**

Fresh human RBC (N=3) and cryopreserved human WBC samples (ZenBio Inc.; Research Triangle Park, NC), including granulocytes (N=4), lymphocytes (N=3) and monocytes (N=3), from healthy donors were obtained. Cryopreserved WBC samples were rapidly thawed in a 37 °C water bath prior to use and suspended in phosphate-buffered saline (PBS) (Sigma-Aldrich; St. Louis, MO) solutions. Cryoprotectant was removed by centrifuging cell suspension at 400x g for 10 mins. The cell samples were then re-suspended in PBS solutions containing 0.1% bovine serum albumin (Sigma-Aldrich; St. Louis, MO) to a concentration of ~150 cells/mm^3, and transferred to the glass cuvettes for imaging.

***Ex vivo* Cell Preparation**

In the final experiment to mimic cell characterization in an in vivo environment, freshly enucleated porcine eyes obtained from a local slaughterhouse and stored at 4°C

were used, and human RBCs, granulocytes, lymphocytes and monocytes (obtained and prepared as in above section) were injected into the ACs of porcine eyes using a syringe for immediate imaging.

3.3.3 Data Acquisition

Due to the weak backscattering signal from single blood cells imaged by our system, we required between 20 and 30 repeated and averaged measurements from the same cell to achieve the necessary SNR for the following spectroscopic analysis (Fig. 3(c)-(d)). Unlike cells moving following a circulating aqueous humor flow pattern due to the natural temperature gradient in the eye [102], the flow patterns of in vitro or ex vivo cells can be affected by many factors, such as gravity, motion introduced during sample resuspension, and temperature gradients in the medium. Therefore, we found that two different OCT scan protocols, repeated B-scans and volumetric scans, were necessary, depending on the velocity and direction of cell movements observed in each sample, with the goal of keeping each single cell within the FOV in repeated scans and, at the same time, maximizing the FOV to capture more cells.

For the data reported in this study, we used either volumetric scans or repeated B-scans at the same location. For each sample, we first aligned the sample such that the system's B-scan direction was aligned along the dominant direction of cell motion (i.e., vertical due to gravity). Then, 50 repeated B-scans were acquired with 500 A-scans/B-scan, providing a FOV of 2 mm in the B-scan direction. For samples in which more than

50% of localized cells (according to the procedure described in Section 3.2.4) remained within the FOV for at least 20 repeated B-scans, the repeated B-scan data was used for further analysis.

For samples in which fewer than 50% of localized cells remained within the FOV for 20 repeated B-scans, a volumetric imaging window was utilized, particularly for freshly resuspended cells with higher and less uniform velocity, which were more likely to move out of the imaging plane in the B-scan mode. Instead, for these samples, 50 repeated OCT volumes were acquired with scan dimensions of 96 A-scans/B-scan and 48 B-scans/volume, and a lateral FOV of approximately 0.4 mm x 0.2 mm. The effective volume rate with these scan parameters was 22 Hz.

Both volumetric and repeated B-scan modes achieved nearly isotropic sampling resolution with a lateral sampling resolution of approximately 4 μm, and an axial sampling resolution of 5.4 μm.

3.3.4 Single Cell Localization and Tracking

In the repeated B-scan mode, individual cells within OCT image (Fig.12(a)) were first localized by creating a binary image using intensity thresholding (Fig.12(b)), then 8-connected component labeling was applied to detect connected regions in the binary image and assign labels to individual cells (Fig.12(c)). Additionally, if the distance between two cell labels were within 4 pixels, these two labels were combined as the label of the same cell. To differentiate cells from noise and exclude cells which were out of the

imaging plane, only connected-components larger than 6 pixels were considered as cells. We used the A-scan (Fig.13(a)) at the center of every labelled cell (Fig.12(d)) for further spectroscopic analysis.

For the volumetric OCT mode (Fig.12(a)), we performed the same processing as just described on each B-scan of each volume. If the distance between any centers of labels in two adjacent B-scans was less than or equal to 4 pixels, these two labels were combined as the label of the same cell. Similarly, we used the A-scan at the center of every labelled cell in the volume for further spectroscopic analysis.

To identify cells within sequentially acquired volumes, we compared whether the location of a cell in one volume corresponded with cell locations within a small voxel region in both the preceding and subsequent volume. If so, co-localized cell locations in sequential volumes were categorized as a single cell. The dimensions of the voxel regions were determined based on the moving speed of cells in each sample. The tracking of each cell stopped when it left the acquired volume. For B-scan mode, every single cell was tracked with a similar approach to locate cells in a neighborhood region. The cell was labelled to be out of the FOV when the peak cell intensity fell below a defined threshold value. Only cells staying in the FOV for at least 20 repeated B-scans or volumes were used for the following spectroscopic analysis.

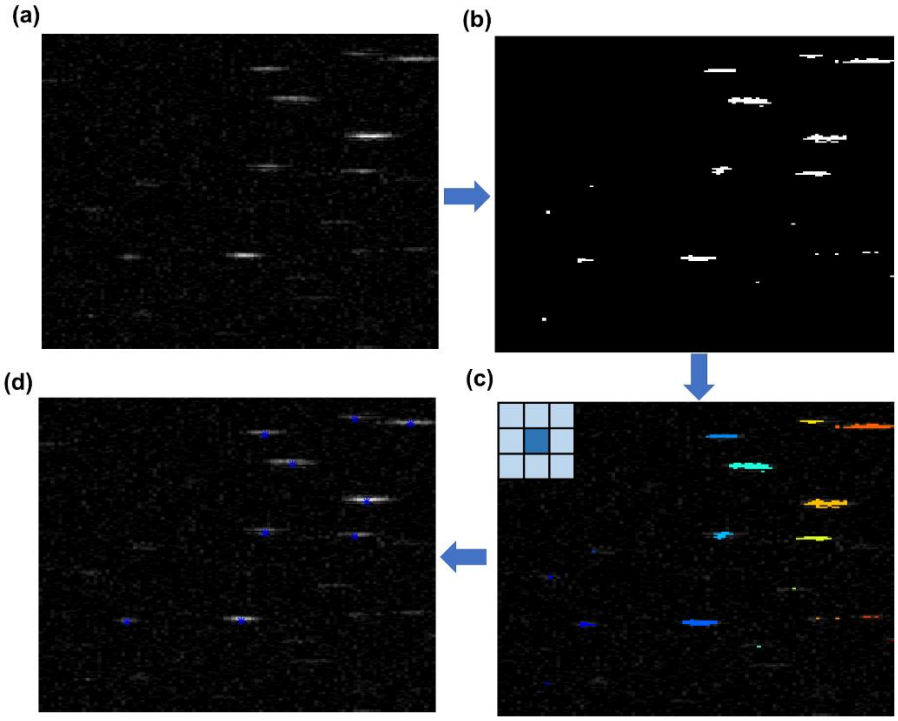

Figure 12: Single cell localization and tracking algorithm. (a) Representative B-scan of lymphocytes suspended in the cuvette; (b) Binary B-scan image after intensity thresholding; (c) Individual cell localization using 8-connected component labeling, with each cell assigned a different overlay color; (d) Same B-scan as (a) with the centers of cells labeled.

3.3.5 Spectroscopic Analysis

The ability to perform SOCT in Fourier-domain OCT using the STFT was first demonstrated by Letigeb et al. [103]. The signal intensity $I(k_o, z)$ extracted from the STFT of the detected interferogram $I_D(k)$ after linear wavenumber interpolation and DC subtraction can be expressed as

$$I(k_o, z) = \left| FT\left(I_D(k) W(k - k_o)\right) \right|, \tag{3}$$

where $W(k-k_o)$ is the window function centered at k_o and FT is the Fourier Transform. In this study, a Hamming window $W(k-k_o) = 0.54 + 0.46\cos(2\pi\frac{k-k_o}{\Delta k})$ with a spectral width Δk of 23.7 cm^{-1} was chosen, corresponding to an axial resolution of ~340 μm for each window. To perform the STFT, the window $W(k-k_o)$ was shifted across the acquired interferogram $I_D(k)$ a total of 100 times with a step size of 9.2 cm^{-1}. Unlike for some previous spectroscopic OCT applications, the inherent tradeoff in spectral and spatial resolution of the STFT was not a significant drawback here, since the sample of suspended cells was sufficiently sparse that the likelihood of having more than one cell within each depth window was low.

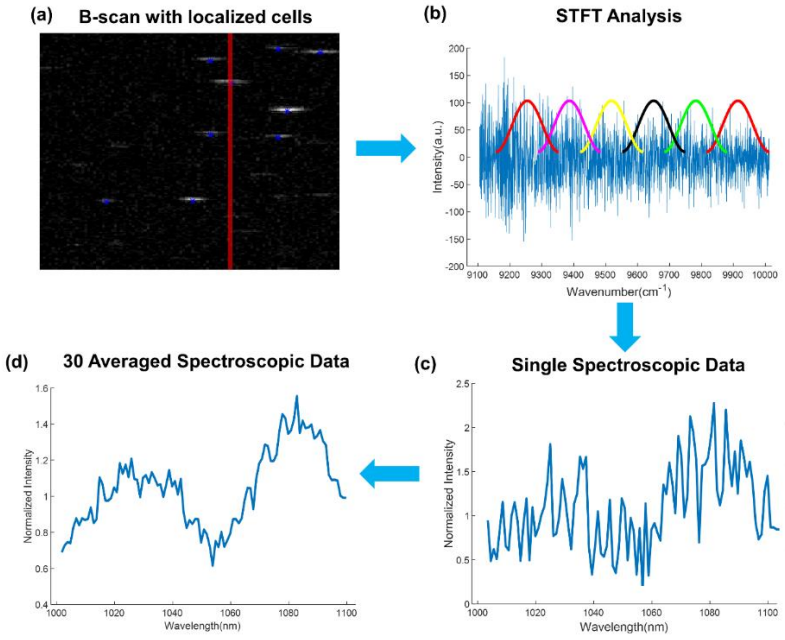

Figure 13: Spectroscopic analysis of single tracked cell in the OCT B-scan.(a) Representative OCT B-scan of a lymphocyte suspension with individual cells (white), their localized and tracked centers (blue), and an example A-scan used for spectroscopic analysys (red line); (b) STFT analysis of the red A-scan in (a) from a

localized cell; (c) single and (d) 30 averaged spectroscopic data extracted from a localized lymphocyte.

Assuming an optical path length difference between a point scatterer and reference arm is z_i, the detected interferogram $I_D(k)$ is proportional to $S(k)\sqrt{R_s(k)}\cos(2kz_i)$, where $S(k)$ is the laser power spectrum and $R_s(k)$ is the backscattering power spectrum of the scatterer [104]. Thus, the signal intensity $I(k_o, z)$ extracted from a window centered at k_o is

$$I(k_o, z) \propto \left| FT\left(S(k)\sqrt{R_s(k)}\cos(2kz_i)W(k-k_o)\right)\right| \ . \tag{4}$$

Assuming the backscattering power at the central wavenumber of the window, $R_s(k_o)$, is the averaged backscattering power $R_s(k)$ across that window, $[k_o - \Delta k/2, k_o + \Delta k/2]$, and ignoring the complex conjugate,

$$\begin{aligned} I(k_o, z>0) &\propto \sqrt{R_s(k_o)}\left|FT\big(S(k)W(k-k_o)\big) * \delta(z-z_i)\right| \\ &\propto \sqrt{R_s(k_o)}|PSF(k_o, z) * \delta(z-z_i)| \\ &\propto \sqrt{R_s(k_o)}|PSF(k_o, z-z_i)| \end{aligned} \tag{5}$$

Here $PSF(k_o, z) = FT\big(S(k)W(k-k_o)\big)$ is the coherence function or axial point-spread function (PSF) of the "windowed" source spectrum. Experimentally, we obtained $|PSF(k_o, 0)|$ by imaging a mirror with a uniform backscattering profile $R_s(k_o)$, which we used to calculate the normalized backscattering signal of the scatterer at z_i, $I_{norm}(k_o, z_i)$, as

$$I_{norm}(k_o, z_i) = \frac{I(k_o, z_i)}{|PSF(k_o, 0)|} \propto \sqrt{R_s(k_o)} \ . \tag{6}$$

The backscattering spectrum of the cell, $R_s(k_o)$, proportional to ${I_{norm}}^2(k_o, z_i)$, was then calculated. The background spectrum of each cell was extracted from the adjacent 80 A-scans without cells at the same depth for noise subtraction. The spectrum after noise subtraction was then converted from wavenumber to wavelength and normalized to its mean (Fig.13(c)). By tracking individual cells in repeated B-scans or volumes, the averaged spectrum of each cell with much higher SNR was obtained (Fig.13(d)).

3.3.6 Mie theory Library and Fit

To estimate the backscattering spectra of polystyrene microspheres, we applied Mie theory to calculate the theoretical backscatter spectrum as a function of size for microspheres of a range of diameters. Although Mie theory assumes plane wave illumination, Xu et al. has demonstrated that, for an OCT system with a weakly-focused beam, the shape of the backscattering spectrum of a cell is not significantly affected by the NA of the sample beam, the axial location of the cell within the depth of focus, or the lateral location of the cell centered at within the beam width [105]. Thus, Mie theory is a reasonable model for this study. A look-up table of Mie spectra was generated using MiePlot [106] with the following parameters: refractive index of polystyrene n_{part} = 1.572, refractive index of aqueous humor n_{med} = 1.336 [107], and the particle diameter d = 9-11 μm, in increments of 0.01 μm. We fit the normalized backscattering spectrum of each microsphere with the Mie spectra library we generated, and the best fit was determined

by minimization of the mean squared error (MSE) between the Mie spectrum and our measured backscattering spectrum. The characteristic size of each microsphere was then directly extracted from the corresponding size of the best Mie spectra fit.

We also used Mie theory to correlate the backscatter spectra of single cells to their characteristic sizes. Previous studies have shown that, for WBCs, light scattering from the cell in the backward direction is mostly due to scattering from the nucleus [108], and the characteristic size extracted from fitting the oscillatory components in the spectrum is highly correlated to the size of the nucleus [109]. A look-up table of Mie spectra for multiple cell nuclei sizes was also generated using MiePlot [106] for comparison against our experimental spectroscopic data. We used the following parameters based on previous studies of refractive index profiles of WBCs using refractive index tomography [110, 111]: the particle diameter d = 1-12 μm in increments of 0.05 μm; particle/nucleus refractive index n_{part} =1.39-1.41, in increments of 0.005; medium/cytoplasm refractive index n_{med} =1.35-1.37, in increments of 0.005; and wavelength λ = 998-1103 nm.

3.3.7 Red Blood Cell Backscattering Spectrum Modeling

Because RBCs lack cell nuclei and are better modeled as biconcave discs rather than spheres, Mie theory may not accurately model RBC cell size. Moreover, backscattering spectra of a single RBC will be dependent on the orientation of the cell in relation to the incident beam. Prior studies have investigated the backscattering spectra

of a single RBC using first-order Born approximations [112, 113], T-matrix [114], and finite difference time domain analysis [115]. Here, we applied a body of revolution spectral integral method (BoR-SIM) [116] to simulate the theoretical spectrum of an RBC model at different orientations. For this analysis, we used an expression for the shape of an RBC described by Fung, et al. [117] and Yurkin, et al. [118]:

$$T(x) = 0.65d\sqrt{1-x^2}(0.1583 + 1.5262x^2 - 0.8579x^4)$$

Here, T is the thickness of the RBC along the axis of symmetry, x is a relative radial cylindrical coordinate [$x = 2\rho/d(-1 \leq x \leq 1)$], ρ is a radial cylindrical coordinate, and d is the diameter of the RBC. The diameter d we used in our simulation was 7.8 μm [119]. The cross section and 3D shape of our idealized RBC model is shown in Fig. 4. We assumed the refractive index of RBC to be 1.39. We ignored the effect of absorption coefficient and refractive index differences between oxygenated and deoxygenated RBCs in our simulation, as for a single RBC, these spectral signatures due to absorption are significantly weaker than those oscillatory spectral features due to its geometry and orientation [112].

Assuming a plane wave incident field, we varied the angle of the incident field relative to the RBC to model the RBC at different orientations and the corresponding resulting backscattering spectra. Because the RBC model is radially symmetric along z-axis, varying the angle of incident field, α, along one cross section plane, xz, was enough to cover all the possible incident field conditions (Fig. 4(b)). Additionally, we modeled

the RBC backscattering cross-section spectrum at two orthogonal linear polarizations, horizontal polarization θ and vertical polarization Φ, with the incident angles of field, α, with respect to the RBC varying from 0° to 90° and a step size of 2.5°. Using a Mie theory fit, we compared the simulation results to the experimental results. While Mie theory cannot accurately model RBC cell size, as we also show later in Section 3.4.2 and 3.4.4, both the simulated and experimental results showed that the extracted characteristic size distribution difference was sufficient to differentiate populations of RBCs from all subtypes of WBCs.

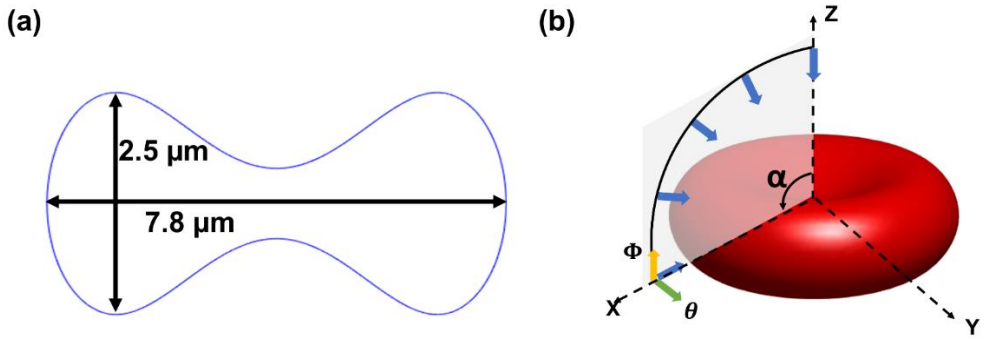

Figure 14: The (a) cross section and (b) 3D rendered shape of the RBC model. In (b), illustrative angles are shown of the incident field α (blue arrows), at two orthogonal linear polarizations, horizontal θ (green arrow) and vertical Φ (yellow arrow).

3.4 Results

3.4.1 Phantom Results

A representative OCT B-scan image of 10 μm polystyrene microspheres injected into the AC of a freshly enucleated porcine eye is shown in Fig. 15(a). Representative spectroscopic data of a single microsphere and its best Mie spectral fit are shown in Fig

15(b). A histogram of microsphere sizes (N = 121), extracted from the corresponding best Mie fit, is shown in Fig. 15(c). The mean size was found to be 10.01 μm with a standard deviation of 0.029 μm. These values were within the manufacturer's specification for these microspheres of 10.00 μm ± 0.08 μm.

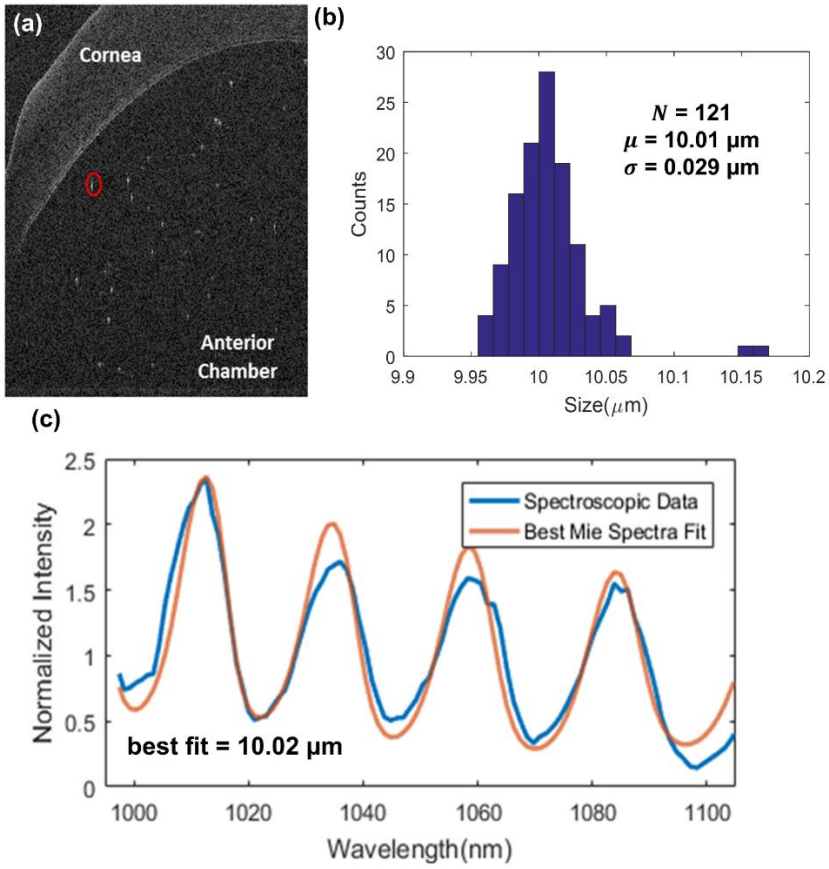

Figure 15: Results of *ex vivo* polystyrene microspheres experiment. (a) A single B-scan of 10um polystyrene microspheres injected into the AC of a porcine eye; (b) Five averaged STFT spectra obtained from a single microsphere (red circle in (a)) and its best Mie spectra fit. The best fit Mie spectra was for a 10.02μm diameter sphere; (c) Extracted microsphere thickness histogram from 121 microsphere measurements.

3.4.2 *In Vitro* Cell Results

Isolated RBCs (N = 634), granulocytes (N = 769), lymphocytes (N = 737) and monocytes (N = 638) in separate glass cuvettes were imaged. Individual cells were localized and tracked in either B-scan or volumetric imaging mode based on the cell moving speed evaluation criteria in Section 3.3.3, and the characteristic size of each tracked cell based on the best Mie spectra fit was found. Histogram plots of characteristic sizes of each cell type are shown in Fig. 16(a,b,g,h), along with their means and standard deviations. Histogram plots of characteristic sizes of each cell type are shown in Fig. 6(a,b,g,h), along with their means and standard deviations. For RBC, the characteristic sizes (Fig. 6a) shows a bimodal distribution instead of a normal distribution; Therefore, we calculated the probability density function (PDF) of the RBC size distribution using kernel density estimation, and fitted the PDF with the following bimodal Gaussian distribution function,

$$f(x) = a_1 e^{-\frac{(x-\mu_1)^2}{2\sigma_1^2}} + a_2 e^{-\frac{(x-\mu_2)^2}{2\sigma_2^2}} \quad (7)$$

The means and standard deviations of the best-fit bimodal distribution were found to be, μ_1=1.94 μm, μ_2=5.41 μm, σ_1=0.85 μm, and σ_2=0.98 μm. In Fig. 17(c,d,i,j), we show the extracted backscattering spectra, best-fit Mie spectra, and extracted characteristic size of a representative single cell from each cell type. In Fig. 17e,f,k,l), we show the B-scan images containing the cells depicted in Fig. 17(c,d,i,j), with all cells in the B-scan color-coded to represent the best-fit characteristic sizes of each individual

cells within the image. Note that cells within the B-scan without color coding (shown in gray) correspond to cells that did not remain in the FOV for at least 20 repeated B-scans or volumes.

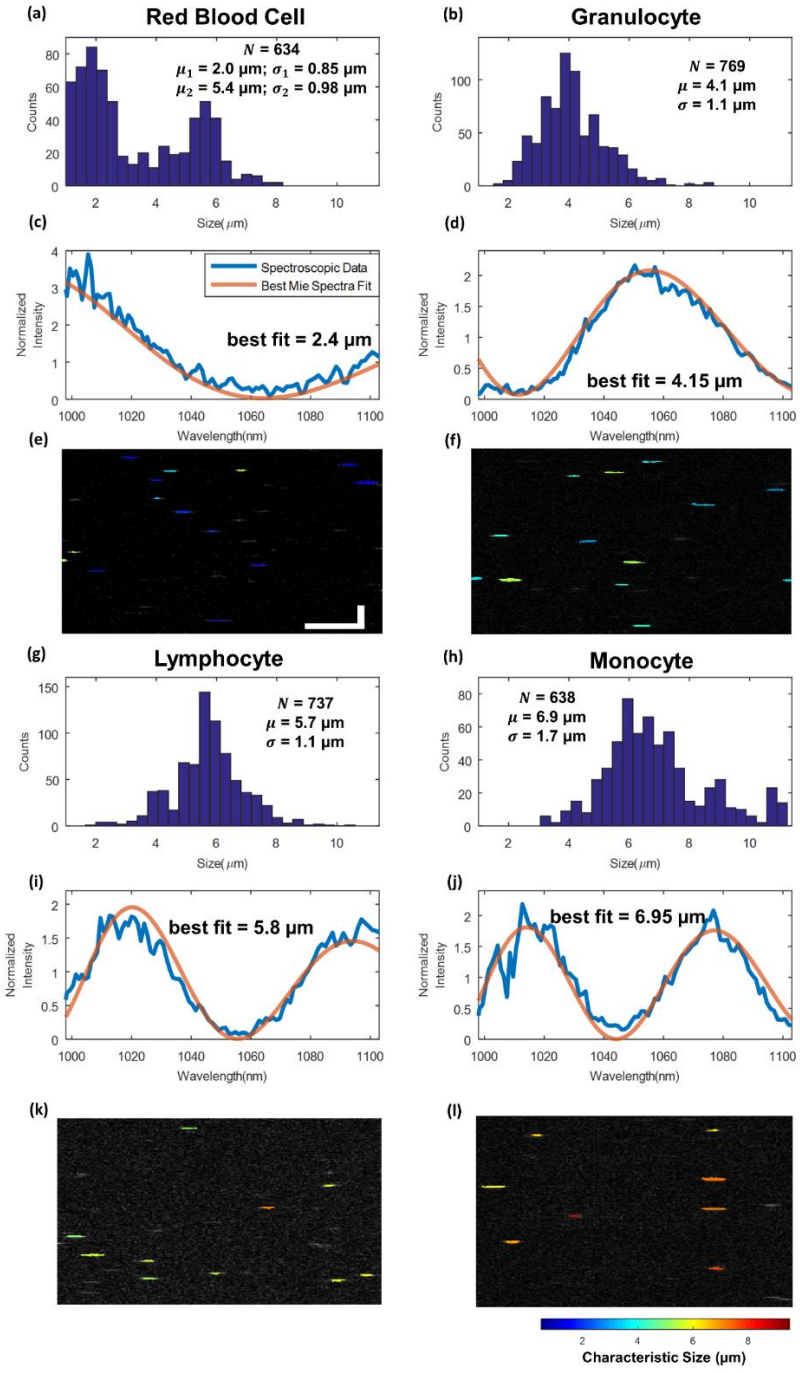

Figure 16: Results of *in vitro* studies of each cell type. (a,b,g,h) Histogram plots of characteristic cell sizes extracted from the best Mie spectra fit with mean and standard deviation; (c,d,i,j) Representative spectrum of a single cell from each blood cell type, and its best Mie spectra fit; (e,f,k,l) OCT B-scan image of each cell sample

with color-coded overlay of the characteristic best-fit sizes of individual cells observed (see color bar for best-fit cell size scale). Distance scale bar (white): 100μm.

A boxplot representation of the characteristic size distributions for each cell type is shown in Fig. 17. The means of the size distributions were all found to be significantly different between each pairs of cell types using one-way ANOVA and post hoc tests with the Bonferroni correction ($p < 0.0001/6 = 1.66*10^{-5}$), which indicates that characteristic size distribution could be used to differentiate between populations of RBCs and subtypes of WBCs. For patients with a dominant cell type present in the AC, the cell type can potentially be identified based on the extracted characteristic size distribution.

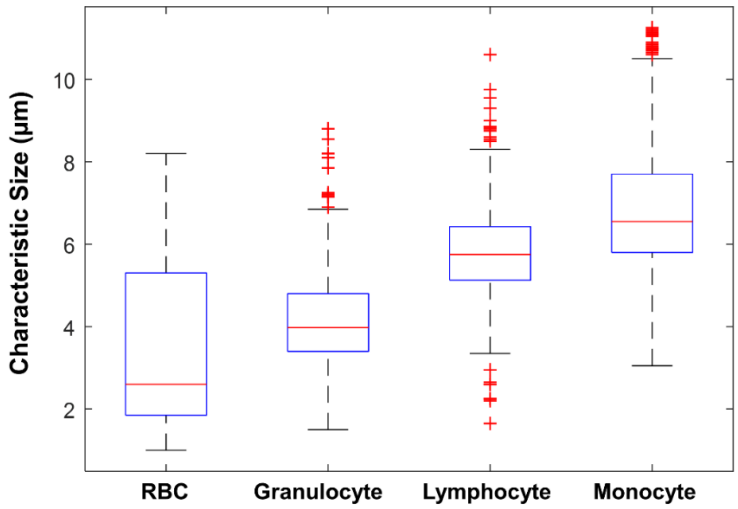

Figure 17: Boxplot of the characteristic size distributions of RBCs, granulocytes, lymphocytes and monocytes observed in the *in vitro* cell study. The box plot represents the range of characteristic sizes, with the red line corresponding to the median size of each cell type, the blue box corresponding to the interquartile distribution, the whiskers corresponding to the sizes within 1.5 times the

interquartile range and the red plus signs representing outliers that are located outside the whiskers.

The size distribution of each type of cell was found to overlap with the size distributions of other types of cells, which means it will still be challenging to differentiate cell type at the single-cell level. To further quantify the overlap among the size distributions, the support vector machine (SVM) classifier with a Gaussian kernel and 10-fold cross validation was applied, and the receiver operating characteristic (ROC) curves between the characteristic sizes of each pairs of cell types were plotted in Fig.8, along with the corresponding areas under the curve (AUC).

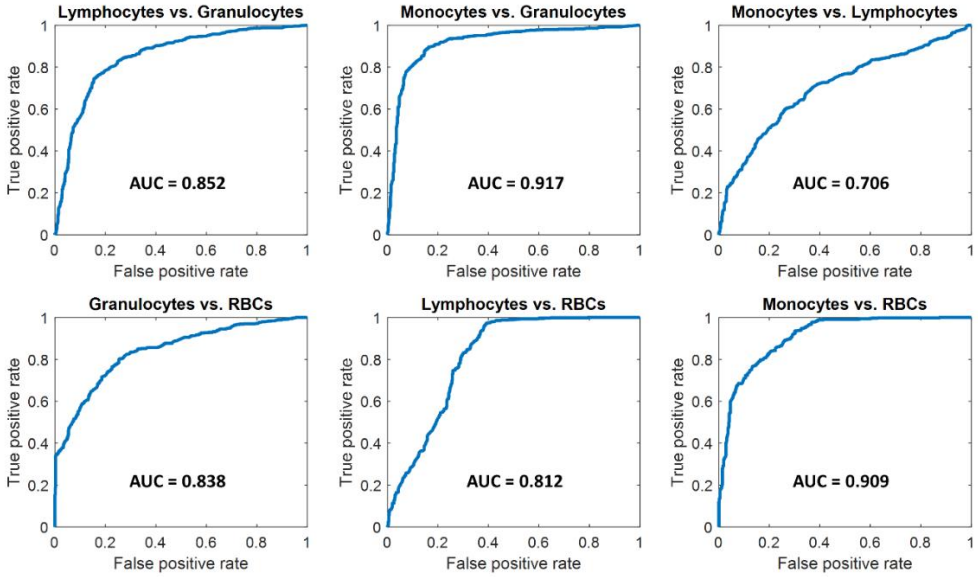

Figure 18: The ROC curves between the characteristic sizes of each pairs of cell types, along with the corresponding AUC values.

3.4.3 *Ex vivo* Cell Results

We also investigated granulocytes injected into the ACs of freshly enucleated porcine eyes to mimic the *in vivo* environment. A representative OCT volume render

with granulocytes suspended in the AC of a porcine eye is shown in Fig.19(a). The characteristic size distributions of RBCs (N=332), granulocytes (N = 246), lymphocytes (N=268) and monocytes (N=219) acquired from the porcine eye studies are shown in Fig.19(b,c,f,g).

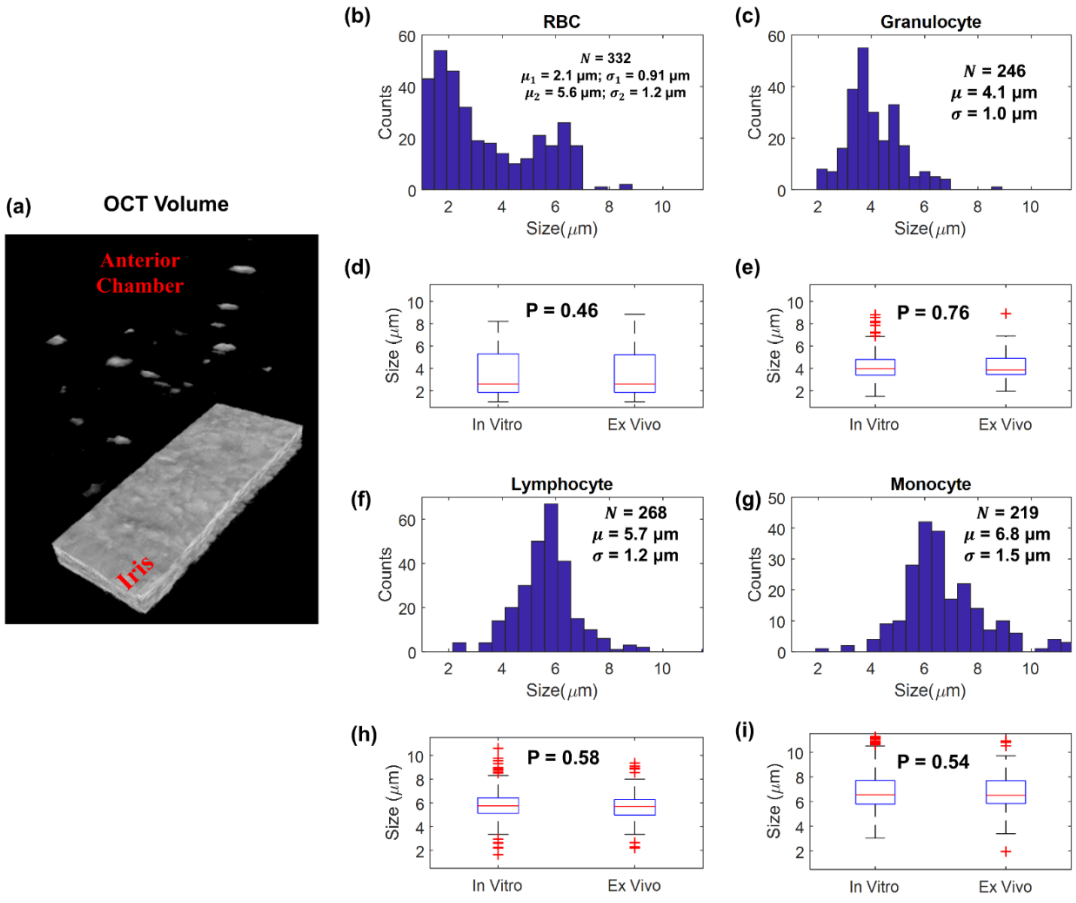

Figure 19: Results of *ex vivo* porcine eye studies of each cell type. (a) Representative OCT volume of granulocytes suspended in the AC of a porcine eye; (b,c,f,g) Histogram plots of characteristic cell sizes extracted from the best Mie spectra fit with means and standard deviations; (d,e,h,i) Boxplot of the characteristic size distributions of all four types of cells *in vitro* and *ex vivo*, and the corresponding p-values calculated using the Wilcoxon rank sum test.

The mean characteristic cell sizes of the *ex vivo* porcine eye studies were very similar to the sizes observed in the *in vitro* studies for all four types of cells (RBC: 2.0 & 5.4 μm vs. 2.1 & 5.6 μm, granulocyte: 4.1 μm vs. 4.1 μm, lymphocyte: 5.7 μm vs. 5.7 μm, and monocyte: 6.9 μm vs. 6.8 μm). No statistically significant difference in the size distributions of all four types of cells between the *in vitro* and the *ex vivo* porcine eyes was found (Fig.19(d,e,h,i)) using the Wilcoxon rank sum test (RBC: $p = 0.46$, granulocyte: $p = 0.76$, lymphocyte: $p = 0.58$, and monocyte: $p = 0.54$).

3.4.4 Red Blood Cell Backscattering Spectrum

The backscattering cross-section, with units of μm^2 or dB μm^2, indicates the scattering property of an object to reflect incident field energy back to the direction of incident field. The BOR-SIM theoretical backscattering spectra of a single RBC at four representative orientations with respect to incident light are shown in Fig. 20.

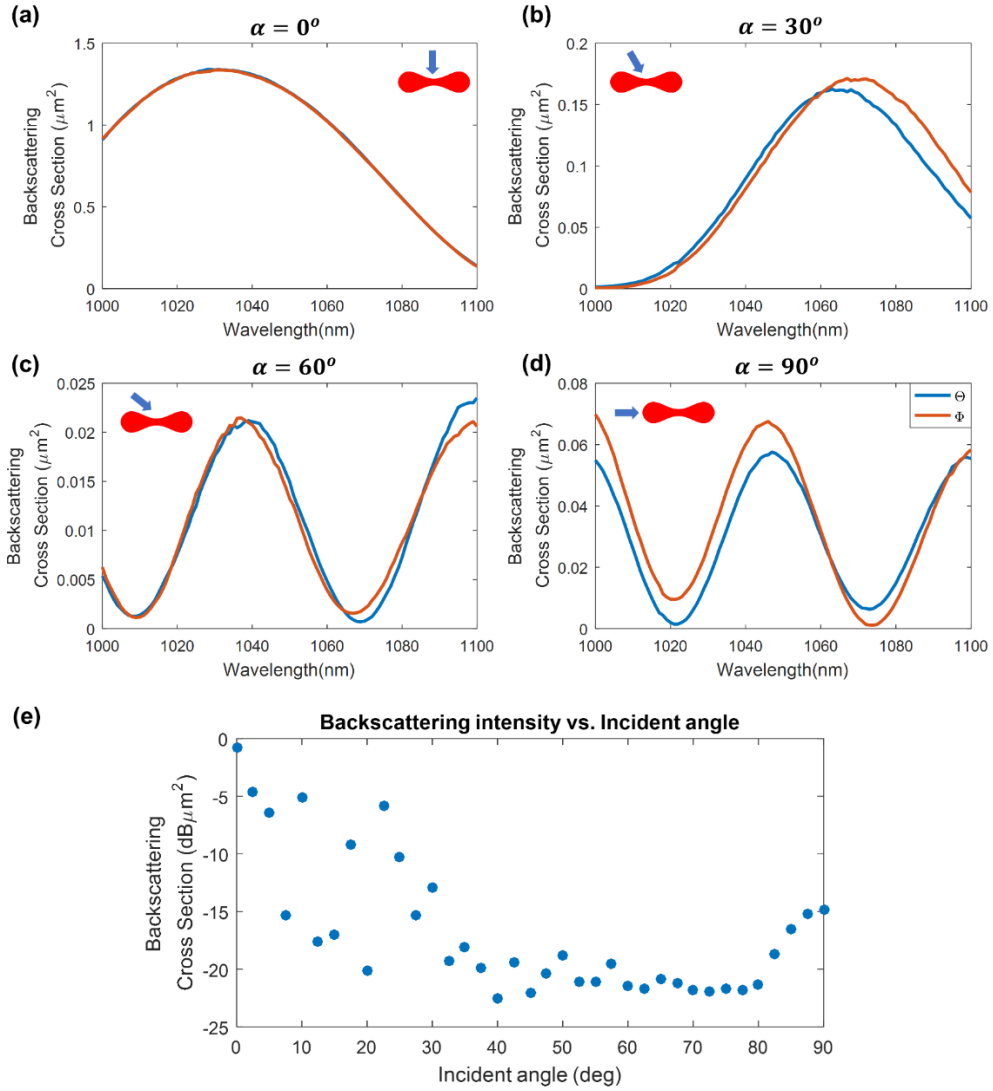

Figure 20: The backscattering spectra of an RBC with different incident angles of light at two orthogonal linear polarizations. (a) 0°, perpendicular to the long axis of the RBC; (b) 30°; (c) 60°; (d) 90°, parallel to the long axis of the RBC. (e) The total backscattering cross-sectional intensity across the entire spectrum as a function of incident angle from 0° to 90° with a step size of 2.5°.

As expected, the frequency of oscillation features in the theoretical spectrum increases as the incident angle of field with respect to the RBC increases. The oscillation frequency of the spectrum is related to the axial optical path length of the scatterer. For

an RBC, when the incident angle of field increases, the axial cross-section length increases from the short axis to the long axis, such that the spectrum has a higher oscillation frequency feature. The spectra at two orthogonal polarizations were completely overlapped when the incident angle of field was 0° (Fig. 20(a)), since the RBC is circular symmetric in the plane of the long axis. At other incident angles, the differences between spectra for the two orthogonal polarizations were minimal (Fig. 20(b)-(d)), and the different polarization spectra had minimal difference in frequency of oscillation features at each angle. Therefore, for simplicity we only used the theoretical spectra with horizontal polarization (θ) for the further analysis below. More importantly, the minimal spectra difference supports that the polarization state of incident light on the sample need not be precisely controlled. Furthermore, the total backscattering cross-sectional intensity of a scatter can be obtained by integrating the intensity at each wavelength, and should be directly correlated to the intensity of a scatterer within an OCT A-scan. For RBCs, we applied this concept and calculated the backscattering cross-sectional intensity across the entire spectrum at each incident angle (0° to 90°) and plotted intensity as a function of wavelength (Fig. 20(e)). The magnitude of the backscatter cross section clearly decreases with increasing incident field angle, as expected from the profile of the RBC cross section viewed as a function of obliquity.

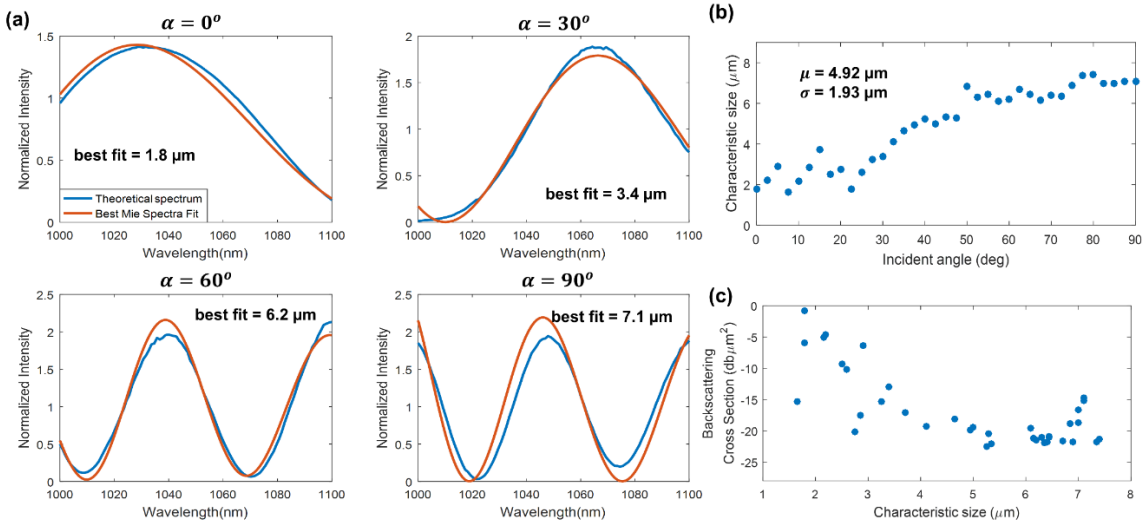

Figure 21: Simulation results of RBC backscattering spectra vs. Mie theory. (a) Normalized backscattering spectra and their best Mie fits at difference incident angles of light; (b) Characteristic sizes extracted from the best Mie fit as a function of incident angles of light ($0° - 90°$ with a step size of $2.5°$); (c) Backscattering cross-section as a function of characteristic size at all the incident angles ($0° - 90°$ with a step size of $2.5°$)

We compared the BoR-SIM theoretical backscattering spectra and our Mie theory library (which assumes spherical scatterers) to extract characteristic sizes from model RBCs as a function of the incident light angle. The best-fit Mie spectra and the corresponding sizes at representative incident angles of light are shown in Fig. 21(a). The extracted sizes from best-fit Mie spectra are shown in Fig. 21(b) as a function of incident angles from 0° to 90°. When the oscillation frequency of a backscattering spectrum increased, the characteristic size extracted from the best-fit Mie spectrum also increased. The characteristic size range of our RBC spectra model was 1.5 – 8 μm diameter, which corresponds well to our experiment results, 1- 7.8 μm diameter, shown

in Fig. 16. When the incident angle of light was within the range of 0° to 30°, the extracted characteristic sizes were between 1.5 and 3 μm, which includes the length of the short axis of the RBC model, 2.5 μm. When the incident angle of light was increased to more than 50°,the extracted characteristic sizes rapidly increased to between 6 and 8 μm, which includes the length of the long axis of the RBC model of 7.8 μm. Thus, although the spherical model assumed by Mie theory is not an accurate morphological model for RBCs, the extracted size using Mie theory was found to correlate well to the axial cross-section length of the RBC at different orientations. These theoretical models, in general, agree with our observed experimental characteristic size distributions, which is a bimodal distribution with two means at approximately 2 μm and 5.4 μm diameter, shown in Fig. 16. However, for the theoretical model, the characteristic size averaged over all incident angles was 4.92 μm ± 1.93 μm and was larger than our experimental results of 3.35 μm ± 1.83 μm.

We also plotted the backscattering cross-sectional intensity as a function of characteristic size in Fig. 21(c). As expected, when the RBC had a small characteristic size, indicating that the incident angle of light was small, it had a higher backscattering intensity due to a larger cross-sectional area perpendicular to the incident field.

We compared this simulated result with our experimental results. The averaged peak intensity of individual RBCs in repeated OCT volumes was calculated, and the scatter plot of average intensities of individual RBCs (N = 133) vs. their characteristic

sizes is shown in Fig. 22(a). Representative spectra from two individual RBCs and their best-fit Mie spectra are shown in Fig. 22(b)-(c). We observed a similar, negative correlation between RBC backscattering intensity and its characteristic size: a RBC with a higher backscattering intensity tends to have a smaller characteristic size. This unique negative correlation may provide an additional dimension of data to differentiate RBCs from WBCs. For WBC nuclei, which are more spherical, the backscattering intensity is expected to increase as the size of the cell nucleus increases.

Additionally, we noticed intensities of some individual RBCs were only slightly above the intensity threshold used to locate and track each cell. This threshold value was previously optimized to maximize the number of localized cells while not labeling noise within the OCT B-scan as individual cells. Thus, some cells with intensities below the threshold were likely excluded from the analysis, and those cells were more likely to have larger characteristic sizes, based on our simulation results, as seen in Fig.21(c). This may be the primary cause of the differences between the smaller mean characteristics size of our experimental results, 3.35 μm, and the larger mean characteristic size of our RBC theoretical model, 4.92 μm. Another potential source of error could be the geometry model and the inhomogeneous refractive index distribution of RBC.

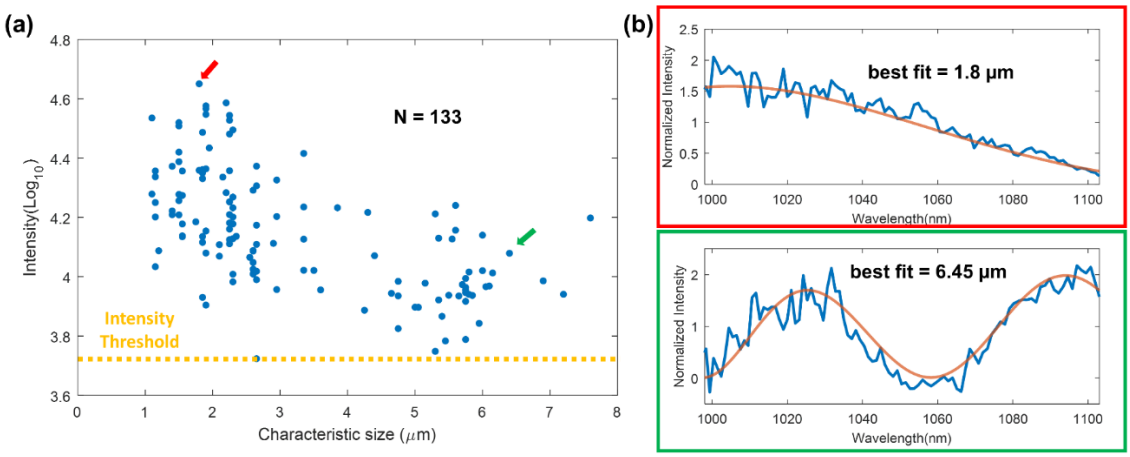

Figure 22: (a) The intensity of individual RBCs in the OCT volume vs. their characteristic sizes. (b-c) Representative spectra from RBCs with small and large characteristic sizes.

Overall, we demonstrated that although Mie theory is not an accurate model for calculating the physical size of RBCs due to their nonsphericity, the extracted size from Mie theory fit was highly correlated to the axial cross-section length of RBC at each incident angle of light, which explains why their characteristic size distribution extracted from Mie theory was sufficient to statistically differentiate populations of RBCs from WBCs.

3.5 Discussion

We have shown that spectroscopic OCT analysis of single blood cells can differentiate populations of RBCs and subtypes of WBCs, including granulocytes, lymphocytes and monocytes. The characteristic size distribution extracted from the Mie theory fit was found to be significantly different among these different types of blood cells. Previous studies have shown that the characteristic sizes extracted from WBCs

using Mie theory are likely to be their nuclear sizes for mononuclear leukocytes such as lymphocytes and monocytes, and sizes of the lobules of the nucleus for polymorphonuclear leukocytes such as neutrophils [109]. There was generally good agreement between our results and the nuclear sizes acquired from previous studies using conventional optical microscopy [120], differential interference contrast microscopy [109], and light-scattering spectroscopy [109]. For the granulocytes, mainly neutrophils, the reported mean characteristic size, 4.1 μm, was consistent with the nuclear lobe sizes reported from other studies, which ranged from 3.0 to 4.4 μm. For lymphocytes, the mean size of 5.7 μm was also within the range of previous reported values, which was from 4.5 μm to 6.4 μm. Three-dimensional refractive index maps of subtypes of WBCs were previously studied using refractive index tomography [110, 111]. However, no quantitative information regarding the nucleus sizes were reported directly in these studies. Moreover, a Mie theory approach here assumes nuclei or nuclei lobes that are spherical, of a uniform refractive index, and that the backscattering signal is dominated by the scattering from the nuclei, all of which oversimplifies the complex morphology of cells. For instance, monocytes tend to have a kidney-bean shaped nucleus while the nuclei of neutrophils have lobes which may not be appropriately modeled as spherical [121]. Additionally, the refractive index we used for our Mie theory library was measured using refractive index tomography at 532nm and 633nm, as there have been no studies at 1000-1100nm wavelength range. However, as

demonstrated in this paper, Mie theory is a sufficient model to statistically differentiate populations of subtypes of WBCs.

In this work, we have developed an algorithm to track single cells in repeated B-scans or volumes. Our scanning protocols were selected based on the moving patterns of *in vitro* and *ex vivo* cell samples, which were heavily affected by the gravity. For future *in vivo* studies, these protocols will likely need be adjusted, because cells in the AC are known to follow a circulating flow pattern due to the natural temperature gradient [102], and living human eye motion artifacts will need to be mitigated. Multiple techniques could be utilized to reduce significant artifacts due to motion during *in vivo* imaging. First, a swept source with a much faster A-scan rate can be used to reduce the acquisition time. For example, with a 1MHz swept source, one acquisition of our repeated B-scan mode (500 A-scans/B-scan, 50 B-scans) would take only 40ms. Another approach could be to use repeated B-scans or volumetric scans with a smaller FOV but a higher effective frame rate. Although fewer cells would be localized in a single acquisition, our cell tracking algorithm would be less likely to be affected in a shorter acquisition time. Multiple measurements could be performed at different locations of the AC to achieve a similar total number of cell measurements. Other real-time eye tracking and motion compensation techniques may also be considered, such as pupil tracking using a 2D fast steering mirror [122] and SLO-based eye tracking [123].

Our porcine eye studies demonstrated that OCT signal attenuation in even deceased corneas did not compromise our spectroscopic analysis methodology. Given that porcine corneas are thicker than human corneas, and that *ex vivo* corneas lack the cellular processes which actively maintain corneal clarity *in vivo*, we believe the porcine corneas were a fair test of robustness with regard to SNR. Finally, we note that as described in the method section 2.1, our illumination power on the sample in both *in vitro* and *ex vivo* studies was 2.2mW, which is well below the optical power safety limit of the newer ANSI standard (Light Hazard Protection for Ophthalmic Instruments - ANSI Z80.36-2016).

The lateral resolution of our system was 20 μm, so that the system had a large enough depth of focus to localize individual cells across the whole AC depth. This resolution is similar to the lateral resolution of conventional, clinical anterior segment OCT systems, which indicate that this proposed spectroscopic technique could potentially be applied directly to widespread clinical OCT systems. However, a higher resolution system may be considered for future *in vivo* imaging to improve the backscattering signal from the cell, but with a tradeoff of the depth of focus. Finding the optimal balance between depth of focus and lateral resolution for our technology is important for our future *in vivo* studies.

In both *in vitro* and *ex vivo* experiments, the cell samples were diluted to a concentration of ~150 cells/mm^3 and minimal cell aggregations were observed. For

patients with inflammatory cellular response in the AC, such as anterior uveitis patients, the number of cells is assessed by the examiner in a slit-lamp microscope evaluation and assigned an integer score from 0 (no cells seen) to 4+ (many cells). The highest clinical grade of 4+ corresponds to ≥50 cells in a lateral FOV of 1 mm *1mm [124]. Given that the average human anterior chamber depth is approximately 3mm [125], the cell concentration of a uveitis patient with a slit-lamp grade of 4+ is thus ≥17 cells/mm^3, which is much smaller than the concentration we used in our *in vitro* and *ex vivo* studies. Moreover, prior studies from Rose-Nussbaumer et al. also showed that the average *in vivo* cell axial size from uveitis subjects were only slightly larger than *in vitro* cell size measurements from OCT images (*in vivo* 6.7–6.8 versus *in vitro* 6.3 μm), which also suggests that aggregated cells are not common in *in vivo* imaging [100].

The methodology demonstrated here could be applied to investigate cell compositions in the vitreous body in several diseases, such as posterior uveitis, using a retinal OCT scanner. Without any required hardware modifications, this proposed spectroscopic technique could potentially be applied as a software upgrade to widespread clinical OCT systems, and combined with other cell information that may further facilitate cell differentiation, such as flow speed, intensity and spatial distribution of cells. Machine learning based approaches could also be implemented to improve the classification.

3.6 Summary

In this work, we developed a spectroscopic OCT analysis method to differentiate between RBCs and subtypes of WBCs, including granulocytes, lymphocytes and monocytes. We located and tracked individual blood cells in repeated OCT B-scans or volumes, and extracted their corresponding backscatter spectra using spectroscopic OCT. We then correlated the spectrum of each cell to its characteristic size by fitting with a Mie theory database. Together, our *in vitro* studies indicated that the extracted size distributions based on the best Mie spectra fit were significantly different between each cell type. To confirm these observations, our pilot *ex vivo* studies with blood cells injected into porcine eyes suggested that spectroscopic OCT can potentially differentiate blood cells in AC *in vivo*. We further studied the backscattering spectrum of RBC at different incident directions of light. We showed that, although Mie theory is not an accurate model for RBCs, the extracted size from Mie theory was highly correlated to the axial cross-section length of RBC at different orientations, sufficient to differentiate RBCs from WBCs. The above described work can potentially provide quantitative diagnostic information of cellular responses in the ocular anterior chambers of patients in the clinic and expand the field's pathophysiologic knowledge about diseases such as anterior uveitis.

4 *In Vivo* Quantitative Analysis of Anterior Chamber Blood Cell Mixture Composition Using Spectroscopic OCT

4.1 Abstract

Anterior uveitis is the most common form of intraocular inflammation, and one of its main signs is the presence of white blood cells (WBCs) in the anterior chamber (AC). Clinically, the true composition of cells can currently only be obtained using AC paracentesis, an invasive procedure to obtain AC fluid requiring needle insertion into the AC. We previously developed a spectroscopic optical coherence tomography (SOCT) analysis method to differentiate between populations of RBCs and subtypes of WBCs, including granulocytes, lymphocytes and monocytes, both *in vitro* and in ACs of excised porcine eyes. We have shown that different types of WBCs have distinct characteristic size distributions, extracted from the backscattered reflectance spectrum of individual cells using Mie theory. Here, we further develop our method to estimate the composition of blood cell mixtures, both *in vitro* and *in vivo*. To do so, we estimate the size distribution of unknown cell mixtures by fitting the distribution observed using SOCT with a weighted combination of reference size distributions of each WBC type calculated using kernel density estimation. We first validated the accuracy of our estimation in an *in vitro* study, by comparing our results for a given WBC sample mixture with the cellular concentrations measured by hemocytometer and SOCT images before mixing. We then conducted a small *in vivo* pilot study which demonstrates

congruence between our method and AC paracentesis in two uveitis subjects. The SOCT based method appears promising to provide quantitative diagnostic information of cellular responses in the ACs of patients with uveitis.

4.2 Introduction

Anterior uveitis, inflammation of the iris and the ciliary body, is the most common form of intraocular inflammation [126], with an estimated 14–17 uveitis cases per 100,000 persons confirmed each year in the USA [126]. In some cases, uveitis can lead to serious complications such as cataract, glaucoma and cystoid macular edema [127], which accounts for 10% of legal blindness in the USA [128]. Despite its importance as a vision threatening disease, the causes of many anterior uveitis cases are unknown [129]. One of the main signs of anterior uveitis is the presence of white blood cells (WBCs) in the anterior chamber (AC). The clinical standard evaluation is grading of these cells by uveitis specialists on a scale of 0 to 4+ using slit-lamp microscope, defined by Standardization of Uveitis Nomenclature (SUN) [130]. One limitation of the slit-lamp evaluation is that subjective qualitative assessment of the condition makes it difficult to judge the longitudinal course of the cellular response. Another major limitation is lack of differentiation between subtypes of WBCs, such as granulocytes, lymphocytes and monocytes. Many human and animal studies have shown that different etiologies of uveitis have different cell composition patterns. For instance, predominantly granulocytic responses may suggest acute and autoimmune inflammations such as

HLA-B27-asscoiated acute uveitis [85, 86] , while a predominant response of mononuclear WBCs, mainly lymphocytes and monocytes, may suggest sarcoidosis [87], Vogt–Koyanagi–Harada [88], or melanin-protein-induced uveitis [89] as examples. Therefore, the composition of AC cells can potentially provide additional diagnostic information regarding the underlying cause of uveitis and hence guide management. Clinically, this information regarding the true composition of cells can currently only be obtained using AC paracentesis which requires invasive needle insertion into the anterior chamber to withdraw fluid with potential complications [91, 131].

Optical coherence tomography (OCT) allows noninvasive, high-resolution cross-sectional imaging of the AC [92], and can be a useful adjunct to provide quantitative diagnostic information regarding cellular responses associated with uveitis. Several groups have previously developed technologies to localize and count cells appearing in the anterior segment OCT (AS-OCT) images in human or animal models [93-97]. However, none of these technologies were able to provide quantitative information regarding the composition of cellular mixtures. Although different types of WBCs have distinct cell sizes or nucleus shapes and sizes, the differences cannot be distinguished directly with contemporary clinical AS-OCT systems because the axial resolution of these systems, typically 5-10μm, is comparable to the size of WBCs. Therefore, individual blood cells appear as indistinguishable hyper-reflective spots in conventional AS-OCT images [100]. Rose-Nussbaumer et al. have previously demonstrated the

possibility to differentiate subtypes of WBCs using the reflectance intensity in OCT images [100]. However, the cell reflectance in the OCT images can possibly be affected by many external factors, such as illumination laser power, optical alignment, and cornea opacities.

To address this shortcoming, in chapter 3, we reported a spectroscopic OCT (SOCT) analysis approach to differentiate subtypes of WBCs, including granulocytes, lymphocytes and monocytes, both *in vitro* and within *ex* vivo porcine eyes [132]. Our approach involved tracking and extracting the backscatter spectrum of isolated single blood cells in repeated OCT B-scans or volumes and correlating the spectral features of single cells to their characteristic sizes using Mie theory fitting. We demonstrated that all three subtypes of WBCs had statistically distinct size distributions. In this work, we further develop this method to estimate the composition of unknown AC cellular mixtures. We have validated the accuracy of our method in both *in vitro* experiments and a preliminary *in vivo* clinical pilot study.

4.3 Methods

4.3.1 *In Vitro* Cell Mixture Study

OCT system design

In vitro imaging was performed utilizing a custom 100-kHz swept-source OCT (SSOCT) system, centered at 1052 nm with a bandwidth of 108 nm (Axsun Technologies; Billerca, MA) with custom imaging optics and OCT engine, as detailed in chapter 3.3.1.

The system had measured axial and lateral resolutions of ~8.8 μm and ~20 μm respectively, and a maximum axial imaging range of 7.4 mm. The measured sensitivity and -6-dB fall off of the system was 103 dB and 4.39 mm with 2.2-mW illumination power on the sample.

In Vitro Cell Mixture Preparation

Cryopreserved granulocytes and lymphocytes from healthy donors (ZenBio Inc.; Research Triangle Park, NC) were obtained; these types were chosen as they are the two predominant WBC types. The detailed procedure we used to obtain a cell suspension in a glass cuvette for *in vitro* imaging was detailed in chapter 3.3.2 . To summarize, cryopreserved WBC samples were rapidly thawed in 37°C water bath and re-suspended in PBS solutions containing 0.1% bovine serum albumin after the cryoprotectant was removed.

We then created a sample mixture of WBCs consisting of granulocytes and lymphocytes. Before mixing the two cell-type samples, two independent approaches were used to determine the true concentrations of the samples. The concentration of each sample was first determined by adding 25μL of cell suspension between cover glass and a hemocytometer (Thermo Fisher Scientific; Waltham, MA), and counting the total number of cells using a 10x microscope objective. As a second, complementary method, OCT was used to separately determine the concentration of each granulocyte or lymphocyte sample. Single B-scans with 500 A-scans/B-scan and the same field of view

(FOV) of 2 mm were acquired at 20 different locations for each sample, and the previously developed cell localization algorithm [132] was applied to count the total number of cells in each scanned dataset. Known volumes of the two component cell samples were then well mixed, and the cell mixture was placed in a glass cuvette for SOCT imaging.

Data Acquisition

Due to the weak backscattering signal from single blood cells, repeated measurements from the same cell were required in order to obtain the spectrum of an individual cell with sufficient SNR for signal processing. We previously developed single cell localization and tracking algorithms for both repeated B-scan and volumetric OCT imaging [132]. In this study, only the repeated B-scan mode was used given the shortened time constraints that would be required for later *in vivo*/clinical imaging experiments. We placed the sample on a manual translation stage (Thorlabs,inc; Newton, NJ) aligned with the sample such that the dominant cell movement was in the same direction as the fast scanning axis, and 200 repeated B-scans with 500 A-scans/B-scan and a field-of-view (FOV) of 2 mm were acquired at 6 different locations of the cell mixture.

Single Cell Tracking and Spectroscopic Analysis

The methods to track and extract the backscattering spectrum of isolated single blood cells and correlate the spectral features of single cells to their characteristic sizes

were detailed in chapter 3.3.4 and 3.3.5. To summarize, we located individual cells in consecutive B-scans by intensity thresholding and labeling connected components. We used the A-scan at the center of every labelled cell for the following spectroscopic analysis. Between any two adjacent B-scans, if a cell located in the second B-scan was within a small region around a cell in the previous B-scan, these two cell images were recorded as arising from the same cell. When the peak cell intensity fell below a defined threshold value, the cell was recorded as having exited the B-scan. Due to the low backscattering signal from single cells, only cells staying in same FOV for at least 15 repeated B-scans were used for the following spectroscopic analysis. We extracted the backscatter spectrum of each cell from its center A-scan using the short-time Fourier transform (STFT). The STFT here used a Hamming window with a spectral bandwidth of 23.7 cm^{-1}, corresponding to an axial resolution of ~340 μm for each window, and the window was shifted across the acquired interferogram a total of 100 times with a step size of 9.2 cm^{-1}. We then normalized the STFT backscatter spectrum by dividing by the known laser power spectrum. After that, we obtained the background spectrum of each cell from the adjacent A-scans without cells at the same depth and performed noise subtraction. Finally, we used Mie theory to correlate the backscatter spectra of single cells to their characteristic sizes (which are likely the size of the nucleus [109]).

Estimation of Cell Mixture Composition

We have previously shown that all three subtypes of WBCs, granulocytes, lymphocytes and monocytes, have distinct characteristic size distributions in chapter 3.4.2. In this study, we further verified our results on more cell samples from different cryopreserved healthy donor cells and used size distributions acquired from these samples as the reference size distributions for each subtype of WBCs (Fig. 2). We calculated the probability density functions (PDFs) of size distributions using kernel density estimation with a Gaussian kernel function, and estimated the cell composition by minimizing the mean square error (MSE) between the PDF of our mixture sample (PDF_{mix}) and a weighted combination of the two component reference PDFs, PDF_{gran} and PDF_{lympho},

$$MSE = \frac{1}{s_{max} - s_{min}} \int_{s_{min}}^{s_{max}} \left(\mathrm{PDF}_{mix}(\mathrm{s}) - (\mathrm{P}_{gran} * PDF_{gran}(\mathrm{s}) + P_{lympho} * PDF_{lympho}(\mathrm{s}))\right)^2 ds \quad (8)$$

where s is the characteristic size, s_{min} and s_{max} are the minimum and maximum characteristic sizes in the distribution, P_{gran} and P_{lympho} are the concentration percentages of granulocytes and lymphocytes in the cell mixture, and $P_{gran} + P_{lympho} = 100\%$.

4.3.2 *In Vivo* Pilot Study of Uveitis Patients

OCT System for *In Vivo* Pilot Study

To facilitate *in vivo* imaging, a custom high-speed SSOCT system was built for the *in vivo* pilot study (Fig. 23) at the Duke Eye Center. The system employed a 200-kHz

swept-wavelength laser (Axsun Technologies; Billerca, MA), centered at 1050 nm with a sweep range of 100 nm. The OCT system utilized a transmissive Mach-Zehnder interferometer topology and the interferometric signal was detected by a balanced photoreceiver (Insight Photonic Solutions, Inc.; Lafayette, CO) with 400-MHz electronic bandwidth and digitized at 800 MS/s (AlazarTech Inc.; Pointe-Claire, QC, Canada). The axial imaging range of the system was 7.4 mm in air. The lateral resolution of the system was designed for 12.8 μm FWHM and 840 μm depth of focus in air. To image throughout the anterior chamber, the system incorporates a focusing module in the sample arm (Fig. 1) to allow for the adjustment of the focal plane axially. The module consisted of two achromatic lenses configured in a 1:1 4F telescope configuration where the first lens was located on a motorized translation stage (National Aperture, Inc.; Salem, NH). The functionality of this module is detailed in the following section.

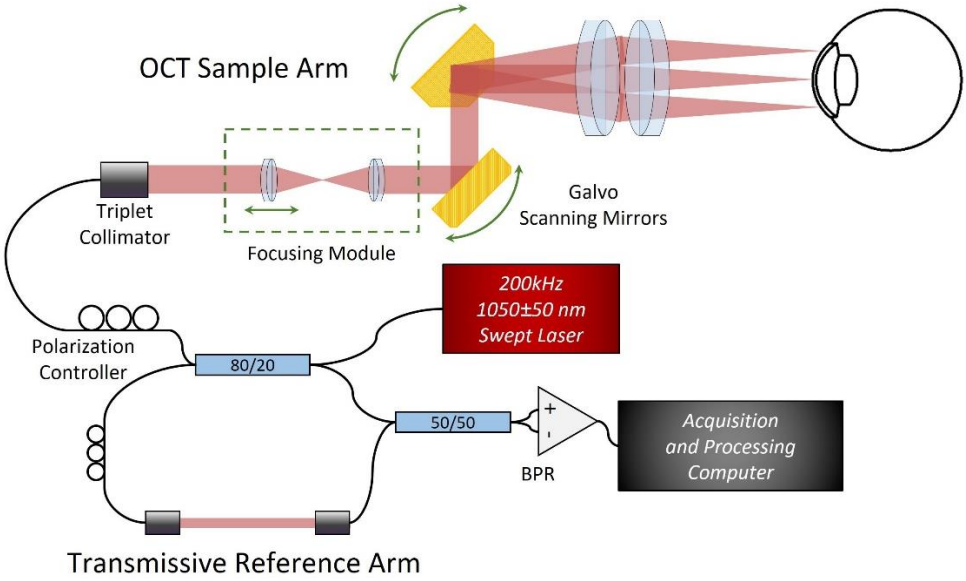

Figure 23: Schematic diagram of the custom 200kHz SS-OCT system for in vivo study with a dynamic focusing module to adjust the focal plane axially BPR: balanced photoreceiver.

***In Vivo* Imaging**

This pilot study was approved by the Duke University Medical Center Institutional Review Board, and adhered to the Health Insurance Portability and Accountability Act and all tenets of the Declaration of Helsinki. Patients with clinically active anterior uveitis of at least 2+ on slit lamp microscopy performed by a uveitis specialist on the day of imaging were enrolled after obtaining written informed consent. The optical power incident on the cornea at 1050 nm was measured at or below 4.1 mW before each imaging session, which is under the maximum permissible exposure determined by American National Standards Institute (ANSI) safety standards (ANSI Z80.36-2016).

The primary difference between all the prior *in vitro/ex vivo* experiments and the *in vivo* imaging was the effect of patient motion during each measurement, as our approach requires multiple OCT B-scans or volumes to obtain the averaged cell spectrum with sufficient SNR for spectroscopic analysis. Therefore, it was important to adjust the imaging scan parameters for *in vivo* imaging at the beginning of the study, with the goal of keeping each single cell within the FOV in consecutive scans while at the same time maximizing the FOV to capture more cells, so that the total imaging time is optimized A total of 7 uveitis patients were imaged during this optimization stage.

We quickly identified that our prior scan protocol based on repeated volumes with the utilized acquisition rate was not ideal for *in vivo* imaging at this point, as >10 repeated OCT volumes combined with a reasonable number of A-scans/B-scan and B-scans/volume requires at least several seconds of imaging, and motion artifacts significantly compromised the cell tracking algorithm. Through imaging initial subjects, we also noticed that cells were not uniformly distributed in each subject's AC, so it was important to identify the regions with more cell appearances at the beginning of the imaging session. Therefore, we designed the following imaging protocol for our study.

Each imaging session started with wide-field volumetric imaging to cover the FOV of nearly the whole AC to study the blood cell distribution in the AC. Once the regions with dense distributions of cells were identified on the real-time OCT volumetric images, we translated the slit-lamp base and the focusing module in the sample arm to

adjust the axial focal plane and lateral position of imaging to these regions. Then, a scanning protocol of 800 A-scans/B-scan, 15 repeated B-scans at 10 different positions along the slow scanning axis (150 B-scans in total), and a FOV of 2 mm by 1 mm, was used. For each subject, we repeated this protocol for 4-5 times to ensure that enough cells were available for measurement.

After imaging parameter optimization, two uveitis subjects were enrolled and imaged in the pilot study. The true compositions of the AC cells were obtained from paracentesis of the subject's AC fluid (the following section "AC fluid cell analysis") and compared to our estimation results.

***In Vivo* Data Processing**

The methods to track and extract the spectrum of single cells was similar to the *in vitro* study above and the previous paper [132], except the minimum number of B-scans (averages) for analysis was reduced from 15 to 6 to ensure that cells stayed within the FOV. Similar to the method in 2.1.5, the spectroscopic OCT based cell composition of each clinical subject was estimated by minimizing the MSE between the PDF of our *in vivo* size distribution (PDF_{sub}) and a weighted combination of all three component reference PDFs, PDF_{gran}(granulocyte), PDF_{lympho}(lymphocyte) and PDF_{mono}(monocyte).

$$MSE = \frac{1}{s_{max}-s_{min}} \int_{s_{min}}^{s_{max}} \left(\mathrm{PDF}_{mix}(\mathrm{s}) - (\mathrm{P}_{gran} * PDF_{gran}(\mathrm{s}) + P_{lympho} * PDF_{lympho}(\mathrm{s}) + + P_{mono} * PDF_{mono}(\mathrm{s}))\right)^2 ds \quad (9)$$

where s is the characteristic size, s_{min} and s_{max} are the minimum and maximum characteristic sizes in the distribution, P_{gran}, P_{lympho} and P_{mono} are the concentration

percentages of granulocytes and lymphocytes in the cell mixture, and $P_{gran} + P_{lympho} + P_{mono} = 100\%$. Here, $P_{lympho}+P_{mono}$ also corresponds to the concentration percentage of mononuclear WBCs. We then compared the estimation results PDF_{gran} and PDF_{lympho} with two reference methods using one-sample t-test.

AC Fluid Cell Analysis

The AC fluid of the first enrolled human subject was sent to a clinical pathology lab and stained using a modified Papanicolaou stain. The slide was then read by a clinical research scientist, and the number of granulocytes, lymphocytes and monocytes were counted based on the nucleus shape and size of the cell.

The AC fluid of the second subject was sent to a research lab, where the sample was simultaneously immunostained for CD45, CD11b, CD11c, CD3, CD4, CD14, CD15, CD16, HLA-DR, and Live/Dead. Data were acquired on a BD Fortessa SORP and analyzed to enumerate live lymphocytes, monocytes and granulocytes using FlowJo software (TreeStar Inc., Ashland, OR).

4.4 Results

4.4.1 Reference Size Distributions of Subtypes of WBCs

In chapter 3, we demonstrated that granulocytes, lymphocytes and monocytes have distinct characteristic size distributions. Here we imaged additional cell samples from different cryopreserved healthy donor cells to further validate our observations, and we used size distributions acquired from these cells as the reference size

distributions for each subtype of WBCs. Histogram plots of characteristic sizes obtained from approximately two thousand cells of each cell type are shown in Fig. 24, along with their means and standard deviations. The means and standard deviations here are similar to our previously reported values (granulocyte: 4.1 μm vs. 4.1 μm; lymphocyte: 5.7 μm vs. 5.7 μm; monocyte: 6.8 μm vs. 6.7 μm). These three reference size distributions were used to estimate the mixture cell composition in the following sections.

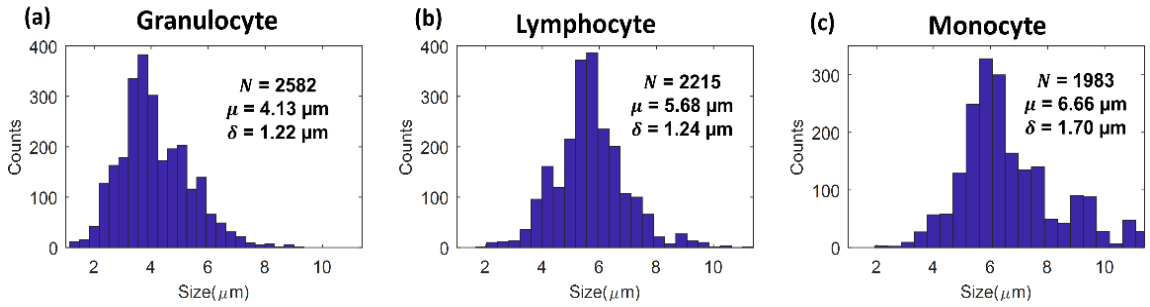

Figure 24 : Histogram plots of characteristic cell sizes of (a)granulocyte (b)lymphocyte and (c)monocyte extracted from the best Mie spectra fit.

4.4.2 *In Vitro* Cell Mixture Results

Repeated B-scans were taken at 6 different locations for the cell mixture sample. Individual cells were localized and tracked, and the corresponding characteristic size of each tracked cell based on the best Mie spectra fit were extracted from the averaged spectrum. A representative B-scan of the cell mixture sample with color-coded characteristic sizes of each individual cells is shown in Fig. 25(a). Cells without color coding correspond to cells that did not remain in the FOV for at least 15 repeated B-scans. The histogram plot of characteristic sizes of all the tracked cells (N=253) at this location is shown in Fig. 25(b), along with their mean and standard deviation. The

extracted backscattering spectrum, best-fit Mie spectrum, and extracted characteristic sizes of two individual cells in the representative B-scan are shown in Fig. 25(c-d). The composition of the cell mixture at this FOV was found to be 62.0% lymphocytes and 38.0% granulocytes by fitting the characteristic size PDF with a weighted combination of two reference PDFs (Fig. 25(e)). The cell composition estimation results at all 6 locations using our spectroscopic OCT method are shown in Table 4, and the averaged lymphocyte and granulocyte proportions across all 6 locations were found to be 61.5% and 39.5%, with a standard deviation of 2.1%. We then compared the estimation results with the results obtained from the component sample counts using the hemocytometer and OCT prior to mixing. Overall, the estimated results using our spectroscopic OCT method agreed with the results from the two reference methods, with percentage deviations of only 0.8% (OCT reference: 60.7% lymphocyte and 39.3% granulocyte) and 0.6% (hemocytometer: 62.1% lymphocyte and 37.9% granulocyte). One-sample t-tests were performed between our estimation results and the two reference method results, and no statistically significant difference was found between the estimation results of our spectroscopic OCT method and the two reference methods (p=0.35 for OCT reference and p=0.48 for hemocytometer). Moreover, the measured cell composition from OCT images before mixing agreed with the results from the hemocytometer counts with a deviation of only 1.4%, indicating that our single cell localization algorithm was capable of locating and tracking most of the cells.

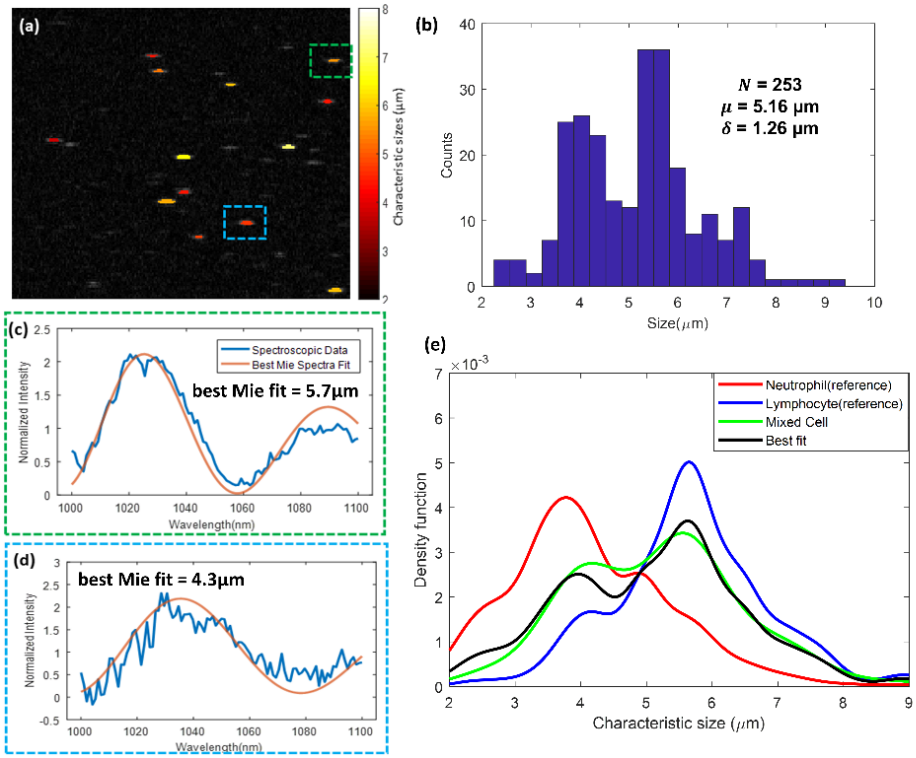

Figure 25: Results of an in vitro mixture cell study. (a) Overlay of characteristic sizes of individual cells with an OCT B-scan image of a cell mixture sample; (b) Histogram plot of characteristic cell sizes extracted from the best Mie spectra fit with mean and standard deviation; (c-d) Representative spectra of two single cells and their best Mie spectra fit; (e) the best fit (black) of characteristic size PDF of this mixture sample (green) with a weighted combination of reference size PDFs of granulocytes (red) and lymphocytes (blue).

Table 4: Comparison of the results of cell composition in the *in vitro* study

Method	**Locations (# of cells)**	**Lymphocyte %** (P_{lympho})	**Granulocyte %** (P_{gran})

Spectroscopic OCT	1 (N=253)	62.0	38.0
	2 (N=219)	57.3	42.7
	3 (N=226)	63.2	36.8
	4 (N=245)	60.9	39.1
	5 (N=211)	61.7	38.3
	6 (N=228)	63.9	36.1
	Mean	61.5	39.5
Reference intensity counts by OCT before mixing (20X averaged)		60.7	39.3
Reference hemocytometer count before mixing (3X averaged)		62.1	37.9

4.4.3 *In Vivo* Pilot Study Results

For the first enrolled subject, a representative OCT B-scan with individual cells localized is shown in Fig. 26(a) and (b). We applied our spectroscopic analysis method to extract the spectrum and calculate the characteristic size of individual cells. Representative spectra of two localized cells and their best Mie spectra fits are shown in Fig. 26 (c) and (d). A total of 224 cells were successfully tracked and measured in this subject, and the histogram plot of characteristic cell sizes with mean and standard

deviation is shown in Fig. 26 (e). We then estimated the cell composition by minimizing the MSE between the measured PDF of the size distribution and a weighted combination of three reference PDFs (granulocytes, lymphocytes and monocytes) (Fig. 26(f)). For this subject, we estimated the cell composition to be 60.3% granulocytes and 39.2% mononuclear WBCs (lymphocytes: 34.3%; monocytes: 4.9%), a granulocyte vs. mononuclear WBC ratio of 1.54:1. This ratio was confirmed by the AC fluid analysis result (granulocyte vs. mononuclear WBCs =1.5:1 - 2:1).

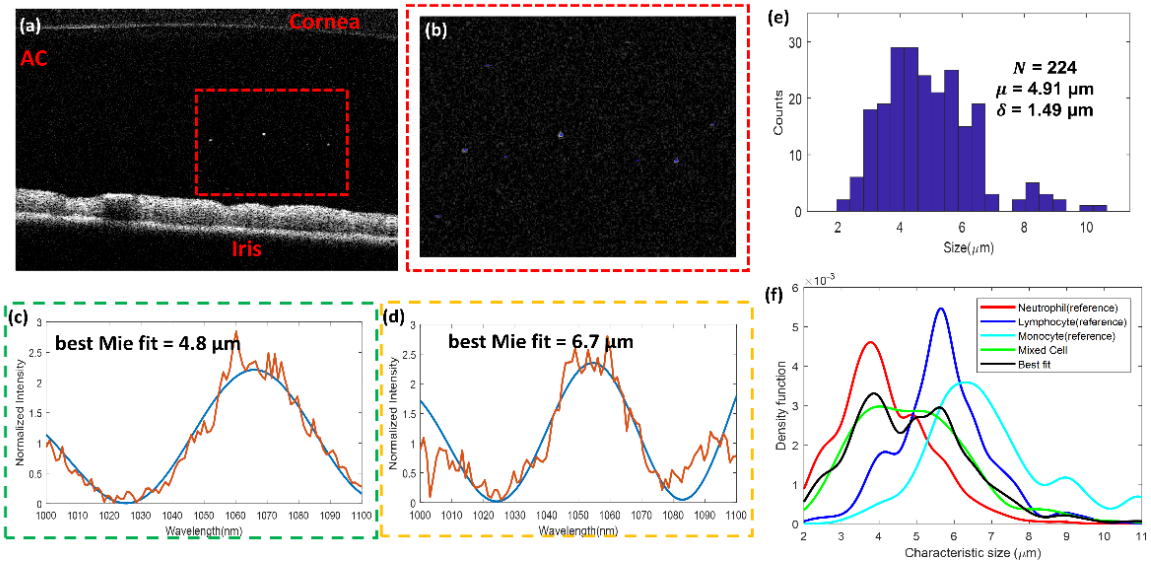

Figure 26: Results of cell composition analysis of the uveitis patient #1 in the in vivo pilot study. (a) A representative OCT B-scan of anterior chamber, and (b) a zoomed-in view with individual blood cells localized; (c-d) Two representative single cell spectra with their best Mie spectra fit. (e) Histogram plot of characteristic cell sizes extracted from the best Mie spectra fit with means and standard deviations. (f) Best fit (black) of measured characteristic size PDF with a weighted combination of reference size PDFs of granulocytes (red), lymphocytes (blue) and monocytes (cyan).

For the second enrolled uveitis subject, a total of 468 cells were successfully tracked and measured in this subject, and the histogram plot of characteristic cell sizes with mean and standard deviation is shown in Fig.27 (c). Similarly, we estimated the cell composition by fitting the measured size distribution with a weighted combination of three reference PDFs (Fig.27 d)). The cell composition was estimated to be 14.5% granulocytes and 85.5% mononuclear WBCs (lymphocytes: 19.8%; monocytes: 63.7%), while the AC paracentesis has the following results: Monocytes: 67%, lymphocytes: 22%, granulocytes: 1% and unclassified lymphoid population or unidentified cells: 10%. Although our estimated composition granulocyte is higher than the true composition (14.5% vs. 1%), the estimated compositions of lymphocytes and monocytes are very close to the true compositions (63.7% vs. 67% and 19.8% vs.22%) with an error of only 3.3% and 2.2%.

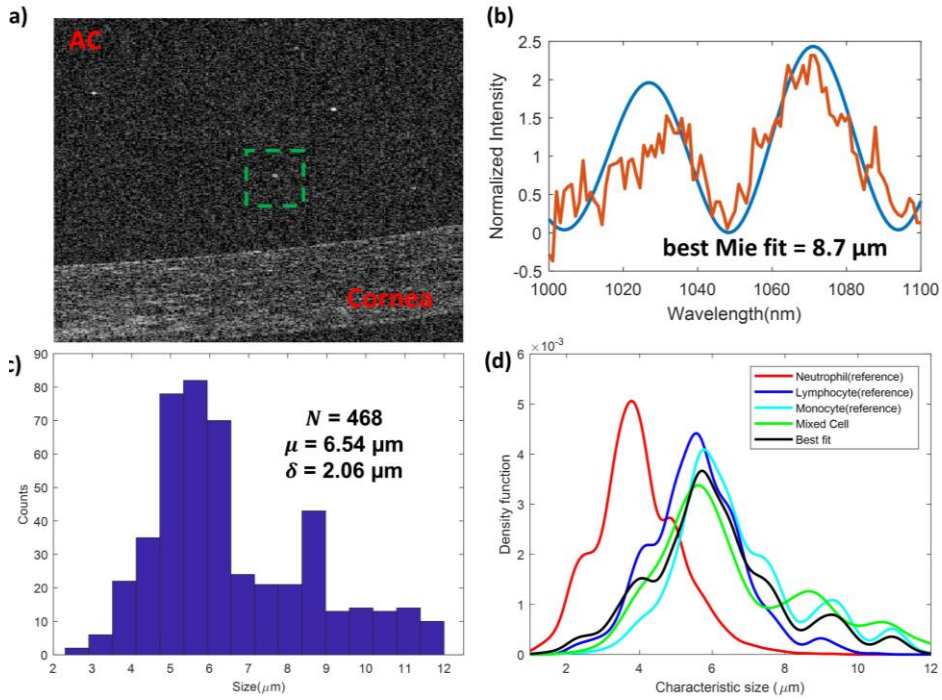

Figure 27: Results of cell composition analysis of the uveitis patient #2 in the in vivo pilot study. (a) A representative OCT B-scan of anterior chamber; (b) A representative single cell spectrum with their best Mie spectra fit; (c) Histogram plot of characteristic cell sizes extracted from the best Mie spectra fit with means and standard deviations. (b) Best fit (black) of measured characteristic size PDF with a weighted combination of reference size PDFs of granulocytes (red), lymphocytes (blue) and monocytes (cyan).

We have also successfully estimated the cell composition in 4 of 7 imaged subjects in the initial optimization stage. Too few cells were localized or successfully tracked in other 3 subjects mainly due to the motion artifacts during the OCT acquisition or the FOV was not large enough. Although the true cell compositions were not obtained from these subjects, as no AC paracentesis was performed, the estimation results using our spectroscopic methods were obtained.

4.5 Discussion

We have previously shown that all three subtypes of WBCs, granulocytes, lymphocytes and monocytes, have distinct characteristic size distributions. The size distribution of each type of cell was found to overlap with the size distributions of other types of cells, which means it is challenging to differentiate cell type at the single-cell level. However, as demonstrated in this study, we still can estimate the true composition of a cell mixture sample, by fitting the measured size distribution to a linear combination of reference size distributions of cells.

A major limitation of our technology for *in vivo* human imaging are artifacts caused by patient motion. In the *in vitro* mixture cell studies, our cell tracking algorithm was able to localize and track the majority of cells in the FOV, as individual cells have only one dominant direction of motion (direction of gravity) and we aligned the system's B-scan direction accordingly to mitigate this motion effect. However, significant eye motion artifacts were present in *in vivo* imaging and compromise the performance of our tracking algorithm. The eye motion effects were more obvious when multiple repeated volumes with a large FOV were taken, which had an acquisition time of longer than several seconds. To reduce the effect of motion artifacts, only repeated B-scan mode with a small FOV (~2 mm) was used in our pilot study. However, shortening the imaging by way of a small FOV limited number of cells can be tracked and analyzed from each acquisition. The total number of tracked cells determines the estimation

accuracy of our cell composition, as a larger number of tracked cells lead to a more accurate representation of the characteristic size distribution of the cell population. In our pilot study, only uveitis patients with a slit-lamp grading of >2+ were enrolled, and multiple acquisitions of repeated B-scans at different locations of the anterior chamber were performed in order to acquire a large enough number of tracked cells.

Multiple approaches can potentially improve the number of tracked cells in each measurement. First, as we have started to explore in our *in vivo* pilot study, optimized OCT imaging parameters (e.g. #of A-scans/B-scan, # of repeated B-scans, FOV) can minimize the motion effects between repeated B-scans and maximize the number of tracked cells in a single measurement. More quantitative studies need to be performed to find the optimal imaging protocol for in vivo imaging. Secondly, real-time eye tracking and motion compensation techniques can also significantly reduce the motion effects, such as pupil tracking [122], a robotically-aligned OCT scanner [133] or SLO-based eye tracking [123].

Moreover, WBCs from healthy donors were used to build up the reference size distributions of subtypes of WBCs in the *in vitro* studies. However, activated lymphocytes caused by the inflammatory responses such as anterior uveitis may increase in size [134], and the reference size distributions of lymphocytes obtained from the *in vitro* studies may not be a very accurate representation of lymphocytes appearing in the AC, which may lead to the error in cell composition estimation. The size

distribution of lymphocytes obtained from the AC paracentesis should be directly studied using our method and compared to the size distribution of lymphocytes obtained from the healthy donors.

4.6 Summary

We have previously shown that spectroscopic OCT analysis of single blood cells can differentiate subtypes of WBCs, including granulocytes, lymphocytes and monocytes. In this paper, we further developed our method to estimate the composition of AC blood cell mixture. The characteristic size distribution of the cell mixture sample was obtained by tracking and extracting the backscattering spectrum of single blood cells in the repeat OCT B-scans, and correlating the spectral features of single cells to their characteristic sizes using Mie theory. The probability density function of the size distribution was calculated using kernel density estimation, and fit with a weighted combination of reference size distributions of each WBC type to estimate the composition. We validated the accuracy of our method in an *in vitro* study, by comparing our estimations with two reference methods, hemocytometer and OCT images before mixing. Finally, we conducted an *in vivo* pilot study and demonstrated that our method can provide quantitative information of AC blood cell composition. The estimation results using our method in general agree with the results from AC paracentesis if available. The above described work can potentially enable noninvasive quantitative diagnosis of cellular responses in the uveitis patients in the clinic.

5 Time-frequency Multiplexed High-speed 3D Imaging

5.1 Abstract

The depth camera or 3D sensor market is growing rapidly in the past several years due to the demands in industries such as digital photography, virtual reality, self-driving car and 3D printing. There are three major types of depth sensing technologies: structured-light, stereo vision and time-of-flight. On the other hand, OCT is a 3D optical imaging modality that has micron-level axial resolution, which can potentially be a major player in the 3D imaging industry. However, current OCT technologies has two major limitations. First, the 3D depth information (the entire volume) in OCT requires substantial resources both hardware (a combination of a fast swept-source laser and a high-end digitizer) and computation (GPU-accelerated computing), to acquire, process and display in real-time. However, video rate (>30 Hz) volumetric OCT imaging with sufficient large volume sizes still remains a challenge [62]. Secondly, conventional OCT system typically only has several millimeter imaging ranging, limited by the coherence length of the laser. Thus, we develop the following optical coherence imaging technology to meet the needs of high-speed 3D imaging with high accuracy (<1mm) and high axial imaging range (> tens of centimeters). We first demonstrate theoretically and using the simulation results that, if a sample has a dominant reflector (likely the surface reflector), only <1nm bandwidth is needed to localize the depth of a dominant surface reflector with <100μn accuracy. We develop the time-frequency multiplexed 3D imaging

system by replacing one scanning galvanometer mirror in a conventional OCT system with a diffraction grating to multiplex spatial positions as a function of wavelength, which essentially a single sweep of the swept source was distributed to different locations along one axis at the imaging plane. Therefore, by performing time-frequency analysis and peak localization, the depths of reflectors along the axis can be localized within the time of a single laser sweep. By scanning the other lateral axis using a scanning mirror, the system can achieve hundreds of Hzs volumetric imaging rate. We first demonstrate the performance of this system using a conventional 100kHz swept source with 100nm bandwidth. Then, we utilize an akinetic swept source with a much longer coherence to further improve the axial imaging range of the system to 16cm and achieve submillimeter axial resolution 3D imaging with >30Hz volume rate on various samples. Our technology can be used in a broad range of non-biomedical and biomedical applications.

5.2 Introduction

In the past several years, the imaging speed of OCT has been significantly improved due to the development of high-speed swept-source lasers and high-end digitizer. For example, Fourier domain mode locking laser enables OCT imaging acquisition with multi-MHz A-scan rates and an imaging range of ~6mm when combined with a 4 GS/s sampling rate digitizer [62]. To process and display these huge amounts of data in real-time, GPU or field-programmable gate array (FPGA) accelerated

computing are required. Although the sweep rate of the swept sources and the data transfer rate of current digitizers are pushed to the limit, video rate (>30 Hz) volumetric OCT imaging with sufficient large volume sizes remains a challenge [62]. On the other hand, in many applications of OCT, particularly applications requiring real-time high-speed volumetric imaging, users mainly focus on the surface profile of OCT volumes. Therefore, most of cross-sectional depth information provided by OCT volumes is unused. For example, in microscope-integrated intraoperative OCT, surgeons used real-time retinal or corneal surface imaging for surgical guidance [73]; in the display, semiconductor and automotive industries, users relied on OCT volumes to perform non-destructive surface inspection [135]. This motivates the need for high-speed depth camera for high accuracy surface imaging.

The depth camera or sensor market is growing rapidly in the past several years due to the demands in industries such as digital photography, virtual reality, augmented reality and 3D printing. There are three major types of depth sensing technologies: structured-light, stereo vision and time-of-flight. These technologies have disadvantages such as poor performance for low feature area, computationally intensive and self-interference [136-138]. More importantly, all these technologies can't easily achieve submillimeter depth imaging accuracy. As a coherence based interferometric technology, the depth resolution of OCT is determined by the bandwidth and central wavelength of the source and is typically <10um. In this work, we built a time-frequency

multiplexed coherence-based system for high-speed high-accuracy 3D imaging. We replaced a galvo mirror in conventional OCT with a diffraction grating to perform spectrally encoded scanning in one dimension. A single sweep of the source was now distributed along one scanning axis instead of at one lateral position. We then performed time-frequency analysis and peak localization to retrieve the depth information of reflectors along the axis. We demonstrate both theoretically and experimentally that if the sample has a dominant surface reflection, the system can achieve video-rate 3D imaging with an axial resolution of several hundreds of microns, which are superior to the conventional 3D depth cameras using technologies such as structured light and time-of-flight. We further improved the imaging range of the technology to tens of centimeters scale by using an akinetic swept laser with meter range coherence length and demonstrated the performance on multiple samples.

5.3 Methods

5.3.1 Theory

In Fourier domain OCT, the Fourier transform of spectral interferogram detected by the spectrometer (spectral-domain OCT) or photodetector (swept-source OCT) results in depth-resolved reflectivity profile at the beam location (A-scan). The axial resolution of OCT is determined the coherence length of the light source, which can be calculated as: $lc = \frac{2\ln 2}{\pi}\frac{\lambda_0^2}{\Delta\lambda}$, where λ_0 and $\Delta\lambda$ are respectively the central wavelength and the bandwidth of the source. Therefore, a larger bandwidth of the source yields a higher

axial resolution. For example, a 100nm bandwidth swept source at 1050nm will lead to an axial resolution of around 7-8 μm. However, if the sample has a dominant reflector (typically the surface reflector), a much narrower bandwidth is needed to localize the reflector axially with the same level of accuracy. We first theoretically studied how much source bandwidth is required at minimum for certain axial localization accuracy. Assume a single reflector at the depth Δz, the real-valued spectral interferogram can be expressed as, $y = A\cos(2k\Delta z + \varphi) + \text{Gauss}(0, \sigma)$, where A and φ are respectively the amplitude and phase of the interference fringe, k is the wavenumber and $\text{Gauss}(0, \sigma)$ is the gaussian noise with a standard deviation of σ. Then the marginal maximum a posteriori estimator of Δz is the peak location of the Fourier transform, and the uncertainty or standard deviation of peak localization is

$$\delta z \approx \left(1.6 \times \text{SNR} \times \frac{\Delta k}{2\pi}\sqrt{N_s}\right)^{-1}, \text{[139]} \quad (5)$$

where Δk is the bandwidth, N_s is the number of sampling points, and SNR is defined as $\frac{A}{\sqrt{2}\sigma}$. The SNR can also be defined as $\sqrt{n/2}$ (n is the total number of detected photons) if the system is shot noise limited. Assume a 0.5nm bandwidth at 1050nm with 2mW of input power at sample, and 0.1% of the input power is backscattered and collected by the photodetector, with an integration time of 0.5ns (the sampling speed of our digitizer), we expect to have collected around 4027 photons, which correspond to a SNR of ~63.4. Assume we sampled 20 spectral points across the 0.5nm bandwidth, the uncertainty or standard deviation of peak localization δz = 17.7μm. The calculation here

is a simplified model that assumes there is only one reflector at a given OCT A-scan. In a more realistic scenario, the sample with a dominant surface reflector still contains multiple weak reflectors under the surface reflector. To further understand the axial localization accuracy of our method, we also performed the following simulation experiments using the conventional OCT data.

Our 100kHz swept source OCT system collected 2752 spectral points across the whole ~100nm bandwidth in a single sweep. Instead of using all 2752 spectral points to compute OCT images, we only used 20-100 spectral points, which corresponds to a bandwidth of 0.73- 3.63nm, and a theoretical OCT axial resolution of ~150-700 μm. we first zero-padded the subsampled spectral signal, and then estimated the depth by localizing the peak of the Fourier transform of the signal. To obtain the ground truth depth positions, we also processed the corresponding regular OCT A-scan using all 2752 spectral points and localize the surface depth. We did the simulations studies on both a metal and an *in vivo* human skin dataset.

5.3.2 Optical Design

In a conventional OCT system, we acquired B-scans and volumetric images by scanning the imaging beam laterally across the sample using a scanner, such as a galvanometer mirror or a MEMS scanner. Here if we want to have only a small fraction of the bandwidth in each sweep at each lateral position/A-scan of the OCT, the straightforward method is to increase the scanning speed of the scanner. However, all

these mechanical scanning modules (e.g. galvo scanner and MEMS scanner) have a maximum bandwidth of <kHz while the A-scan/sweeping rate of the OCT swept source is typically >100kHz. Therefore, the mechanical scanner is at least two-fold slower than the OCT swept source. Instead of using a mechanical scanner, our time-frequency multiplexed 3D camera uses a diffraction grating to distribute a single sweep of the swept source to different lateral locations along one axis, so that the depth profile along one axis/line can be obtained at the A-scan rate.

In spectroscopic OCT (chapter 3 and 4), the time-frequency analysis has an internal tradeoff between the axial resolution and spectral resolution. Here, since a grating distributed a spectral sweep along one lateral axis, which means the axis is spectrally encoded, the system essentially has a tradeoff between depth and lateral resolution. The spectral resolution of the time-frequency multiplexed 3D camera is similar to a conventional spectrometer, which has the spectral resolution of the system determined by the following equation [140],

$$\delta\lambda = \frac{\lambda}{R} = \frac{\lambda^2}{W\,(sinI+sinD)}, \tag{9}$$

where $\delta\lambda$ is the spectral resolution, R is the grating resolving power, W is the beam diameter, I and D are the incident and diffracted angle, which depend on the groove density (g/mm). Except the groove density, as we can see from this equation, a larger input W beam onto the grating will lead to a better spectral resolution. It is because that

a large input beam W means a larger NA of the focusing beam, which means a smaller beam spot at the focus and a better spectral resolution. Therefore, for the following system design, it was important to use the right beam size to control the lateral and axial resolution of the system.

The designed spectral resolution of the system also determines the window size of our time-frequency analysis (section 5.3.3), as we would like to have all the spectral points within the same to match the spectral resolution of the system, which means all the spectral points within the window are from the same lateral resolvable spot at the imaging plane.

Prototype Using a Conventional OCT Swept Source

For our first prototype that used a 1050nm swept source (Axsun Technologies; Billerca, MA), we plot the spectral resolution as a function of the beam (Fig 28) width at three different grating configurations (600, 800 and 1200 g/mm) and the central wavelength of 1050nm using the equation 9. Our OCT system has a spectral sampling resolution of ~0.036nm (2752 spectral points across 100nm bandwidth). For example, assume 20 spectral points are needed for each lateral location to perform depth localization, we would like to have a spectral resolution of ~0.7nm. We can achieve that by using an input beam diameter of around 2.5mm and a grating with a groove density of 600g/mm (black line).

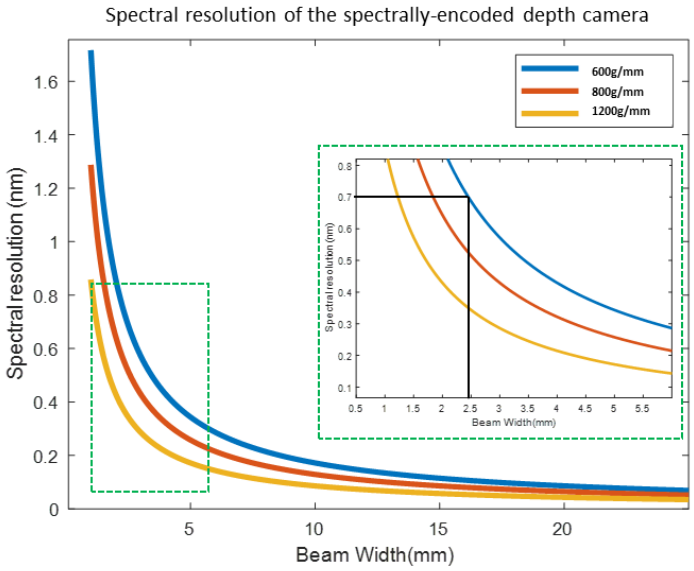

Figure 28: Spectral resolution of the time-frequency multiplexed 3D camera as a function of the input beam width.

We designed the prototype with a 2mm input beam and a 600g/mm grating in Zemax to confirm the spectral resolution and FOV. The grating is placed at one focal length away from an imaging lens with f= 100mm to create a telecentric imaging plane (Fig.29a). Different wavelengths of a single sweep were distributed to the different lateral location along one dimension. The spot diagrams at the starting wavelength (1000nm) and the ending wavelength (1100nm) were shown in Fig 29b and 29d. The FOV of the system can then be determined to be approximately 6.2mm and the lateral resolution of the system is about 62 μm. In Fig.29c, we showed the overlapped three spot diagrams from 1049.8nm (green), 1050nm (blue) and 1050.2nm (red), to demonstrate that the beam locations across a bandwidth of 0.4nm are significantly overlapped and unresolvable, which agrees with the calculation above.

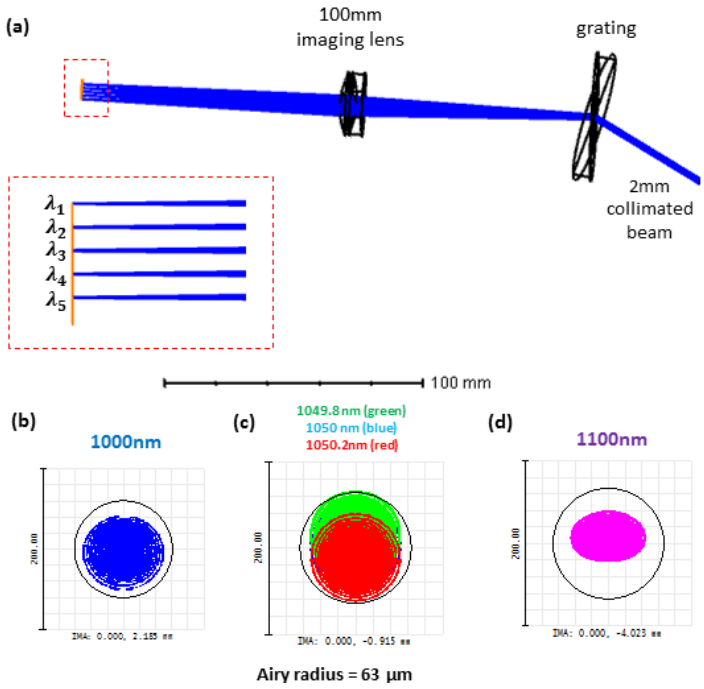

Figure 29: The Zemax design of time-frequency multiplexed 3D camera with (a) an zoom-in view of the imaging plane where different wavelengths of a single sweep were distributed to the different lateral location along one axis; the spot diagrams at (a) the starting wavelength of the sweep (1000nm), (b) three adjacent wavelengths (1049.8nm, 1050nm and 1050.2nm) and (c) the ending wavelength of the sweep (1100nm). Airy radius = 63µm

To achieve 3D imaging, a galvanometer mirror was placed at a conjugate plane before the diffraction grating formed by a pair of f=100mm achromatic doublets and used to perform orthogonal axis scanning (Fig.30). In summary, the fast axis scanning was controlled by the grating, while the slow axis scanning was controlled by the galvanometer scanner.

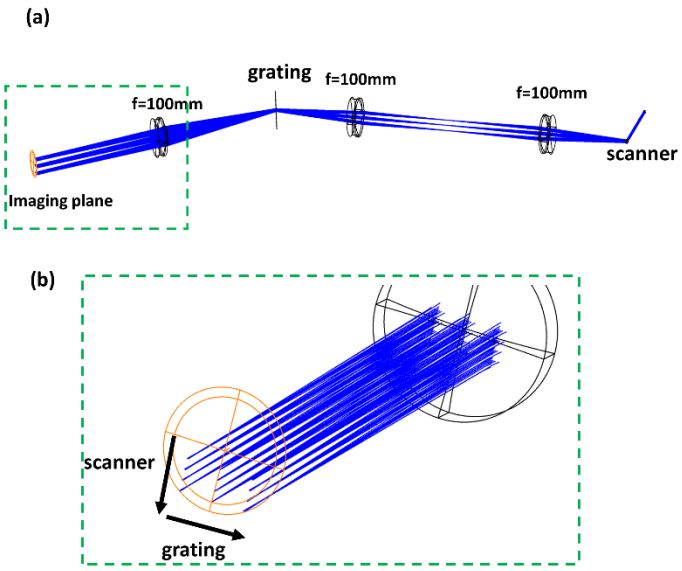

Figure 30: The Zemax design of the time-frequency multiplexed 3D camera using the diffraction grating for fast-axis scanning and the galvo mirror for slow-axis scanning, with (b) an zoom-in view of the imaging plane

Prototype Using a Long Coherence Length Swept Source

To improve the axial imaging range of our 3D camera, we utilized an Akinetic swept laser (Insight, inc; Lafayette, CO) for our second prototype. The laser has a coherence length of at least 220mm and a central wavelength of 1310nm. Moreover, both the bandwidth and sweeping rate of the laser can be adjusted from ~5nm to 70nm and from ~5kHz to 400kHz. In this application, we set the sweeping rate of the source at 16kHz and the bandwidth at 70nm.

With a sampling rate of 800MHz, a total of 48891 spectral points can be acquired within a sweep. The maximum axial imaging range is ~16 cm, limited by the bandwidth of the balanced photodetector, 400MHz.

To have the depth of focus of our imaging system comparable to the axial imaging range, 16cm, as well as maximizing the lateral FOV, the following non-telecentric imaging system was designed and built (Fig.31), and the spot diagrams at the focal plane at the starting wavelength (1275nm), the central wavelength (1310nm) and the ending wavelength (1345nm) are shown in Fig. 31(c).

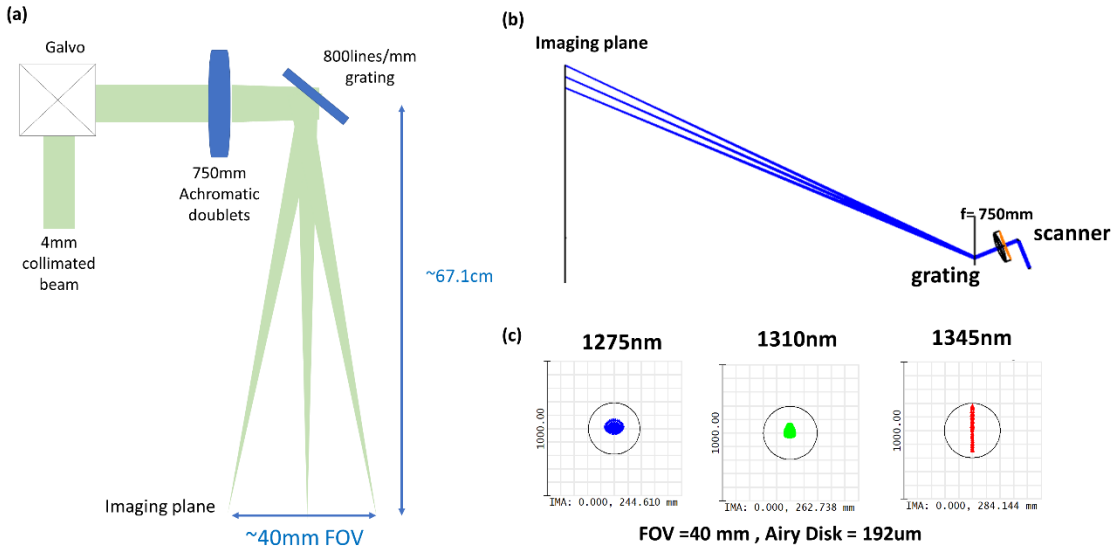

Figure 31: The optical design of the time-frequency multiplexed 3D camera using a long coherence length swept source. The (a) system and (b)Zemax design of the non-telecentric time-frequency multiplexed 3D camera using the diffraction grating for fast-axis scanning and the galvanometer for slow-axis scanning; (c) the spot diagrams at the starting (1275nm), central (1310nm) and ending (1345nm) wavelength of the sweep; Airy radius = 192μm

The system achieves a lateral spot size of 192μm, a FOV of ~40mm and a working distance (from the grating to the imaging plane) of 67.1cm.

5.3.3 Processing Methods

To retrieve the depth information from the detected spectral interferogram, the time-frequency analysis was performed. Here, for the 1050nm conventional OCT swept source system, we performed short-time Fourier transform (STFT) analysis with a Hamming window function and a window size of 20 spectral points, which corresponds to a bandwidth of approximately 0.73nm. This bandwidth is also close to the designed spectral resolution of the system (0.7nm). To achieve the Nyquist sampling, two adjacent windows are overlapped by half of the window size, 10 spectral points, which leads to the total number of windows across one sweep to be 237. For the long imaging range akinetic source system, a window size of 300 spectral points, which corresponds to a bandwidth of 0.43nm, was used. Similarly, two adjacent windows are overlapped by half of the window size, 150 spectral points, which leads to the total number of windows across one sweep to be 326. We then zeropadded each subsampled spectral signal to 10,000 sampling points and estimated the depth by finding the peak location of the Fourier transform of the signal.

5.4 Results

5.4.1 Simulation Results

We first demonstrated that to localize the depth of a dominant reflector in OCT, a much smaller bandwidth is actually needed. Here, we showed that when only 20-100

spectral points of a sweep were used for analysis, which corresponds to a bandwidth of 0.73- 3.63nm and a theoretical OCT axial resolution of ~150-700 μm, we still can localize the depth of the dominant reflector with an accuracy much better than the theoretical OCT axial resolution. Here in Fig.32, we showed that, we can localize the depth of a metal sample surface with an accuracy of <35 μm using only 20 spectral points (~0.73nm bandwidth) and human skin surface with an accuracy of <70 μm using only 40 spectral points (~1.46nm bandwidth). Fig 32(a) is a representative single B-scan of a metal along with the depth estimation calculated using only 0.73nm bandwidth (blue line) per A-scan and ground truth depth calculated using the full 100nm bandwidth (red line). We also calculated the standard deviation between estimated and ground truth depth as a function of spectral points we used across a total of 576 A-scans (Fig 32c). We performed a similar analysis on a human skin sample (Fig 32b). Although human skin as a biological sample has a much weaker surface reflection, we demonstrated that we can still achieve <70 μm depth sensing using only 40 spectral points.

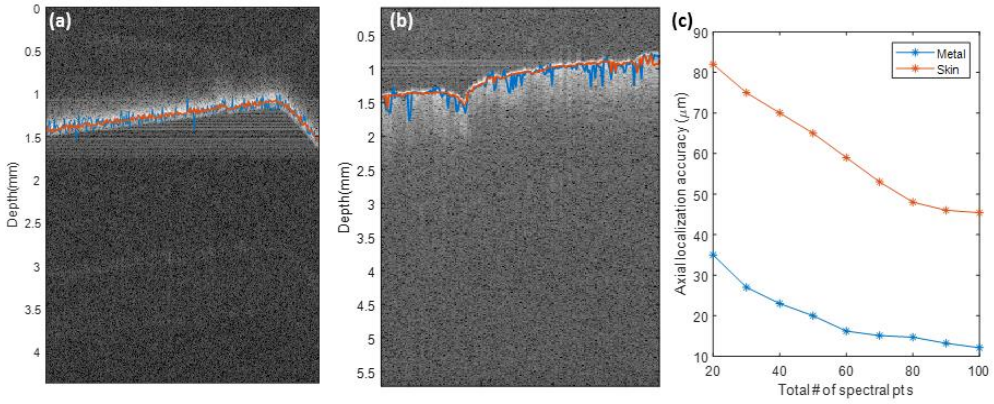

Figure 32: Simulation results of time-frequency multiplexed 3D imaging using conventional OCT data. Single OCT B-scans of (a) a metal piece and (b) human skin with the blue line representing estimated depth calculated using only 20 spectral points and the red line representing ground truth surface depth calculated using all 2752 spectral points; (c) The standard deviation between estimated and ground truth depth (axial localization accuracy) as a function of spectral points.

5.4.2 Experimental Results

Prototype Using a Conventional OCT Swept Source

We performed some preliminary testing of our prototype by imaging the depth of a metal piece. The picture of the metal piece is shown in Fig. 33(a). We performed STFT analysis on the detected spectral interferogram with a sliding window and a window size of 20 spectral points (~0.73nm) (Fig.33(b)). There is still a major difference between the data collected using the prototype and the simulated data using conventional OCT. In conventional OCT, the beam is considered to be extremely stationary for each A-scan, as the laser sweep rate is much faster than the galvo mirror scanning speed; while in our prototype, although the beam spots between adjacent wavelengths were designed to be significantly overlapped, there was still a slight lateral shift of the beam spot. Therefore,

the sub-resolution reflector profiles within the beam spot were also slightly modified, which meant beam spots of two adjacent wavelengths contained different speckle information. This speckle effect can reduce the accuracy of our depth localization measurement. One simple approach to reduce the speckle effect is to perform spatial compounding/averaging. Here, we performed slow axis scanning using the galvo mirro and calculated the averaged depth profile using the adjacent scans. The 20-averaged STFT image of the metal piece is shown in the Fig.33(c), and the localized surface depth profiles of this metal piece with 1,5 averaged,10 adveraged,20 averaged measurements are shown in Fig.33(d). We calculated the standard deviation of the localized depths at each surface to estimate the depth sensing accuracy. A depth sensing accuracy of <300 μm is achieved with single measurement, and a depth sensing accuracy of <100 μm is achieved with more than 10 averaged measurements. For the comparison purpose, the conventional OCT system with the same bandwidth (0.73nm) has only approximately ~1mm axial resolution. More importantly, a single depth measurement shown in Fig.33(d) only took 10μs to acquire. Assume 500 lateral positions along the orthogonal axis were obtained by scanning the galvanometer mirror, a 237*500 3D image with a frame rate of 200 Hz can be achieved.

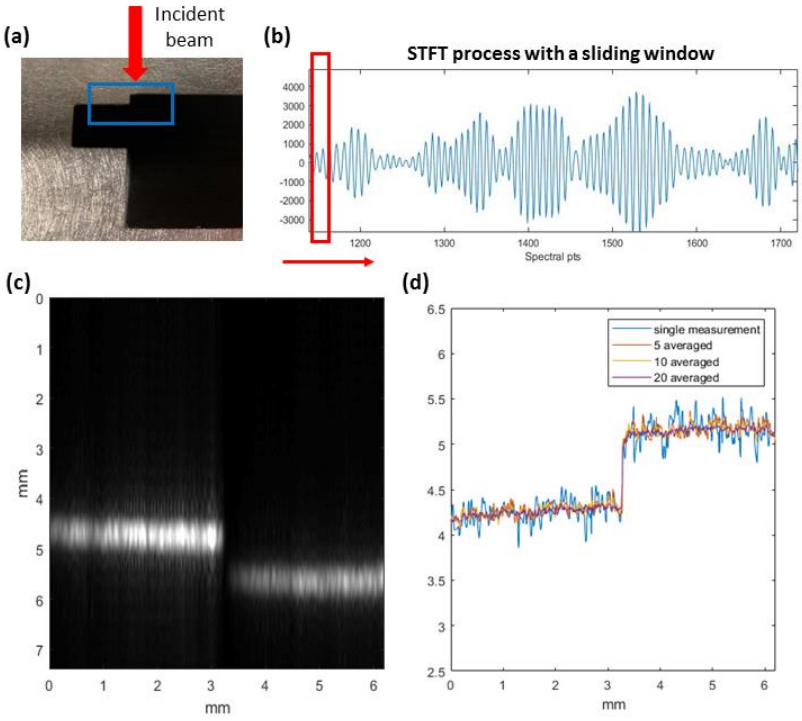

Figure 33: 3D imaging results of a metal piece corner. (a) The picture of the metal piece along with the incident beam direction (b) The STFT process with a sliding window (c) 20-averaged STFT processed image of the metal piece (d) The localized surface depth profiles of the metal piece using 1,5,10 and 20 averaged measurements

As mentioned in the method section, the imaging depth of this system using conventional OCT swept source is limited by the coherence length of the laser (~6mm), which greatly restricts the samples that can be imaged. Nevertheless, we demonstrated that this time-frequency multiplexed 3D camera prototype can acquire 3D image of a sample with a depth sensing accuracy of <300μm and a frame rate of 200Hz.

Prototype Using a Long Coherence Length Swept Source

With a much longer imaging range (16cm) of this prototype, various objects were imaged. First, we imaged a stack of five metal pieces, that spans a depth range of more than 6cm. The STFT processed image of the cross section (green line in Fig.34(d)) of the sample with a single measurement is shown in Fig.34(a), along with its localized depth profile shown in Fig.34(b). The top and front view of the sample are shown in Fig.34(c-d). Assume each metal surface is flat, we calculated the standard deviation of the localized depth profile at each surface, which is an estimation of the depth sensing accuracy of the system. The mean standard deviation across all five surfaces is 424μm, which is about 30% larger than the standard deviation obtained from the previous system (~300μm). The increased standard deviation is mainly due to 1) The bandwidth at each lateral position is smaller due to the total bandwidth of the laser has a narrower bandwidth (~70nm@1310nm) compared to the conventional OCT swept source (100nm@1050nm) and 2)The metal surfaces may not be placed exactly perpendicular to the incoming beam.

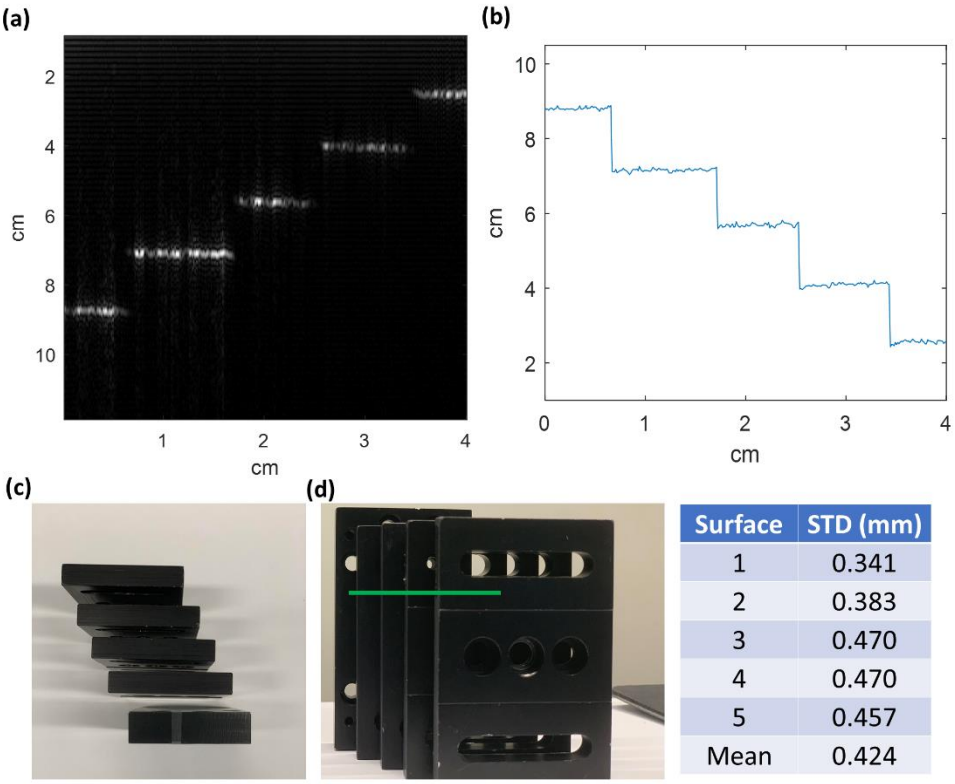

Surface	STD (mm)
1	0.341
2	0.383
3	0.470
4	0.470
5	0.457
Mean	0.424

Figure 34: 3D imaging results of a stack of metal pieces to demonstrate long imaging range. (a) the STFT processed image of the cross-section (green line in (d)) of a stack of five metal pieces with a single measurement and (b) the localized surface depth profile; (c) the top view and (d)the font view of the metal stack

Here we demonstrated that our prototype can acquire the depth profile of a cross-section with 324 laterally sampling points at a rate of ~16kHz and a depth sensing accuracy better than 424μm. We then started to acquire 3D image of the sample by scanning the slow-axis galvanometer mirror.

First, we imaged a cage plate that was placed in front of a metal. The top and side view of the sample are shown in Fig.35(d). The extracted depth map and 3D mesh surface plot of the sample (green box in Fig.35(d)) is shown in Fig.35(a) and (b). Two

representative STFT processed images of the cross sections (red and orange dashed lines in Fig.34(d)) are shown in Fig. 35(c). The depth map has 324*600 pixels and a frame rate of ~28Hz.

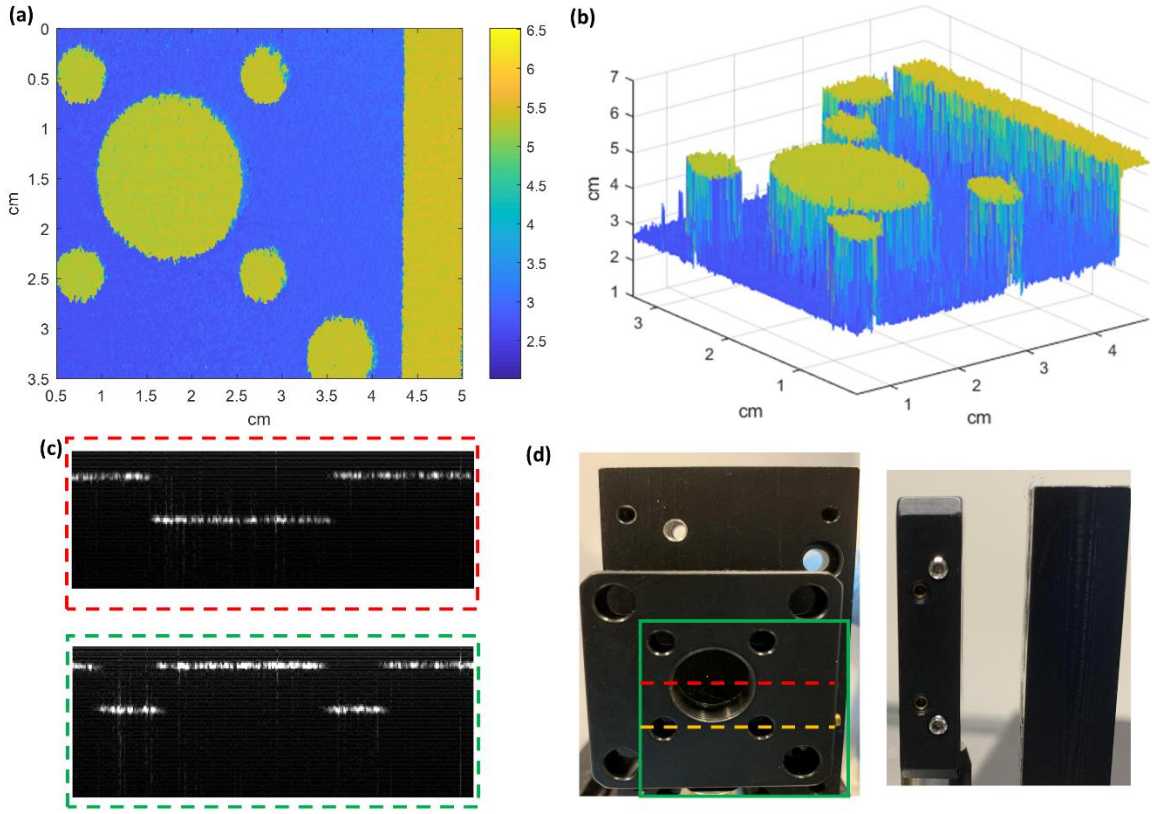

Figure 35: 3D imaging results of a cage plate placed in front of a metal plate. (a) the depth map and (b) the 3D surface plot of a cage plate; (c) two STFT processed images of the cross-sections (red and orange dashed lines in (d)) of the sample; (d) the top view and the side view of the cage plate and the metal plate.

We also imaged an Airbus 350-900 plane model. The top view of the airplane model is shown in Fig.36(d). The extracted depth map and 3D mesh surface plot of the plane (green box in Fig.36(d)) is shown in Fig.36(a) and (b). A representative STFT

processed image of the cross section (red dashed line in Fig.36(d)) are shown in Fig. 36(c). The depth map has 324*500 pixels and a frame rate of ~33.4Hz.

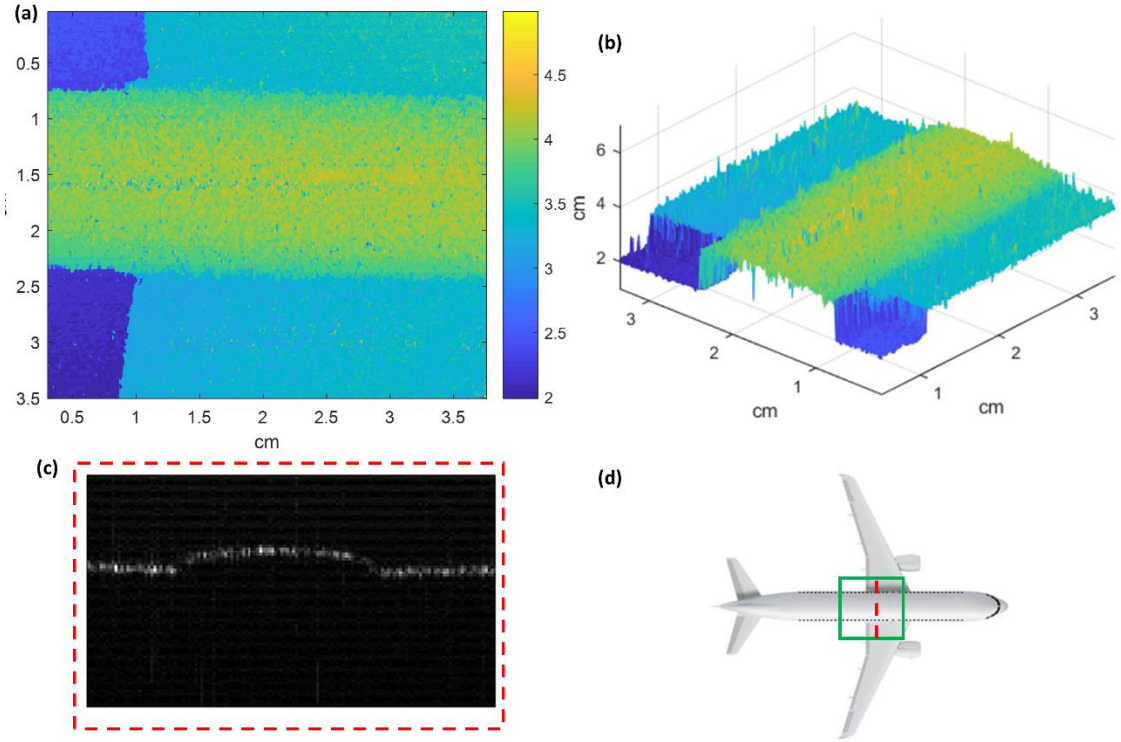

Figure 36: 3D imaging results of an airplane model. (a) the depth map and (b) the 3D surface plot of an airplane model; (c) a STFT processed image of the cross-section (red dashed line in (d)) of the plane; (d) the top view of the airplane model

Finally, we imaged a Japanese ceramic cat coin bank. The front and top view of the sample are shown in Fig.37(d). The extracted depth map and 3D mesh surface plot of the cat (green box in Fig.37(d)) is shown in Fig.36(a) and (b). A representative STFT processed image of the cross-section (red dashed line in Fig.37(d)) is shown in Fig. 37(c). The depth map has 324*500 pixels and a frame rate of ~33.4Hz.

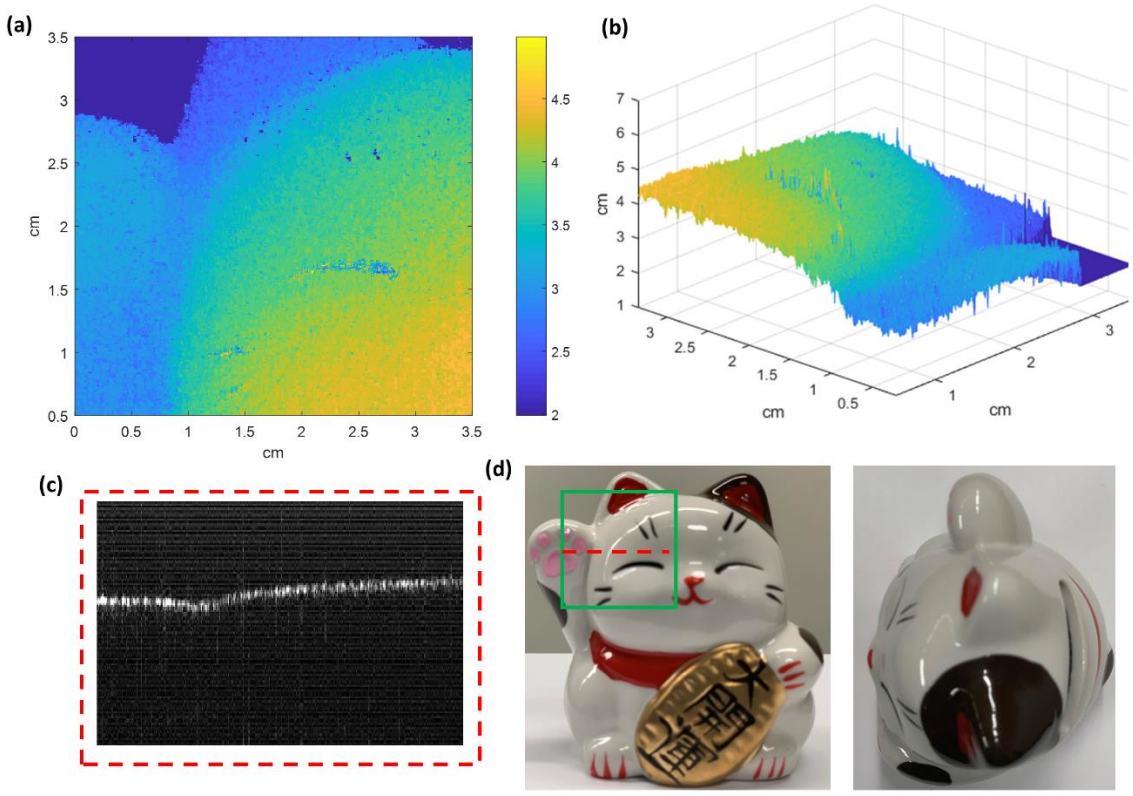

Figure 37: 3D imaging results of a cat coin bank. (a) the depth map and (b) the 3D surface plot of a ceramic cat coin bank; (c) a STFT processed image of the cross-section (red dashed line in (d)) of the sample; (d) the front and top view of the cat coin bank

5.5 Discussion

In this work, we develop a time-frequency multiplexed 3D camera with a frame rate > 30Hz and an axial imaging range of >16cm. The depth sensing accuracy of the system depends on the property of the imaged sample. In Fig.34, we demonstrate that the depth sensing accuracy is better than 400μm on metal parts. However, more testing on various types of samples which don't have dominant surface reflections like metal parts are needed in order to fully characterize the system performance. Especially,

imaging of biological samples, such as skin, is important for investigating the potential applications of this 3D camera.

The system currently has a limited FOV of ~4cm, which greatly restricted the sample that can be imaged. The limited FOV in the prototype is due to a small range of deflection angles coming out of the diffraction grating. There are three potential approaches to increase the FOV of the system: 1) use a grating with a higher groove density, for example, a 1200g/mm grating will double the current FOV; 2) add a telescope after the grating to expand the FOV ; 3) Use a longer focal length lens to increase the working distance.

The maximum axial imaging range of the current system is 16cm, which is limited by the bandwidth of the balanced photodetector. With a larger bandwidth photodetector, the imaging range of the system is ultimately limited by the digitization speed. The current system can be digitized at 4Gsamples/s, which corresponds to the maximum axial imaging range of 1.6m.

Moreover, the system design in terms of beam size and grating selection needs to be further optimized to achieve the maximum product of depth sensing accuracy and lateral resolution. The future system can also be designed with a tunable beam size into the grating, so that the depth sensing accuracy and lateral resolution of the system can be adjusted accordingly based on the sample properties, such as size and material. Other

processing approaches besides STFT and peak localization should also be considered to further improve the depth sensing accuracy.

5.6 Summary

In this work, we develop a time-frequency multiplexed 3D imaging technique that can achieve video-rate 3D imaging with submillimeter depth sensing accuracy and >16cm axial imaging range. Instead of using a mechanical scanner in conventional OCT system, this time-frequency multiplexed camera utilizes a diffraction grating to perform spectrally encoded scanning on the fast axis. Using the signal zeropadding and STFT analysis, the depth of the dominant reflector can then be localized. We first studied the depth sensing accuracy both theoretically and using the simulation data. Then we demonstrated the first prototype that uses a conventional 100kHz swept source and achieved >100Hz 3D imaging with an imaging range of ~6mm. To expand the axial imaging range, a second prototype using an Akinetic swept laser with a coherence length of meters was developed. Various samples were imaged to demonstrate the performance of the system.

6. Conclusion

The work in this dissertation describes the efforts to develop novel optical design and signal processing approaches in optical coherence imaging, mainly optical coherence tomography (OCT). OCT has become a standard of care for ophthalmic imaging. However, current OCT technologies face several limitations, including (1) difficult alignment and fixation in pediatric imaging (2) poor cellular level imaging contrast due to limited resolution and (3) expensive hardware and intensive computation requirements for real-time high-speed 3D imaging. To address these limitations, the following novel optical design and signal processing approaches were developed and demonstrated in this dissertation. First, a swept-source OCT system that incorporates two custom lenses and a novel 2f retinal scanning configuration was designed and developed to achieve a long working distance of 350mm, and the system was demonstrated to facilitate retinal imaging of young children (chapter 2). Secondly, a spectroscopic OCT method that utilizes time-frequency analysis to extract the spectrum of single cell was developed. The technique can differentiate and quantify the composition of anterior chamber blood cells noninvasively and provide quantitative diagnostic information of cellular responses in the ocular anterior chamber *in vivo*. Finally, a time-frequency multiplexed high-speed 3D imaging technique was developed. The system utilizes a grating for fast beam steering and time-frequency analysis for depth retrieval. Using a long coherence length swept laser, >video rate(30Hz) 3D

imaging with sub-millimeter axial resolution and tens of centimeters axial imaging ranging was demonstrated (chapter 5).

Bibliography

1. D. Huang, E. A. Swanson, C. P. Lin, J. S. Schuman, W. G. Stinson, W. Chang, M. R. Hee, T. Flotte, K. Gregory, C. A. Puliafito, and et al., "Optical coherence tomography," Science **254**, 1178-1181 (1991).

2. M. R. Hee, J. A. Izatt, E. A. Swanson, D. Huang, J. S. Schuman, C. P. Lin, C. A. Puliafito, and J. G. Fujimoto, "Optical coherence tomography of the human retina," Arch Ophthalmol **113**, 325-332 (1995).

3. J. A. Izatt, M. R. Hee, E. A. Swanson, C. P. Lin, D. Huang, J. S. Schuman, C. A. Puliafito, and J. G. Fujimoto, "Micrometer-scale resolution imaging of the anterior eye in vivo with optical coherence tomography," Arch Ophthalmol **112**, 1584-1589 (1994).

4. M. R. Hee, C. A. Puliafito, C. Wong, J. S. Duker, E. Reichel, J. S. Schuman, E. A. Swanson, and J. G. Fujimoto, "Optical coherence tomography of macular holes," Ophthalmology **102**, 748-756 (1995).

5. J. S. Schuman, M. R. Hee, A. V. Arya, T. Pedut-Kloizman, C. A. Puliafito, J. G. Fujimoto, and E. A. Swanson, "Optical coherence tomography: a new tool for glaucoma diagnosis," Curr Opin Ophthalmol **6**, 89-95 (1995).

6. C. A. Puliafito, M. R. Hee, C. P. Lin, E. Reichel, J. S. Schuman, J. S. Duker, J. A. Izatt, E. A. Swanson, and J. G. Fujimoto, "Imaging of macular diseases with optical coherence tomography," Ophthalmology **102**, 217-229 (1995).

7. F. Feldchtein, V. Gelikonov, R. Iksanov, G. Gelikonov, R. Kuranov, A. Sergeev, N. Gladkova, M. Ourutina, D. Reitze, and J. Warren, "In vivo OCT imaging of hard and soft tissue of the oral cavity," Opt Express **3**, 239-250 (1998).

8. J. Welzel, E. Lankenau, R. Birngruber, and R. Engelhardt, "Optical coherence tomography of the human skin," J Am Acad Dermatol **37**, 958-963 (1997).

9. G. J. Tearney, M. E. Brezinski, B. E. Bouma, S. A. Boppart, C. Pitris, J. F. Southern, and J. G. Fujimoto, "In vivo endoscopic optical biopsy with optical coherence tomography," Science **276**, 2037-2039 (1997).

10. J. G. Fujimoto, S. A. Boppart, G. J. Tearney, B. E. Bouma, C. Pitris, and M. E. Brezinski, "High resolution in vivo intra-arterial imaging with optical coherence tomography," Heart **82**, 128-133 (1999).

11. K. A. Serrels, M. K. Renner, and D. T. Reid, "Optical coherence tomography for non-destructive investigation of silicon integrated-circuits," Microelectronic Engineering **87**, 1785-1791 (2010).

12. H. Liang, M. G. Cid, R. G. Cucu, G. M. Dobre, A. G. Podoleanu, J. Pedro, and D. Saunders, "En-face optical coherence tomography - a novel application of non-invasive imaging to art conservation," Opt. Express **13**, 6133-6144 (2005).

13. Z. Wang, B. Potsaid, L. Chen, C. Doerr, H.-C. Lee, T. Nielson, V. Jayaraman, A. E. Cable, E. Swanson, and J. G. Fujimoto, "Cubic meter volume optical coherence tomography," Optica **3**, 1496-1503 (2016).

14. W. Drexler and J. G. Fujimoto, *Optical Coherence Tomography: Technology and Applications* (Springer Berlin Heidelberg, 2008).

15. S. R. Chinn, E. A. Swanson, and J. G. Fujimoto, "Optical coherence tomography using a frequency-tunable optical source," Opt. Lett. **22**, 340-342 (1997).

16. A. F. Fercher, C. K. Hitzenberger, G. Kamp, and S. Y. El-Zaiat, "Measurement of intraocular distances by backscattering spectral interferometry," Optics Communications **117**, 43-48 (1995).

17. G. Haeusler and M. Lindner, ""Coherence radar" and "Spectral radar"- new tools for dermatological diagnosis," Journal of Biomedical Optics **3**(1998).

18. F. Lexer, C. K. Hitzenberger, A. F. Fercher, and M. Kulhavy, "Wavelength-tuning interferometry of intraocular distances," Appl. Opt. **36**, 6548-6553 (1997).

19. M. A. Choma, M. V. Sarunic, C. Yang, and J. A. Izatt, "Sensitivity advantage of swept source and Fourier domain optical coherence tomography," Opt. Express **11**, 2183-2189 (2003).

20. R. Leitgeb, C. K. Hitzenberger, and A. F. Fercher, "Performance of fourier domain vs. time domain optical coherence tomography," Opt. Express **11**, 889-894 (2003).

21. J. F. de Boer, B. Cense, B. H. Park, M. C. Pierce, G. J. Tearney, and B. E. Bouma, "Improved signal-to-noise ratio in spectral-domain compared with time-domain optical coherence tomography," Opt. Lett. **28**, 2067-2069 (2003).

22. W. H. Organization, "Visual impairment and blindness" (Geneva: WHO, 2014), retrieved.

23. R. G. Mirza, M. W. Johnson, and L. M. Jampol, "Optical coherence tomography use in evaluation of the vitreoretinal interface: A review," Surv Ophthalmol **52**, 397-421 (2007).

24. M. Stopa, B. A. Bower, E. Davies, J. A. Izatt, and C. A. Toth, "Correlation of pathologic features in spectral domain optical coherence tomography with conventional retinal studies," Retina-J Ret Vit Dis **28**, 298-308 (2008).

25. P. N. Dayani, R. Maldonado, S. Farsiu, and C. A. Toth, "Intraoperative Use of Handheld Spectral Domain Optical Coherence Tomography Imaging in Macular Surgery," Retina-J Ret Vit Dis **29**, 1457-1468 (2009).

26. A. W. Scott, S. Farsiu, L. B. Enyedi, D. K. Wallace, and C. A. Toth, "Imaging the Infant Retina with a Hand-held Spectral-Domain Optical Coherence Tomography Device," Am J Ophthalmol **147**, 364-373 (2009).

27. W. Jung, J. Kim, M. Jeon, E. J. Chaney, C. N. Stewart, and S. A. Boppart, "Handheld Optical Coherence Tomography Scanner for Primary Care Diagnostics," Ieee T Bio-Med Eng **58**, 741-744 (2011).

28. F. LaRocca, D. Nankivil, T. DuBose, C. A. Toth, S. Farsiu, and J. A. Izatt, "In vivo cellular-resolution retinal imaging in infants and children using an ultracompact handheld probe," Nat Photon **advance online publication**(2016).

29. G. T. Chong, S. Farsiu, S. F. Freedman, N. Sarin, A. F. Koreishi, J. A. Izatt, and C. A. Toth, "Abnormal Foveal Morphology in Ocular Albinism Imaged With Spectral-Domain Optical Coherence Tomography," Arch Ophthalmol-Chic **127**, 37-44 (2009).

30. S. H. Chavala, S. Farsiu, R. Maldonado, D. K. Wallace, S. F. Freedman, and C. A. Toth, "Insights into Advanced Retinopathy of Prematurity Using Handheld Spectral Domain Optical Coherence Tomography Imaging," Ophthalmology **116**, 2448-2456 (2009).

31. A. Patel, R. Purohit, H. Lee, V. Sheth, G. Maconachie, E. Papageorgiou, R. J. McLean, I. Gottlob, and F. A. Proudlock, "Optic Nerve Head Development in Healthy Infants and Children Using Handheld Spectral-Domain Optical Coherence Tomography," Ophthalmology (2016).

32. R. S. Maldonado, J. A. Izatt, N. Sarin, D. K. Wallace, S. Freedman, C. M. Cotten, and C. A. Toth, "Optimizing Hand-held Spectral Domain Optical Coherence Tomography Imaging for Neonates, Infants, and Children," Invest Ophth Vis Sci **51**, 2678-2685 (2010).

33. L. Vajzovic, A. E. Hendrickson, R. V. O'Connell, L. A. Clark, D. Tran-Viet, D. Possin, S. J. Chiu, S. Farsiu, and C. A. Toth, "Maturation of the human fovea: correlation of spectral-domain optical coherence tomography findings with histology," Am J Ophthalmol **154**, 779-789 e772 (2012).

34. R. S. Maldonado, R. V. O'Connell, N. Sarin, S. F. Freedman, D. K. Wallace, C. M. Cotten, K. P. Winter, S. Stinnett, S. J. Chiu, J. A. Izatt, S. Farsiu, and C. A. Toth, "Dynamics of human foveal development after premature birth," Ophthalmology **118**, 2315-2325 (2011).

35. H. Lee, F. Proudlock, and I. Gottlob, "Is Handheld Optical Coherence Tomography Reliable in Infants and Young Children With and Without

Nystagmus?Reliability of Handheld OCT in Young Children," Invest Ophth Vis Sci **54**, 8152-8159 (2013).

36. L. Vajzovic, A. L. Rothman, D. Tran-Viet, M. T. Cabrera, S. F. Freedman, and C. A. Toth, "Delay in Retinal Photoreceptor Development in Very Preterm Compared to Term Infants," Invest Ophth Vis Sci **56**, 908-913 (2015).

37. A. Vinekar, K. Avadhani, M. Sivakumar, P. Mahendradas, M. Kurian, S. Braganza, R. Shetty, and B. K. Shetty, "Understanding clinically undetected macular changes in early retinopathy of prematurity on spectral domain optical coherence tomography," Invest Ophthalmol Vis Sci **52**, 5183-5188 (2011).

38. A. Vinekar, S. Mangalesh, C. Jayadev, R. S. Maldonado, N. Bauer, and C. A. Toth, "Retinal Imaging of Infants on Spectral Domain Optical Coherence Tomography," Biomed Res Int (2015).

39. A. Mallipatna, A. Vinekar, C. Jayadev, S. Dabir, M. Sivakumar, N. Krishnan, P. Mehta, T. Berendschot, and N. K. Yadav, "The use of handheld spectral domain optical coherence tomography in pediatric ophthalmology practice: Our experience of 975 infants and children," Indian J Ophthalmol **63**, 586-593 (2015).

40. R. S. Maldonado, E. Yuan, D. Tran-Viet, A. L. Rothman, A. Y. Tong, D. K. Wallace, S. F. Freedman, and C. A. Toth, "Three-Dimensional Assessment of Vascular and Perivascular Characteristics in Subjects with Retinopathy of Prematurity," Ophthalmology **121**, 1289-1296 (2014).

41. R. S. Maldonado and C. A. Toth, "Optical Coherence Tomography in Retinopathy of Prematurity Looking Beyond the Vessels," Clin Perinatol **40**, 271-+ (2013).

42. A. L. Rothman, T. V. Du, L. Vajzovic, V. Tai, N. Sarin, S. Holgado, K. E. Gustafson, C. M. Cotten, S. F. Freedman, and C. A. Toth, "Functional Outcomes of Young Infants with and without Macular Edema," Retina-J Ret Vit Dis **35**, 2018-2027 (2015).

43. M. K. Erol, O. Ozdemir, D. T. Coban, A. B. Bilgin, B. Dogan, E. S. Sari, and D. Toslak, "Macular Findings Obtained by Spectral Domain Optical Coherence Tomography in Retinopathy of Prematurity," J Ophthalmol (2014).

44. A. Vinekar, S. Mangalesh, C. Jayadev, N. Bauer, S. Munusamy, V. Kemmanu, M. Kurian, P. Mahendradas, K. Avadhani, and B. Shetty, "Macular edema in Asian Indian premature infants with retinopathy of prematurity: Impact on visual acuity and refractive status after 1-year," Indian J Ophthalmol **63**, 432-437 (2015).

45. A. M. Dubis, C. D. Subramaniam, P. Godara, J. Carroll, and D. M. Costakos, "Subclinical Macular Findings in Infants Screened for Retinopathy of Prematurity with Spectral-Domain Optical Coherence Tomography," Ophthalmology **120**, 1665-1671 (2013).

46. T. H. Cronin, R. W. Hertle, H. Ishikawa, and J. S. Schuman, "Spectral domain optical coherence tomography for detection of foveal morphology in patients with nystagmus," J AAPOS **13**, 563-566 (2009).

47. H. Lee, V. Sheth, M. Bibi, G. Maconachie, A. Patel, R. J. McLean, M. Michaelides, M. G. Thomas, F. A. Proudlock, and I. Gottlob, "Potential of Handheld Optical Coherence Tomography to Determine Cause of Infantile Nystagmus in Children by Using Foveal Morphology," Ophthalmology **120**, 2714-2724 (2013).

48. R. H. Muni, R. P. Kohly, E. H. Sohn, and T. C. Lee, "Hand-held spectral domain optical coherence tomography finding in shaken-baby syndrome," Retina **30**, S45-50 (2010).

49. C. Viehland, X. Chen, D. Tran-Viet, M. Jackson-Atogi, P. Ortiz, G. Waterman, L. Vajzovic, C. A. Toth, and J. A. Izatt, "Ergonomic handheld OCT angiography probe optimized for pediatric and supine imaging," Biomed. Opt. Express **10**, 2623-2638 (2019).

50. S. Song, K. Zhou, J. J. Xu, Q. Zhang, S. Lyu, and R. Wang, "Development of a clinical prototype of a miniature hand-held optical coherence tomography probe for prematurity and pediatric ophthalmic imaging," Biomed. Opt. Express **10**, 2383-2398 (2019).

51. U. Morgner, W. Drexler, F. X. Kärtner, X. D. Li, C. Pitris, E. P. Ippen, and J. G. Fujimoto, "Spectroscopic optical coherence tomography," Opt. Lett. **25**, 111-113 (2000).

52. A. L. Oldenburg, C. Xu, and S. A. Boppart, "Spectroscopic Optical Coherence Tomography and Microscopy," IEEE Journal of Selected Topics in Quantum Electronics **13**, 1629-1640 (2007).

53. F. E. Robles and A. Wax, "Measuring morphological features using light-scattering spectroscopy and Fourier-domain low-coherence interferometry," Opt. Lett. **35**, 360-362 (2010).

54. F. E. Robles, C. Wilson, G. Grant, and A. Wax, "Molecular imaging true-colour spectroscopic optical coherence tomography," Nat Photonics **5**, 744-747 (2011).

55. J. Yi, Q. Wei, W. Liu, V. Backman, and H. F. Zhang, "Visible-light optical coherence tomography for retinal oximetry," Opt Lett **38**, 1796-1798 (2013).

56. Y. Zhao, J. R. Maher, J. Kim, M. A. Selim, H. Levinson, and A. Wax, "Evaluation of burn severity in vivo in a mouse model using spectroscopic optical coherence tomography," Biomed Opt Express **6**, 3339-3345 (2015).

57. C. Xu, F. Kamalabadi, and S. A. Boppart, "Comparative performance analysis of time-frequency distributions for spectroscopic optical coherence tomography," Appl Opt **44**, 1813-1822 (2005).

58. F. Robles, R. N. Graf, and A. Wax, "Dual window method for processing spectroscopic optical coherence tomography signals with simultaneously high spectral and temporal resolution," Opt Express **17**, 6799-6812 (2009).

59. K. C. Zhou, R. Qian, S. Farsiu, and J. A. Izatt, "Spectroscopic optical coherence refraction tomography," Opt. Lett. **45**, 2091-2094 (2020).

60. T. Klein and R. Huber, "High-speed OCT light sources and systems [Invited]," Biomed Opt Express **8**, 828-859 (2017).

61. T. Klein, W. Wieser, L. Reznicek, A. Neubauer, A. Kampik, and R. Huber, "Multi-MHz retinal OCT," Biomed Opt Express **4**, 1890-1908 (2013).

62. J. P. Kolb, W. Draxinger, J. Klee, T. Pfeiffer, M. Eibl, T. Klein, W. Wieser, and R. Huber, "Live video rate volumetric OCT imaging of the retina with multi-MHz A-scan rates," PLoS One **14**, e0213144 (2019).

63. S. Song, J. Xu, and R. K. Wang, "Long-range and wide field of view optical coherence tomography for in vivo 3D imaging of large volume object based on akinetic programmable swept source," Biomed Opt Express **7**, 4734-4748 (2016).

64. T. DiLazaro and G. Nehmetallah, "Large-volume, low-cost, high-precision FMCW tomography using stitched DFBs," Opt. Express **26**, 2891-2904 (2018).

65. D. Huang, E. A. Swanson, C. P. Lin, J. S. Schuman, W. G. Stinson, W. Chang, M. R. Hee, T. Flotte, K. Gregory, C. A. Puliafito, and J. G. Fujimoto, "Optical Coherence Tomography," Science **254**, 1178-1181 (1991).

66. Q. Zhang, C. S. Lee, J. Chao, C.-L. Chen, T. Zhang, U. Sharma, A. Zhang, J. Liu, K. Rezaei, K. L. Pepple, R. Munsen, J. Kinyoun, M. Johnstone, R. N. Van Gelder, and R. K. Wang, "Wide-field optical coherence tomography based microangiography for retinal imaging," Scientific Reports **6**, 22017 (2016).

67. H. Lee, R. Purohit, A. Patel, E. Papageorgiou, V. Sheth, G. Maconachie, A. Pilat, R. J. McLean, F. A. Proudlock, and I. Gottlob, "In Vivo Foveal Development Using Optical Coherence Tomography," Invest Ophth Vis Sci **56**, 4537-4545 (2015).

68. S. J. Chiu, X. T. Li, P. Nicholas, C. A. Toth, J. A. Izatt, and S. Farsiu, "Automatic segmentation of seven retinal layers in SDOCT images congruent with expert manual segmentation," Opt Express **18**, 19413-19428 (2010).

69. A. V. Goncharov and C. Dainty, "Wide-field schematic eye models with gradient-index lens," J Opt Soc Am A Opt Image Sci Vis **24**, 2157-2174 (2007).

70. O. M. Carrasco-Zevallos, R. Qian, N. Gahm, J. Migacz, C. A. Toth, and J. A. Izatt, "Long working distance OCT with a compact 2f retinal scanning configuration for pediatric imaging," Opt Lett **41**, 4891-4894 (2016).

71. S. G. Guo, R. Hutchison, R. P. Jackson, A. Kohli, T. Sharp, E. Orwin, R. Haskell, Z. P. Chen, and B. J. F. Wong, "Office-based optical coherence tomographic imaging of human vocal cords," J Biomed Opt **11**(2006).

72. S. A. Boppart, B. E. Bouma, C. Pitris, J. F. Southern, M. E. Brezinski, and J. G. Fujimoto, "Intraoperative assessment of microsurgery with three-dimensional optical coherence tomography," Radiology **208**, 81-86 (1998).

73. O. M. Carrasco-Zevallos, B. Keller, C. Viehland, L. Shen, G. Waterman, B. Todorich, C. Shieh, P. Hahn, S. Farsiu, A. N. Kuo, C. A. Toth, and J. A. Izatt, "Live volumetric (4D) visualization and guidance of in vivo human ophthalmic surgery with intraoperative optical coherence tomography," Sci Rep **6**, 31689 (2016).

74. Y. K. Tao, S. K. Srivastava, and J. P. Ehlers, "Microscope-integrated intraoperative OCT with electrically tunable focus and heads-up display for imaging of ophthalmic surgical maneuvers," Biomed Opt Express **5**, 1877-1885 (2014).

75. P. F. Sharp and A. Manivannan, "The scanning laser ophthalmoscope," Phys Med Biol **42**, 951-966 (1997).

76. R. H. Webb, G. W. Hughes, and F. C. Delori, "Confocal Scanning Laser Ophthalmoscope," Appl Optics **26**, 1492-1499 (1987).

77. A. Dubra, A. Gómez-Vieyra, L. Díaz-Santana, and Y. Sulai, "Optical Design of Clinical Adaptive Optics Instruments for Retinal Imaging," in *Frontiers in Optics 2010/Laser Science XXVI*, OSA Technical Digest (CD) (Optical Society of America, 2010), FTuB3.

78. K. Irsch, B. I. Gramatikov, Y. K. Wu, and D. L. Guyton, "New pediatric vision screener employing polarization-modulated, retinal-birefringence-scanning-based strabismus detection and bull's eye focus detection with an improved

target system: opto-mechanical design and operation," J Biomed Opt **19**, 067004 (2014).

79. O. Carrasco-Zevallos, D. Nankivil, B. Keller, C. Viehland, B. J. Lujan, and J. A. Izatt, "Pupil tracking optical coherence tomography for precise control of pupil entry position," Biomed Opt Express **6**, 3405-3419 (2015).

80. B. I. Gramatikov, S. Rangarajan, K. Irsch, and D. L. Guyton, "Attention attraction in an ophthalmic diagnostic device using sound-modulated fixation targets," Med Eng Phys **38**, 818-821 (2016).

81. M. F. Kraus, B. Potsaid, M. A. Mayer, R. Bock, B. Baumann, J. J. Liu, J. Hornegger, and J. G. Fujimoto, "Motion correction in optical coherence tomography volumes on a per A-scan basis using orthogonal scan patterns," Biomed Opt Express **3**, 1182-1199 (2012).

82. J. Lezama, D. Mukherjee, R. P. McNabb, G. Sapiro, A. N. Kuo, and S. Farsiu, "Segmentation guided registration of wide field-of-view retinal optical coherence tomography volumes," Biomed Opt Express **7**, 4827-4846 (2016).

83. Z. Wang, B. Potsaid, L. Chen, C. Doerr, H. C. Lee, T. Nielson, V. Jayaraman, A. E. Cable, E. Swanson, and J. G. Fujimoto, "Cubic meter volume optical coherence tomography," Optica **3**, 1496-1503 (2016).

84. W. Walton, S. Von Hagen, R. Grigorian, and M. Zarbin, "Management of traumatic hyphema," Surv. Ophthalmol. **47**, 297-334 (2002).

85. J. H. Chang, P. J. McCluskey, and D. Wakefield, "Acute anterior uveitis and HLA-B27," Surv Ophthalmol **50**, 364-388 (2005).

86. C. J. Chu, P. J. Gardner, D. A. Copland, S. E. Liyanage, A. Gonzalez-Cordero, S. M. Kleine Holthaus, U. F. Luhmann, A. J. Smith, R. R. Ali, and A. D. Dick, "Multimodal analysis of ocular inflammation using the endotoxin-induced uveitis mouse model," Dis Model Mech **9**, 473-481 (2016).

87. N. Biophysical JournalDis Model MechDave, P. Chevour, P. Mahendradas, A. Venkatesh, A. Kawali, R. Shetty, A. Ghosh, and S. Sethu, "Increased Aqueous Humor CD4+/CD8+ Lymphocyte Ratio in Sarcoid Uveitis," Ocul. Immunol. Inflamm., 1-8 (2018).

88. A. Baltmr, S. Lightman, and O. Tomkins-Netzer, "Vogt-Koyanagi-Harada syndrome - current perspectives," Clin. Ophthalmol. **10**, 2345-2361 (2016).

89. R.S. Moorthy, P.L. Rao, R.W. Read, R.N. Van Gelder, A.T. Vitale, B. Bodaghi, and C. M. Parrish., *Intraocular inflammation and uveitis*, Basic and clinical science course (American Academy of Ophthalmology, San Francisco, CA, 2014), pp. xii, 370 pages.

90. T. H. Flynn, N. A. Mitchison, S. J. Ono, and D. F. P. Larkin, "Aqueous humor alloreactive cell phenotypes, cytokines and chemokines in corneal allograft rejection," Am. J. Transplant. **8**, 1537-1543 (2008).

91. A. Van der Lelij and A. Rothova, "Diagnostic anterior chamber paracentesis in uveitis: a safe procedure?," Br. J. Ophthalmol. **81**, 976-979 (1997).

92. J. A. Izatt, M. R. Hee, E. A. Swanson, C. P. Lin, D. Huang, J. S. Schuman, C. A. Puliafito, and J. G. Fujimoto, "Micrometer-Scale Resolution Imaging of the Anterior Eye in-Vivo with Optical Coherence Tomography," Arch. Ophthalmol. **112**, 1584-1589 (1994).

93. A. Agarwal, D. Ashokkumar, S. Jacob, A. Agarwal, and Y. Saravanan, "High-speed Optical Coherence Tomography for Imaging Anterior Chamber Inflammatory Reaction in Uveitis: Clinical Correlation and Grading," Am. J. Ophthalmol. **147**, 413-416 (2009).

94. Y. Li, C. Lowder, X. Zhang, and D. Huang, "Anterior chamber cell grading by optical coherence tomography," Invest. Ophthalmol. Vis. Sci. **54**, 258-265 (2013).

95. A. O. Igbre, M. C. Rico, and S. J. Garg, "High-Speed Optical Coherence Tomography as a Reliable Adjuvant Tool to Grade Ocular Anterior Chamber Inflammation," Retina **34**, 504-508 (2014).

96. M. Edmond, A. Yuan, B. A. Bell, A. Sharma, R. M. DiCicco, L. Tucker, J. Bena, Y. K. Tao, and S. K. Srivastava, "The Feasibility of Spectral-Domain Optical Coherence Tomography Grading of Anterior Chamber Inflammation in a Rabbit Model of Anterior Uveitis," Invest. Ophthalmol. Vis. Sci. **57**, Oct184-Oct188 (2016).

97. W. J. Choi, K. L. Pepple, and R. K. Wang, "Automated three-dimensional cell counting method for grading uveitis of rodent eye in vivo with optical coherence tomography," J. Biophotonics **11**, e201800140 (2018).

98. M. Diez-Silva, M. Dao, J. Han, C. T. Lim, and S. Suresh, "Shape and Biomechanical Characteristics of Human Red Blood Cells in Health and Disease," MRS Bull **35**, 382-388 (2010).

99. T. Sun and ebrary Inc., "Atlas of hematologic neoplasms," (Springer,, Boston, MA, 2009), pp. xi, 525 p.

100. J. Rose-Nussbaumer, Y. Li, P. Lin, E. Suhler, M. Asquith, J. T. Rosenbaum, and D. Huang, "Aqueous Cell Differentiation in Anterior Uveitis Using Fourier-Domain Optical Coherence Tomography," Invest. Ophthalmol. Vis. Sci. **56**, 1430-1436 (2015).

101. P. Ossowski, A. Raiter-Smiljanic, A. Szkulmowska, D. Bukowska, M. Wiese, L. Derzsi, A. Eljaszewicz, P. Garstecki, and M. Wojtkowski, "Differentiation of morphotic elements in human blood using optical coherence tomography and a microfluidic setup," Opt. Express **23**, 27724-27738 (2015).

102. M. Goel, R. G. Picciani, R. K. Lee, and S. K. Bhattacharya, "Aqueous humor dynamics: a review," Open. Ophthalmol. J. **4**, 52-59 (2010).

103. R. Leitgeb, M. Wojtkowski, A. Kowalczyk, C. K. Hitzenberger, M. Sticker, and A. F. Fercher, "Spectral measurement of absorption by spectroscopic frequency-domain optical coherence tomography," Opt. Lett. **25**, 820-822 (2000).

104. J. A. Izatt, M. A. Choma, and A.-H. Dhalla, "Theory of Optical Coherence Tomography," in *Optical Coherence Tomography: Technology and Applications*, W.

Drexler and J. G. Fujimoto, eds. (Springer International Publishing, Cham, 2015), pp. 65-94.

105. C. Xu, P. S. Carney, and S. A. Boppart, "Wavelength-dependent scattering in spectroscopic optical coherence tomography," Opt. Express **13**, 5450-5462 (2005).

106. P. Laven, (2018), retrieved http://www.philiplaven.com/mieplot.htm.

107. I. Grulkowski, J. J. Liu, J. Y. Zhang, B. Potsaid, V. Jayaraman, A. E. Cable, J. S. Duker, and J. G. Fujimoto, "Reproducibility of a Long-Range Swept-Source Optical Coherence Tomography Ocular Biometry System and Comparison with Clinical Biometers," Ophthalmology **120**, 2184-2190 (2013).

108. C. G. Liu, C. Capjack, and W. Rozmus, "3-D simulation of light scattering from biological cells and cell differentiation," J. Biomed. Opt. **10**, 014007 (2005).

109. A. Hsiao, M. Hunter, C. Greiner, S. Gupta, and I. Georgakoudi, "Noninvasive identification of subcellular organization and nuclear morphology features associated with leukemic cells using light-scattering spectroscopy," J. Biomed. Opt. **16**, 037007 (2011).

110. J. Yoon, K. Kim, H. Park, C. Choi, S. Jang, and Y. Park, "Label-free characterization of white blood cells by measuring 3D refractive index maps," Biomed. Opt. Express **6**, 3865-3875 (2015).

111. M. Habaza, M. Kirschbaum, C. Guernth-Marschner, G. Dardikman, I. Barnea, R. Korenstein, C. Duschl, and N. T. Shaked, "Rapid 3D Refractive-Index Imaging of Live Cells in Suspension without Labeling Using Dielectrophoretic Cell Rotation," Adv. Sci. **4**, 1600205 (2017).

112. R. R. Liu, G. Spicer, S. Y. Chen, H. F. Zhang, J. Yi, and V. Backman, "Theoretical model for optical oximetry at the capillary level: exploring hemoglobin oxygen saturation through backscattering of single red blood cells," J. Biomed. Opt. **22**, 025002 (2017).

113. J. Lim, H. F. Ding, M. Mir, R. Y. Zhu, K. Tangella, and G. Popescu, "Born approximation model for light scattering by red blood cells," Biomed. Opt. Express **2**, 2784-2791 (2011).

114. A. M. K. Nilsson, P. Alsholm, A. Karlsson, and S. Andersson-Engels, "T-matrix computations of light scattering by red blood cells," Appl. Optics **37**, 2735-2748 (1998).

115. J. Q. Lu, P. Yang, and X. H. Hu, "Simulations of light scattering from a biconcave red blood cell using the finite-difference time-domain method," J. Biomed. Opt. **10**, 024022 (2005).

116. Y. K. Li, J. Hu, W. F. Huang, Z. P. Nie, and Q. H. Liu, "A Spectral Integral Method for Smooth Multilayered Bodies of Revolution," IEEE Trans. Antennas Propag. **65**, 4146-4154 (2017).

117. Y. C. Fung, W. C. Tsang, and P. Patitucci, "High-resolution data on the geometry of red blood cells," Biorheology **18**, 369-385 (1981).

118. M. A. Yurkin, K. A. Semyanov, P. A. Tarasov, A. V. Chernyshev, A. G. Hoekstra, and V. P. Maltsev, "Experimental and theoretical study of light scattering by individual mature red blood cells by use of scanning flow cytometry and a discrete dipole approximation," Appl. Optics **44**, 5249-5256 (2005).

119. D. A. Fedosov, B. Caswell, and G. E. Karniadakis, "A Multiscale Red Blood Cell Model with Accurate Mechanics, Rheology, and Dynamics," Biophys. J. **98**, 2215-2225 (2010).

120. G. I. Ruban, S. M. Kosmacheva, N. V. Goncharova, D. Van Bockstaele, and V. A. Loiko, "Investigation of morphometric parameters for granulocytes and lymphocytes as applied to a solution of direct and inverse light-scattering problems," J. Biomed. Opt. **12**, 044017 (2007).

121. Y. K. Chan, M. H. Tsai, D. C. Huang, Z. H. Zheng, and K. D. Hung, "Leukocyte nucleus segmentation and nucleus lobe counting," BMC Bioinformatics **11**, 558 (2010).

122. O. M. Carrasco-Zevallos, D. Nankivil, C. Viehland, B. Keller, and J. A. Izatt, "Pupil Tracking for Real-Time Motion Corrected Anterior Segment Optical Coherence Tomography," PLoS One **11**, e0162015 (2016).

123. K. V. Vienola, B. Braaf, C. K. Sheehy, Q. Yang, P. Tiruveedhula, D. W. Arathorn, J. F. de Boer, and A. Roorda, "Real-time eye motion compensation for OCT imaging with tracking SLO," Biomed. Opt. Express **3**, 2950-2963 (2012).

124. M. J. Hogan, S. J. Kimura, and P. Thygeson, "Signs and Symptoms of Uveitis*: I. Anterior Uveitis," Am. J. Ophthalmol. **47**, 155-170 (1959).

125. H. Shankar, D. Taranath, C. T. Santhirathelagan, and K. Pesudovs, "Anterior segment biometry with the Pentacam: comprehensive assessment of repeatability of automated measurements," J. Cataract. Refract. Surg. **34**, 103-113 (2008).

126. J. S. Harthan, D. L. Opitz, S. R. Fromstein, and C. E. Morettin, "Diagnosis and treatment of anterior uveitis: optometric management," Clin Optom (Auckl) **8**, 23-35 (2016).

127. R. Maini, J. O'Sullivan, A. Reddy, S. Watson, and C. Edelsten, "The risk of complications of uveitis in a district hospital cohort," Br J Ophthalmol **88**, 512-517 (2004).

128. R. L. Smit, G. S. Baarsma, and J. de Vries, "Classification of 750 consecutive uveitis patients in the Rotterdam Eye Hospital," Int Ophthalmol **17**, 71-76 (1993).

129. A. Rothova, M. S. Suttorp-van Schulten, W. Frits Treffers, and A. Kijlstra, "Causes and frequency of blindness in patients with intraocular inflammatory disease," Br J Ophthalmol **80**, 332-336 (1996).

130. D. A. Jabs, R. B. Nussenblatt, J. T. Rosenbaum, and G. Standardization of Uveitis Nomenclature Working, "Standardization of uveitis nomenclature for reporting clinical data. Results of the First International Workshop," Am J Ophthalmol **140**, 509-516 (2005).

131. C. M. Cheung, O. M. Durrani, and P. I. Murray, "The safety of anterior chamber paracentesis in patients with uveitis," Br J Ophthalmol **88**, 582-583 (2004).

132. R. Qian, W. F. Huang, R. P. McNabb, K. C. Zhou, Q. H. Liu, A. N. Kuo, and J. A. Izatt, "Ocular anterior chamber blood cell population differentiation using spectroscopic optical coherence tomography," Biomed Opt Express **10**, 3281-3300 (2019).

133. M. Draelos, P. Ortiz, R. Qian, B. Keller, K. Hauser, A. Kuo, and J. Izatt, "Automatic Optical Coherence Tomography Imaging of Stationary and Moving Eyes with a Robotically-Aligned Scanner," in *2019 International Conference on Robotics and Automation (ICRA)*, 2019), 8897-8903.

134. B. M. Iritani, J. Delrow, C. Grandori, I. Gomez, M. Klacking, L. S. Carlos, and R. N. Eisenman, "Modulation of T-lymphocyte development, growth and cell size by the Myc antagonist and transcriptional repressor Mad1," EMBO J **21**, 4820-4830 (2002).

135. M. F. Shirazi, K. Park, R. E. Wijesinghe, H. Jeong, S. Han, P. Kim, M. Jeon, and J. Kim, "Fast Industrial Inspection of Optical Thin Film Using Optical Coherence Tomography," Sensors-Basel **16**(2016).

136. S. Jecić and N. Drvar, *The assessment of structured light and laser scanning methods in 3D shape measurements* (2003), pp. 18-20.

137. B. Langmann, K. Hartmann, and O. Loffeld, *Depth camera technology comparison and performance evaluation* (2012), Vol. 2, pp. 438-444.

138. A. S. Malik, *Depth Map and 3D Imaging Applications: Algorithms and Technologies: Algorithms and Technologies* (IGI Global, 2011).

139. P. C. Gregory, "A Bayesian revolution in spectral analysis," Aip Conf Proc **568**, 557-568 (2001).

140. Z. Hu and A. M. Rollins, "Fourier domain optical coherence tomography with a linear-in-wavenumber spectrometer," Opt. Lett. **32**, 3525-3527 (2007).

Biography

Ruobing Qian received his Bachelor of Science in Engineering with the highest distinction from University of Rochester in 2014, majoring in biomedical engineering with two minors in Electrical and Computer Engineering and Mathematics. Subsequently, Ruobing earned a Ph.D. in Biomedical Engineering from Duke University in 2020, advised by Prof. Joseph A. Izatt. Towards his Ph.D., he also earned a M.S. in Electrical and Computer Engineering from Duke University. Ruobing has authored or co-authored 10 published, accepted or submitted manuscripts, 4 manuscript currently in preparation, 17 conference presentations and 2 patent applications.

Publications:

- **R. Qian**, R. P. McNabb, K. C. Zhou, H. M. Mousa, D. R. Saban, V. L. Perez, A. N. Kuo, J. A. Izatt, "*In vivo* quantitative analysis of anterior chamber cell composition using spectroscopic Optical Coherence Tomography", In Preparation.

- W. Liu***, R. Qian*,** S. Xu, P. C. Konda, E. Berrocal, J. Jonsson, D. Borycki, M. Harfouche, R. Horstymeyer, "Highly parallelized diffuse correlation spectroscopy with a SPAD array", In Preparation.

- **R. Qian**, K. C. Zhou, J. Zhang, C. Viehland, H. Dhalla, J. A. Izatt, "Time-frequency multiplexed 3D imaging", In Preparation.

- K.C. Zhou, **R. Qian**, H. Dhalla, S. Farsiu, J. A. Izatt, "A k-space theory of 3D coherent microscopy", In Preparation.

- M. Draelos, P. Ortiz, **R. Qian** , C. Viehland , R.P. McNabb, K. Hauser , A. K. Kuo , J. A. Izatt, "Robotic optical coherence tomography scanner for autonomous eye imaging of freestanding subjects", Submitted to ***Nature Biomedical Engineering.***

- B. Keller, M. Draelos, K. Zhou, **R. Qian**, G. Konidaris, K. Hauser, A. K. Kuo, J. A. Izatt, "OCT guided robotic ophthalmic microsurgery via reinforcement learning from demonstrations," ***IEEE Transactions on Robotics***, April, 2020.

- K. C. Zhou, **R. Qian**, S. Farsiu, J. A. Izatt, "Spectroscopic optical coherence refraction tomography", ***Optics Letters* 45,** 2091-2094 (2020).

- Y. Tian, M. Draelos, G. Tang, **R. Qian**, A. K. Kuo, J. A. Izatt , K. Hauser, "Toward autonomous robotic micro-suturing using optical coherence tomography calibration and path planning," *International Conference on Robotics and Automation* ***(ICRA)***, 2020.

- **R. Qian**, W. F. Huang, R. P. McNabb, K. C. Zhou, Q. H. Liu, A. K. Kuo, J. A. Izatt, "Aqueous blood cell characterization using spectroscopic OCT", ***Biomed. Opt. Express*** 10, 3281-3300 (2019).

- K. C. Zhou, **R. Qian**, S. Degan, S. Farsiu, J. A. Izatt, "Optical coherence refraction tomography", ***Nature Photonics*** (2019). M. Draelos, P. Ortiz, **R. Qian**, B. Keller, K. Hauser, A. K. Kuo, J. A. Izatt, "Automatic Optical Coherence Tomography Imaging of Stationary and Moving Eyes with a Robotically-aligned Scanner," *International Conference on Robotics and Automation* ***(ICRA)***, 2019.

- **R. Qian**, R. P. McNabb, A. K. Kuo, J. A. Izatt, "Anterior chamber blood cell differentiation using spectroscopic OCT," ***SPIE Proc*** 10474, 2018.

- **R. Qian**, O. M. Carrasco-Zevallos, S. Mangalesh, N. Sarin, L. Vajzovic, S. Farsiu, J. A. Izatt, C. Toth "Characterization of Long Working Distance Optical Coherence Tomography for Imaging of Pediatric Retinal Pathology," ***Transl. Vis. Sci. Technol.*** 6,12 (2017).

- O. M. Carrasco-Zevallos, **R. Qian**, N. Gahm, J. Migacz, C. A. Toth, J. A. Izatt, "Long working distance OCT with a compact 2f retinal scanning configuration for pediatric imaging," ***Optics Letters***, 41(21), 4891-4894 (2016).

- D. W. Shipp, **R. Qian**, A. J. Berger, "Angular-domain scattering interferometry," ***Optics Letters***, 38(22), 4750-4753 (2013).

Conference Presentations:

- K. C. Zhou, **R. Qian**, S. Farsiu, J. A. Izatt, "Resolution enhancement and speckle reduction in coherence imaging: a k-space model of optical coherence refraction tomography (OCRT)," OSA Biophotonics, 2020.

- W. Liu, **R. Qian**, S. Xu, P. C. Konda, R. W. Horstmeyer, "Fast sensitive diffuse correlation spectroscopy with a SPAD array", OSA Biophotonics, 2020.

- W. Liu, **R. Qian**, S. Xu, P. C. Konda, H. Wang, R. W. Horstmeyer, "High-speed, high-sensitivity diffuse correlation spectroscopy using a single-photon avalanche diode array", SPIE Photonics West, San Francisco, 2020.

- K. Hagan, T. Dubose, **R. Qian**, J. Park, R.P. McNabb, J.A. Izatt, S. Farsiu, "Design and fabrication of the first handheld multimodal adaptive optics scanning laser ophthalmoscope", ARVO Annual meeting, Vancouver, 2019.

- **R. Qian**, R. P. McNabb, A. K. Kuo, J. A. Izatt, "Quantitative analysis of anterior chamber blood cell mixture composition using spectroscopic optical coherence tomography," SPIE Photonics West, San Francisco, 2019.

- K. C. Zhou, **R. Qian**, S. Farsiu, J. A. Izatt, "Spectroscopic optical coherence refraction tomography for isotropically resolved imaging with simultaneously high spatial and spectral resolution," SPIE Photonics West, San Francisco, 2019.

- M. Draelos, P. Ortiz, **R. Qian**, C. Viehland, B. Keller, T. DuBose, A. N. Kuo, J. A. Izatt, "Robotically-aligned optical coherence tomography for automatic imaging of stationary and moving eyes," SPIE Photonics West, San Francisco, 2019.

- **R. Qian**, R. P. McNabb, A. K. Kuo, J. A. Izatt, "Anterior chamber blood cell differentiation using spectroscopic OCT," SPIE Photonics West, San Francisco, 2018. **(Pascal Rol Award/Best Paper Finalist)**

- K. C. Zhou, **R. Qian**, S. Degan, S. Farsiu, J. A. Izatt, "Optical coherence refraction tomography for isotropically resolved cross-sectional imaging," SPIE Photonics West, San Francisco, 2018.

- **R. Qian**, O. M. Carrasco-Zevallos, L. Vajzovic, C. A. Toth, J. A. Izatt, "Imaging of pediatric retinal pathology with long working distance optical coherence tomography," ARVO Annual Meeting, Seattle, 2016.

- **R. Qian**, O. M. Carrasco-Zevallos, L. Vajzovic, C. A. Toth, J. A. Izatt, "Long working distance optical coherence tomography for pediatric imaging," SPIE Photonics West, San Francisco, 2016.

- **R. Qian**, O. M. Carrasco-Zevallos, L. Vajzovic, C. A. Toth, J. A. Izatt, "Long Working Distance Swept Source Optical Coherence Tomography for Pediatric Imaging," *ARVO Annual Meeting, Denver, 2015.*

- D. W. Shipp, **R. Qian**, A. E. Cannaday, A. J. Berger, "Precise, time-lapsed measurements of organelle sizes in single cells by holographic angular domain elastic scattering," SPIE Photonics West, 2014.

- **R. Qian**, D. W. Shipp, A. J. Berger, "Interferometric measurement of organelle-size objects," University of Rochester Undergraduate Research Exposition, 2013.

- **R. Qian**, D. W. Shipp, A. J. Berger, "Interferometric scattering measurement of organelle sizes in single cells," BMES Annual Meeting, Seattle, 2013.

- D. W. Shipp, **R. Qian**, A. J. Berger, "Angular-domain scattering interferometry," ECI Advances in Optics for Biotechnology, Medicine and Surgery, Lake Tahoe, 2013.

- D. W. Shipp, **R. Qian**, A. J. Berger, "Size- and position- dependent angular scattering interferometry," SPIE Photonics West, San Francisco, 2013**.**

Patents:

- **R. Qian**, K. C. Zhou, O. M. Carrasco-Zevallos, J.A. Izatt, "Novel 3D Sensing Depth Camera," U.S. Provisional Patent Application No. 63/014,319.

- K. C. Zhou, **R. Qian**, S. Farsiu and J. A. Izatt, "Systems and Methods for Optical Coherence Refraction Tomography," U.S. Patent Application No. 62/623,044.